Steady State Performance of an Elastic Flexible Wing

by

William Edward Gorgen

B.S., Massachusetts Institute of Technology (1991)

Submitted to the Department of Aeronautics and Astronautics
in partial fulfillment of the requirements for the degree of

Master of Science in Aeronautics and Astronautics

at the

MASSACHUSETTS INSTITUTE OF TECHNOLOGY

May 1993

Author .....
Department of Aeronautics and Astronautics
May 18, 1993

Certified by .....
Sheila E. Widnall
Professor of Aeronautics and Astronautics
Thesis Supervisor

Accepted by .....
Professor Harold Y. Wachman
Chairman, Departmental Graduate Committee

Steady State Performance of an Elastic Flexible Wing

by

William Edward Gorgen

Submitted to the Department of Aeronautics and Astronautics
on May 18, 1993, in partial fulfillment of the
requirements for the degree of
Master of Science in Aeronautics and Astronautics

Abstract

This Study considers a flexible wing which is designed to change camber in response to lift loads. This cambering response is achieved by properly constraining a flexible bending plate-like wing. By supporting the leading and trailing edges of such a wing, the lift loads cause the wing to camber. The performance of flexible wings differs significantly from traditional rigid wings. The variable camber of the flexible wings results in a lift curve whose slope depends on the stiffness of the airfoil as related to the dynamic pressure of the flow. This relative stiffness of the bending plate to the dynamic pressure of the flow is measured by a non-dimensional stiffness parameter. A numerical analysis combining a vortex lattice aerodynamic model and a finite element structural model is used to determine the performance characteristics of these wings. The analysis is idealized by including only the linear bending effects of the structure and the inviscid aerodynamics of the wing. The results of the analysis show the theoretical performance characteristics of flexible wings in terms of the lift curve slope of the wing as related to its stiffness and aspect ratio.

Thesis Supervisor: Sheila E. Widnall
Title: Professor of Aeronautics and Astronautics

Acknowledgments

I would like to thank all of the people who helped me through MIT and helped me finish my thesis. I have been very fortunate during the past few years to have had an opportunity to participate in several exiting projects. Without the many people that were involved in these projects, I would not have learned as much or had as much fun. I would like to thank all of the people for all that they have meant to me over the years.

I could have never done any of this work without the help and friendship of Jeff "Orville" Evernham. Together, we conceived of a flexibly cambering wing and sought to develop it as a sailboard fin for our own boards. Without his input and collaboration, the entire concept would not exist. Of course, without Jeff's unending enthusiasm for the sport of windsurfing, I would still be practicing my waterstarts on a transition board. And without his companionship in the classroom and at Theta Xi, I surely would have never been able to finish even a single degree in aeronautical engineering, much less two. But most of all, I want to thank Jeff for all the craziness and fun that we had together.

During the past two years, it could have been easy for me to fall into a daily regimen of studies and work. And without the constant encouragement from Matt Butler, Ted Liefield, Scott Stephenson, Rick "Pax" Paxson and the rest of the gang, I just may have. Thanks guys for keeping me swimming in beer at crucial times in my graduate career. And thanks as well to the bands Letters To Cleo, Cliffs of Dooneen and Chucklehead for making the nights at the clubs such memorable events.

The times away from school added so much to the years I've spent here. I'd like to thank The Boyz (and Girlz) of $B\Phi\Delta$ and our sister sorority, $\Pi M\Sigma$, for all the fun and crazy times. Living with them was never dull.

I'd also like to thank Alex Chisholm. Alex gave me a unique perspective on the world and taught me more about life than he will ever know. The time I spent with Alex is some of the most memorable and important times of my college career. Without Alex, I would have never survived emotionally.

My family was always there for me and supported me throughout my college life. My dad, as an engineer, could understand many of the issues I faced and encouraged me to keep working. My mom, who kept asking if I had finished my "paper", supported me in more ways that I can express. My sister Mary kept me sane for these past years by keeping my social skills up to date. The rest of my family also gave me support and encouragement in all of my endeavors.

I'd like to thank Sheila and Bill Widnall who believed in the idea of flexible wings enough to support my work not only in graduate school, but also in Flex Foil Technology Corporation which they co-founded with Jeff Evernham and I. If it was not for sheila's guidance on the development of this idea, it would probably have never gotten off the ground.

I'd also like to thank Prof. Mark Drela for teaching me how to design wings. His inspired teaching as well as his guidance of the Decavitator Hydrofiol Team inspired me to dream of flight in all of its forms. Mark also taught me that fluid dynamics often can be studied with a pint or two of one of Cambridge Brewery's Ales.

Developing numerical algorithms to solve problem can often be a tedious programming task. However, it can be impossible without the support of people who have done similar work before. Without Steve Ellis, the Athena God who kept Reynolds and the rest of the Fluid Dynamics Research Lab's Computer hardware up and running, I never could have finished my research. I'd also like to thank Harold "Guppy" Youngren for giving me his vortex lattice code and advice on how to use it and modify it. Prof. Mike Graves who taught me all about the inner workings of Finite Element programs. Prof. Bathe from the Mechanical Engineering department answered an endless barrage of questions from me about how to make his ADINA program work. And I'd also like to thank the Freindly people at the MITSF who put up with my stupidity on the cray.

In trying to turn all of my ideas into reality, I spent a lot of time in the Aero-Astro Projects lab building models. I'd like to thank Jeff DiTullio, Dick Perdichizzi, Don Weiner and Earle Wassmouth who let me run wild in their machine shop. Thanks especially to Jeff, who was an unlimited pool of information about composite production techniques.

Finally, I'd like to thank all of my officemates for making the office such a great place to work. I wish all of them the best of luck with their reseach as well. Hopefully they will have as much fun as I did.

Contents

List of Figures

List of Tables

Chapter 1

Introduction

One of the main goals in the design of a lifting body such as a wing is to maximize the lift to drag ratio. This desire to minimize drag resulted in the development of cambered airfoil sections for wings. Adding camber to wings has the effect of increasing the amount of lift that can be achieved at a certain angle of attack. Camber also increases the magnitude of the lift that can be generated before the wing transitions from low drag laminar flow to high drag turbulent flow. By properly designing the camber of a wing it is possible to achieve a high lift to drag ratio for a certain range of operating points. Traditional fixed geometry wings generate lift through a combination of camber and angle of attack. However, since the amount of camber is fixed, these wings can only increase the amount of lift they are generating by increasing their angle of attack. This tends to add drag and decreases the efficiency of the wings. Thus, the range of efficient operation of a fixed-camber wing is limited to a small range close to the operating point that it was designed for. When the wings deviate too far from this design point, their efficiency goes down.

By utilizing airfoil sections that change camber as the operating point changes, it is possible to extend that range of efficient operation of a wing. Wings of this type are known as variable geometry wings. The characteristics of these wings make them ideal for vehicles that require a large range of lifting needs, a wide range of speeds or a need to generate both positive and negative lift. There are many wing designs which utilize variable geometry airfoils but their shapes are usually controlled externally by

the use of mechanical actuators that deploy leading edge flaps or slats or otherwise change the shape of the wing. While these wings often achieve significant performance advantages over fixed geometry wings, the control and actuation system is often too large and complex to be practical for many smaller applications.

An elastically flexible wing changes its camber shape automatically, in response to lifting loads. Such an automatic camber-adjusting wing does not use external control devices to change camber, but rather controls the shape through the elastic flexibility of the chordline. Because this wing can change its amount of camber, it responds to an increased lift requirement by increasing its camber as well as its angle of attack.

This automatic cambering behavior in response to load is achieved by controlling the flexibility of the wing in the chordwise direction. By having a flexible chordline and being constrained in deflection at the leading and trailing edges, the lift forces push up on the center of the wing and bend it into a cambered shape. Thus, additional lift is generated by an increase in camber as well as a change in angle of attack. This increase in camber allows the wing to generate the increased lift more efficiently.

1.1 Description of Flexible Wings

The elastically flexible wings considered in this work are comprised of a flexible plate in the shape of a wing with an aerodynamic thickness distribution. The plate is supported by explicitly prescribed boundary conditions at the leading and trailing edges of the wing or by rigid spars along the leading and trailing edges that are cantilevered at the root of the wing. The spars are mounted to the craft such that they are free to pivot around their major axes. The spar that runs along the trailing edge is also free to slide in the chordwise direction to provide simple support to the plate. Thus, the spars constrain the deflection of the wing under load such that the wing is reasonably flexible in the chordwise direction but is not allowed to deform in the spanwise direction providing a flexible camberline.

By properly constraining the leading and trailing edge deflections, the wing can be made to increase its camber as the lift loads increase. By the proper tailoring of

the flexibility of the camberline, the wing can increase its camber in direct proportion to the lift loads. The flexible region should be flexible enough so that the lift loads cause it to camber, but not so flexible that it cambers more than desired.

1.2 Advantages of Flexible Wings

Flexible wings have many advantages over standard fixed geometry wings. Rigid wings are designed to operate mainly at one operating point. The camber of these wings is designed to maximize the performance at that point. Wings operating at low lift coefficients generally have low camber while higher lift coefficients generally demand higher camber. Due to their ability to change camber, flexible wings have a much broader range of lift loads where they can operate efficiently. At low lift, these wings have only a small amount of camber much like the rigid wing designed to operate at that same operating point. However, at higher lift, the camber is increased and thus the wing operates like the rigid wing with higher camber. Thus, the flexible wing has the ability to perform with high efficiency over a much broader range of operating points than any one fixed geometry wing.

A flexible wing also resists stalling. Most rigid wings are designed to operate at a moderate lift point. The camber of the wing is designed to optimize the performance of the wing at that point. When such a wing is operated at a much higher lift point, it is prone to stall since it does not have enough camber for that amount of lift and must drastically increase its angle of attack. For a flexible wing, an increased lift need is met by a camber increase as well as an increase in angle of attack. Thus, the increase in angle of attack is less for the flexible wing than it is for the rigid wing and the flexible wing is further from its stall point.

1.3 Applications

Flexible wings are particularly well suited for certain applications. Given their ability to camber in the direction of the lift force, they work well on lifting bodies

that may need to generate lift in either directions such as lifting surfaces on sailboats or control surfaces on aircraft. They may also work well for devices that have a large range of lift requirements such as compressor or turbine blades in turbomachinery.

1.3.1 Aircraft

There are many types of aircraft that could utilize a wing with a wide performance range. It is not uncommon for an aerobatic aircraft to perform maneuvers that can require the wings to operate anywhere between $+6g$ and $-2g$ or more. The wings of such aircraft would need to be able to generate lift up to 6 times the weight of the aircraft as well as negative lift of 2 times the weight of the aircraft. Standard fixed geometry wings are often pushed to their aerodynamic limit, or stall point, by such extreme maneuvers. A flexible wing would be much further from its limit at these points and would be in a more efficient configuration than the fixed geometry wings. This would give the aerobatic plane a much greater stall margin as well as reduced drag, and thus more speed, through the maneuvers.

These flexible wings could also be used for control surfaces on aircraft with more conservative operation. The elevators and rudders on such aircraft operate through a wide range of lift needs. A flexible wing could adjust its camber to remain in a efficient configuration throughout a wide range of lift points giving an efficient configuration for a wide range of control surface positions.

1.3.2 Sailcraft Keels and Sails

Sailcraft have a unique place in the world of fluid dynamics. The sails and underwater appendages (such as rudders and keels) of sailcraft need to generate lift in either direction depending on the direction they are sailing in. In some operating points the wind blows over the port side of the craft and in other operating points the wind blows over the starboard side of the craft. Thus on some *points of sail* the lifting bodies must generate lift in one direction and on other *points of sail* the pressure and suction surfaces are reversed. This unique need to generate lift in both

directions resulted in the development of sails that can camber from side to side as the wind pushes on them.

However, traditional sails behave in a very different way than the flexible wings studied here. Structurally, a wing is a membrane rather than a bending plate. The deflection state of the loaded membrane is determined by the tensions that build up in the membrane rather than the bending strains that are associated with the plate. The shape of a sail is determined mainly by the way that the sailmaker cut the cloth of the sail. The sail tends to exhibit a "snap through" camber response where it takes on one of only two possible shapes; positively cambered or negatively cambered. The shape of the elastic flexible wing studied is proportional to the loading on it.

In a similar way, a flexible wing can camber in either direction depending on the direction of the lift forces. By having a flexible wing for a keel, the drag of the craft can be reduced and the craft can go faster. The ability to camber in either direction allows the performance advantages to be realized on either tack. The elastic response of the camber to the lift allows the keel to adjust to the lift need of the boat. Flexible wings can also give rudders better control authority. The rudder, much like the elevators on aircraft, needs to generate lift in either direction to quickly adjust the direction of the boat. A flexible rudder could reduce the drag associated with the steering the boat allowing the boat to maintain more speed through maneuvers.

1.3.3 Turbomachinery

The compressors in turbomachinery act to push air or some other fluid through the turbomachine. The turbines of these machines act to extract energy from the fluid. Both the compressors and turbines make use of lifting bodies to impart or extract energy from the fluid flow. In many applications, these lifting bodies are blades with airfoil cross-sections. The performance of these blades is limited by two operating points of the blades. The high lift limit is the stall point of the blades. The low lift point or *windmilling point* is the zero lift point of the blades. The efficiency of the machinery is often limited by the difference between these points.

By utilizing a flexible blade, the difference in lift between the stall point and

windmilling point is much greater resulting in an increased efficiency of the turbomachinery. The difference in lift between the stall point and the windmilling point results in a large difference in camber. Given the large camber at the stall point, the lift at this point can be increased, or the angle of attack of the blades can be reduced. The drag at the windmilling point is reduced by having an uncambered airfoil at this zero lift point.

Chapter 2

Theory and and Modeling of Flexible Wings

An elastically flexible wing changes its shape when acted on by the aerodynamic pressures associated with lift. The centerline of the wing can be thought of as a bending plate acted on by the distributed load of the aerodynamic pressure forces. By fixing the deflection of the leading and trailing edges of the wing, the wing acts like a simply supported bending plate. As the lift forces build up on the wing, it bends into a positively cambered shape. By properly tailoring the flexibility of the camberline, the camber response of the wing can be made to be proportional to the load. Such a wing has dramatically different performance than a standard fixed camber wing.

2.1 Classical Theories

For wings of reasonably high aspect ratio the flow is roughly parallel to the direction of travel. At any spanwise location of such a wing, the flow is very similar to the two-dimensional flow around an airfoil that is identical to the cross section of the wing. The performance of these airfoil sections give useful information about the behavior of the entire wing itself.

Similarly, a plate that is simply supported along two opposite edges and is free

along the other two, often has a deflection state that is similar from one spanwise station to another. If the plate is much longer than it is wide, has supports along the longer edges and has minimal variation of the load in the spanwise direction, the variation in the deflection in that direction will be negligible. Thus, the deformation of the entire plate can be studied by looking at the two-dimensional bending of cross-sections of the plate.

To understand the behavior of a flexible wing, it is useful to explore the theoretical performance of a two-dimensional flexible airfoil. A two-dimensional flexible airfoil theory can be derived by combining classical linear bending plate theory and linear inviscid airfoil theory. Classical plate theory describes the bending of the camberline under load and classical airfoil theory describes the the pressure load distribution on an airfoil of a given shape. A combination of these two theories gives a good model for the behavior of the wing sections and therefore the wing itself.

2.1.1 Two-Dimensional Plate Theory

In a two-dimensional analogy, the camberline of a flexible airfoil can be thought of as a bending plate simply supported with a pin joint at the leading edge and a roller pin at the trailing edge. When such a plate is loaded, it bends. The lift forces that act on the airfoil act upon the plate and bend it into a cambered shape as shown in Figure 2-1.

The elastic deflection of a bending plate can be described by the Bernuolli-Euler plate equation given in [9]:

$$D \frac{\partial^4 w(x)}{\partial x^4} = p_z(x) \tag{2.1}$$

Where the plate stiffness, D, is given in terms of the elastic modulus, E, Poisson's ratio, ν and the thickness, h as

$$D \equiv \frac{E\, h^3}{12(1 - \nu^2)} . \tag{2.2}$$

The deflection at some point $x_p, w(x_p)$, is proportional to the magnitude of the

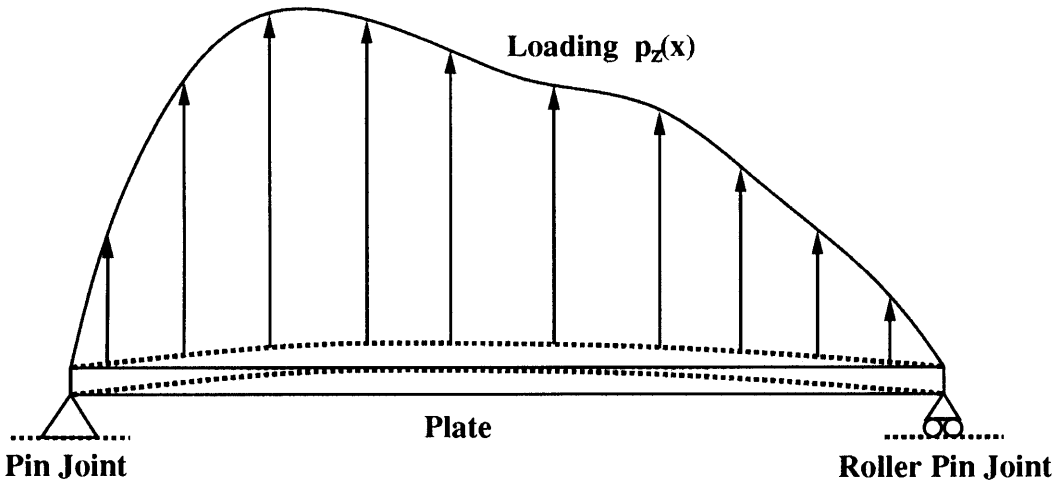

Figure 2-1: Simply Supported Plate Acted on by a Distributed Load

load so long as the load is distributed in the same way. Thus if

$$C\ p(x) \implies w(x_p) \tag{2.3}$$

for some constant, C, then for a proportional load state, $\alpha\ p(x)$, the deflection state is given by

$$C\ [\alpha\ p(x)] \implies \alpha\ w(x_p) \tag{2.4}$$

This proportional response is valid for a small strain (small deflections) and linear elastic materials (constant $E(\sigma)$). Thus, if the total load on the beam doubles, the deflection at any point will also double.

The boundary conditions shown in Figure 2-1 (simply supported at the extremities of the beam) are necessary to produce a positive (upward) deflection in response to a positive load. In order for the wing to camber in the right direction, the center of the load must act between the supports. As is shown in Section 2.1.2, the loading for an uncambered wing at an angle of attack is centered at the 1/4 chord and for a purely cambered wing at zero angle of attack is located at the 1/2 chord. In order to produce positive camber, the center of load should be behind the leading edge support and in

front of the trailing edge support. This requires that the leading edge support must be in front of the 1/4 chord point in order for the uncambered wing to camber under the initial flat plate load. Further, the trailing edge support should be behind the 1/2 chord point to maintain positive camber for a purely cambered loading. The best performance is obtained for boundary conditions as close to the leading and trailing edges as possible.

2.1.2 Airfoil Theory

Much aerodynamic theory has been developed to describe the behavior of lifting bodies. A wing of sufficiently high aspect ratio can be described in terms of cross sectional airfoil shapes at its spanwise stations. The flow around such a wing has a very small velocity component in the spanwise direction such that it can be modeled as a two-dimensional flow around the various airfoil sections. Examining the behavior of airfoils in a two-dimensional flow gives a good approximation of the actual flow over the wing at various points along the span. Generally, the lift and drag performance of airfoil sections can give a good indication of the lift and drag performance of the entire wing.

The theory of thin airfoils, as given by Von Mises in [7], gives an approximate solution for the flow around a thin airfoil, and thus the lift, in terms of the vorticity distribution along the camberline, $\gamma(x)$. The vorticity distribution, $\gamma(x)$, is determined from the camberline of the airfoil by enforcing the conditions that there is no flow across the camberline (i.e. the flow is tangent to the camberline) and that $\gamma(x)$ goes to zero at the trailing edge (thus enforcing the Kutta condition). The flow around the airfoil that is induced by such a $\gamma(x)$ distribution is a good approximation to the flow around a thin airfoil with the same camberline.

The lift due to this vorticity distribution can be expressed in a non-dimensional lift coefficient as

$$C_l = \frac{2}{c\, V_\infty} \int_{-c/2}^{c/2} \gamma(x)\, dx \tag{2.5}$$

where c is the chord of the airfoil and V_∞ is the freestream flow velocity. For a straight camberline at an angle to the freestream flow of α, the lift coefficient is

$$C_l = 2\pi\alpha \tag{2.6}$$

Similarly, the lift coefficient due to a curved camberline given in terms of the max camber, ϵ, at zero angle of attack to the flow ($\alpha = 0$) is

$$C_l = \pi\epsilon \tag{2.7}$$

Combining these two results for a general cambered airfoil at some angle of attack gives

$$C_l = 2\pi\alpha \ + \ \pi\epsilon. \tag{2.8}$$

The moment due to the pressure distribution is given by

$$M = -\int_{-c/2}^{c/2} p(x)\,(x - x_m)\,dx. \tag{2.9}$$

where x_m is the point that the moment is acting around. In most cases, the moment is calculated around the 1/4 chord since the moment is independent of the lift when it is calculated around the 1/4 chord. For the uncambered airfoil, this integral evaluates to zero implying that the center of lift of the flat plate is at the 1/4 chord. Performing this same integral for the cambered airfoil at zero angle of attack shows that the moment around this point is equivalent to the lift force acting at the 1/2 chord point. Thus the center of lift for the pure camber case is located at the 1/2 chord.

The location of the center of lift for a general airfoil having some non-zero camber magnitude and at some non-zero angle of attack depends on both the amount of camber and the angle of attack. Because camber produces lift at the 1/2 chord while angle of attack produces lift at the 1/4 chord, the amount of lift produced by each of these factors determines where the center of lift is located, and the magnitude of the lift at that point.

Traditional aerodynamic theory describes airfoils that have an arbitrary but fixed amount of camber. The lift and drag forces are usually described in terms of nondimensional coefficients that do not depend on the size of the airfoil or the strength of the fluid flow. The lift coefficient of these fixed geometry airfoils is proportional to their angle of attack. The relationship between angle of attack and lift coefficient is described by the *lift curve* for that airfoil. Before stall, all inviscid airfoils have a lift curve that is linear with a positive slope equal to 2π. An uncambered airfoil has a lift coefficient equal to 0 at zero angle of attack. A cambered airfoil on the other hand has a positive amount of lift at zero angle of attack. The lift curve of the cambered airfoil is still 2π and is simply shifted upward from the uncambered lift curve. The more camber an airfoil has, the more its lift curve is shifted upward from the uncambered airfoil. The additional lift produced by camber is linearly proportional to the amount of camber. The lift curves for various fixed geometry airfoils is shown in Figure 2-2 as well as in [8].

2.2 Elastic Airfoil Theory

The behavior of elastic airfoils can be described be combining simple plate theory with simple airfoil theory resulting in an aeroelastic description of the flexible airfoil. Airfoil theory describes the amount of lift that is generates by the airfoil and how that lift is distributed. Beam theory describes how a beam bends under load. The airfoil lift loads bend the beam and shape of the beam describes the camber of the airfoil. The derivation of the linear aeroelastic theory is relatively straight forward, but does require a few slight modifications to each of the theories. The deformation response of the bending beam depends on the actual lift force of the airfoil rather than the lift coefficient. Thus, when describing the behavior of the elastic airfoil in terms of the traditional lift curve, it is also necessary to look at the lift of the airfoil at each point on the curve.

2.2.1 Linear Theory of Flexible Airfoils

For a flexible airfoil, as the angle of attack increases, the camber increases and thus the coefficient of lift will continually rise at a rate faster than the traditional lift curve. For a given camber and coefficient of lift, the angle of attack can be found from traditional cambered airfoil lift curves. However, the camber increases as the lift coefficient increases. Thus the lift curve slope for a flexible airfoil should be greater than the traditional lift curve slope of 2π. Figure 2-2 shows the lift curves of fixed geometry airfoils with different amounts of camber and the lift curve for an automatic camber adjusting airfoil. It shows how the lift curve slope is increased by the changes in camber.

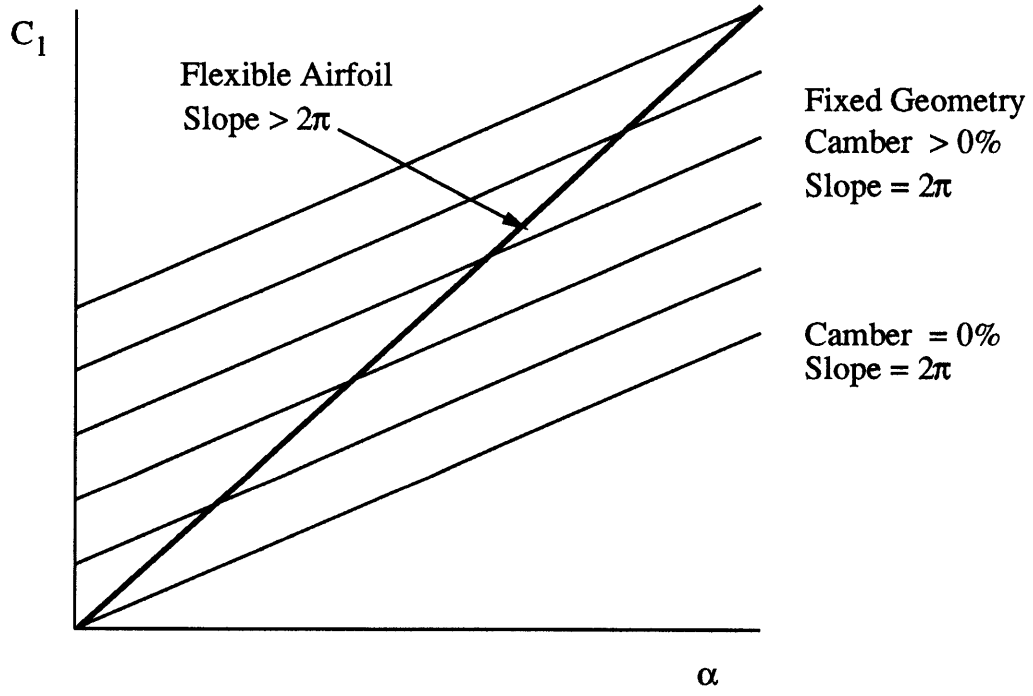

Figure 2-2: Lift Curves for a Flexible Airfoil and Rigid Airfoils of Various Camber

2.2.2 Stiffness Parameter

The two major elements which determine the magnitude of a flexible airfoil's camber are the stiffness of the airfoil and the strength of the aerodynamic loading. The interaction and balancing of these two forces determines the amount of bend in the plate, and thus the amount of camber in the airfoil.

In order to determine the exact bending behavior of the airfoil, the bending stiffness and aerodynamic forces are equated in a coupled aerodynamics, bending plate equation:

$$D\frac{\partial^4 w(x)}{\partial x^4} = p_z(x) \tag{2.10}$$

where D is the plate stiffness, $w(x)$ is the deflection of the plate at any point, x, and $p(x)$ is the aerodynamic pressure load applied to the plate at any point, x. From this equation it is easy to see that increasing the load, $p(x)$ causes the plate to bend, increasing the camber, and that increasing the elastic plate modulus, D, causes the plate to bend less, decreasing the camber.

For a given operating point with a fixed fluid dynamic pressure, q_∞ and given an airfoil section of chord length, c, and plate stiffness, D, the camber response of the wing to the loading can be described by a nondimensional stiffness parameter, K.

$$K \equiv \frac{D}{q_\infty(\frac{c}{2})^3} \tag{2.11}$$

This stiffness parameter describes the relative strength of the restoring force of a flexible plate and the aerodynamic forces of the flow. Larger values of K describe stiffer airfoils with respect to the flow. Airfoils that have the same relative strengths of the plate and the flow, will have the same cambering behavior for specific angles of attack. Thus, the slope of the lift curve is related to the stiffness parameter, K. The stiffer the airfoil, the less it cambers and thus the lower the lift curve slope. The limiting case of this is when the airfoil becomes infinitely stiff. At this point the airfoil does not camber at all and thus the lift curve matches that of a symmetrical, rigid airfoil. Smaller values of K describe more flexible airfoils with respect to the

flow. As the stiffness, K, goes down, the airfoil cambers more and thus the slope of the lift curve goes up. The limiting case of this is a an airfoil made with a very flexible material such as a cloth sail. A sail cambers to its full extent with minimal load and thus its lift curve in the cambering region jumps to full camber immediately with no proportional response. In between these two limits is the K range for an automatic camber adjusting airfoil. The Lift Curves for automatic camber-adjusting airfoils with different K values are shown in Figure 2-3.

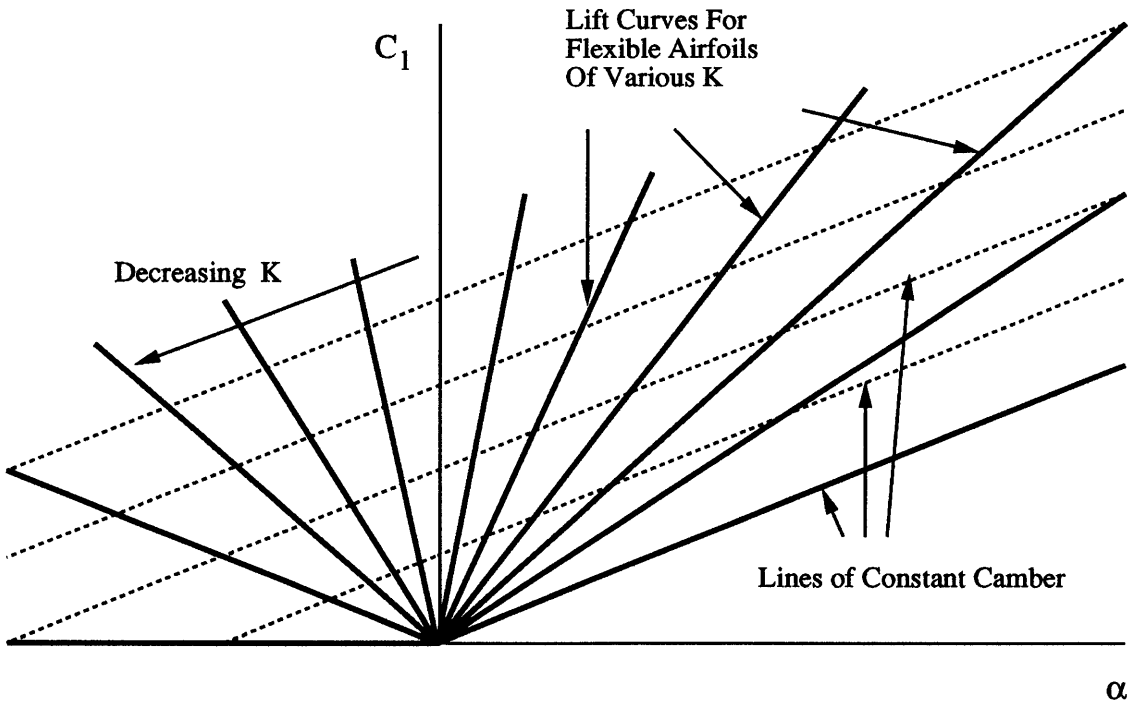

Figure 2-3: Lift Curves for Airfoils of Various K Values

2.2.3 Critical Stiffness

The stiffness that results in an infinite lift curve slope is defined as the critical stiffness ,K_{crit}. At this value of the stiffness parameter, the camber of an airfoil at zero angle of attack results in exactly the proper amount of lift to sustain that camber. The airfoil can operate in equilibrium at any amount of camber without a change in angle of attack. Thus the camber is undetermined for this stiffness at zero angle of attack.

The critical stiffness depends, in part, on the distribution of the plate stiffness, D. For a constant D, the value of K_{crit} is calculated by Widnall *et. al.* in [10] to be 1.4. For a case where the plate stiffness varies, this value can change. In the case of a NACA 0012 airfoil made from a constant modulus, isotropic material, D will be larger in the center, due to the greater thickness, than it is near the leading and trailing edges where the airfoil is much thinner. If for this case an average plate modulus D_{ave} is used in calculating K, then the value of K_{crit} is higher than 1.4.

For values of K below the critical stiffness, any initial camber at a fixed angle of attack results in a full divergent deflection of the camberline. Thus in a theoretical aerodynamic sense, the airfoil undergoes static aeroelastic divergence at the critical stiffness. From a structural point of view, however, it is still possible for the aerodynamic forces and the plate structure to achieve an equilibrium for values of the stiffness parameter below K_{crit}. A cambered airfoil at some positive lift but negative angle of attack produces pressure forces that would cause a flexible airfoil to camber. By fixing the lift of the wing and allowing the angle of attack of the wing to adjust to changes in the camber, it is possible to achieve an elastic equilibrium for values of K less than K_{crit}.

The theoretical lift curve in Figure 2-3 shows that for values of K below K_{crit}, the lift curve slope is negative. This occurs when the increase in loading causes the airfoil to camber to such an extent that the increase in lift due to camber is greater than the increase in the restoring force of the beam. Such negative lift curves would be impossible to achieve in a wind tunnel or other experimental situation, but is relatively easy to achieve numerically or for applications to craft where the lift is determined rather than the angle of attack of the airfoil.

2.2.4 Effect of Spar Placement

The stiffness parameter defined in Equation 2.11 is based on the boundary conditions at the leading and trailing edge points. However, this boundary condition cannot be realized in a real wing because the spars that enforce the boundary conditions cannot be located at the leading and trailing edges. Since the airfoil has no

thickness at the leading and trailing edges, a spar located there would also have no thickness and thus no strength. In real wings, these spars must be placed where the airfoil has significant thickness so that a structurally efficient spar can be used.

For such real wings, the spars are placed closer to the mid chord where the airfoil is thicker. However, the spars cannot be placed arbitrarily as explained in Section 2.1.1. For many applications the structural considerations of the spars are an important design limitation and the designer is forced to maximize the spar thickness to support the loads on the wing. Thus the spars are placed as close to the thickest part of the airfoil as possible. It has been determined (mainly through working designs) that the leading edge spar should not be much further back than the 10% chord point and the trailing edge spar no further forward than the 70% chord point. The portion of the airfoil in front of the leading edge axle and behind the trailing edge axle should be made from a much stiffer material than the flexible region so that there is no bending of the chordline in these regions.

Placing the spars at locations other than the leading and trailing edges has a large effect on the value of the stiffness parameter of the airfoil. Placing the spars closer together acts to effectively stiffen the airfoil in two ways. First, the flexible region between the spars is smaller and making the plate seem stiffer. Secondly, some of the load acts on the airfoil regions in front of and behind the spars. Thus, the load acting on the flexible section is diminished and the load acting beyond the spars acts to decamber the airfoil. This effect was quantified by Widnall *et. al.* in [10] for the spar location effect on the critical stiffness. By applying a curve fit to numerical results, K_{crit} for an airfoil with constant plate stiffness between the spars is given by

$$K_{crit} = 1.3 - 2.6\frac{x_{L.E.\ Spar}}{c} - 2.3(1 - \frac{x_{T.E.\ Spar}}{c}) \tag{2.12}$$

where $x_{L.E.\ Spar}$ and $x_{T.E.\ Spar}$ are the x locations of the leading and trailing edge spars.

2.3 Two-Dimensional XFOIL Tests

The viscous drag of an airfoil is determined by many characteristics of the airfoil shape and operating point. The drag polar for an airfoil shows the relationship of drag to lift coefficient for the airfoil. Changes in the camber of an airfoil change the lift coefficient associated with the minimum drag coefficient for an airfoil. In general, increases in camber increase the minimum drag lift coefficient. Figure 2-4 show how the minimum drag point moves to higher lift coefficient as the camber of the airfoil increases.

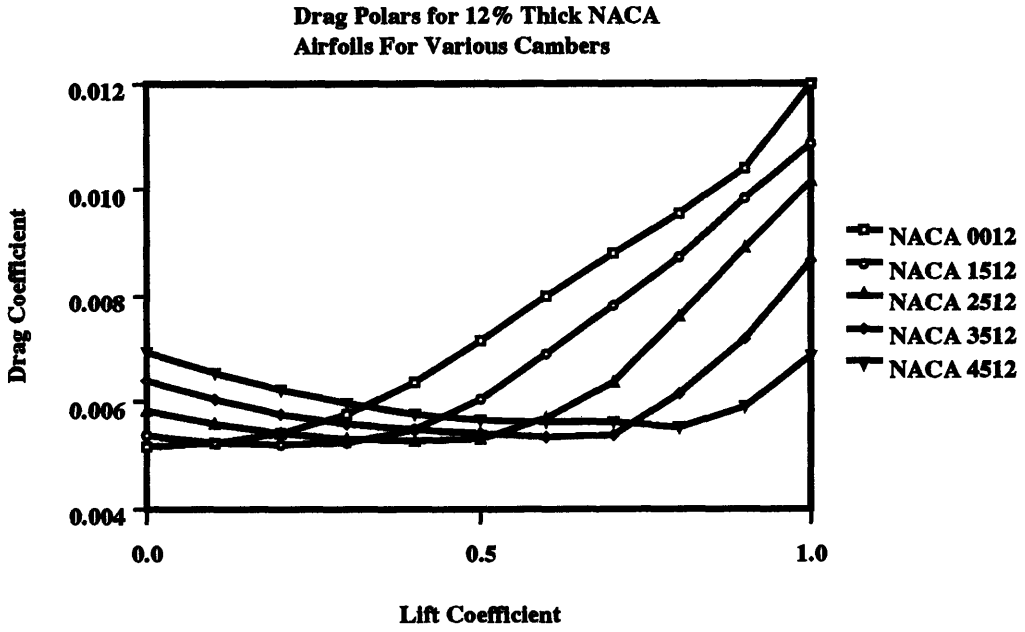

Figure 2-4: Drag Polars for Airfoils of Various Cambers

In order to determine the value of K that produces the best lift to drag ratio for a flexible airfoil, the performance of several characteristic airfoils with similar cross sections but different amount of camber were explored. In an effort to minimize drag, an operating point was chosen for each airfoil in the lowest drag region of the drag polar. The corresponding operating points on the lift curve were determined. These operating points were connected by a line to form a composite lift curve. This lift curve describes the performance of an automatic camber adjusting airfoil as it changes camber as was illustrated in Figure 2-2. From this lift curve, a relationship between

C_l and camber was determined.

The program, XFOIL (See [3] for program details) was used to generate the lift and drag data for airfoils of various camber and lift coefficient. The NACA x515 section was chosen for the thickness and camber distribution. The Stiffness of a particular airfoil was related to a proportionality between camber and lift coefficient as

$$Flexibility = \frac{C_l}{camber} \tag{2.13}$$

For example if the flexibility, was chosen to be 10, then at a C_l of 0.1, the NACA 1515 (1% camber) was chosen; for a C_l of 0.2, a NACA 2512 (2% camber) was chosen; for a C_l of 0.3, a NACA 3512 (3% camber) was chosen; etc. In this way, a lift curve was constructed from the various operating points of the airfoil as represented by the various fixed geometry airfoils. Lift curves were constructed for various flexibilities. The results showed that the optimal lift to drag performance was attained when the camber to C_l ratio was near 5. For this flexibility, a C_l change of 0.1 results in a 2% camber change. For this flexibility, the amount of lift produced by the camber of the airfoil is about 3 times the amount of lift produced by angle of attack. Put another way, for high reynolds number airfoils, the optimal lift to drag ratio occurs when about 3/4 of the lift is produced by camber and the remaining 1/4 by angle of attack.

The lift curves generated by these XFOIL tests show the relationship of lift curve slope to stiffness for a two-dimensional airfoil. A few of the lift curves are show in Figure 2-5. The slope of the lift curve clearly varies with the stiffness of the airfoil. As the flexibility of the airfoil goes up (stiffness goes down), the slope of the airfoil's lift curve increases. For a high enough flexibility, the slope becomes negative.

The results of these XFOIL tests also give a good indication of the reduction in viscous drag of flexible wings over rigid symmetric wings. The drag polars for various flexible airfoils are shown in Figure 2-6. The drag on the rigid airfoil (flexibility = 0) increases rapidly as the lift coefficient increases because the angle of attack is also

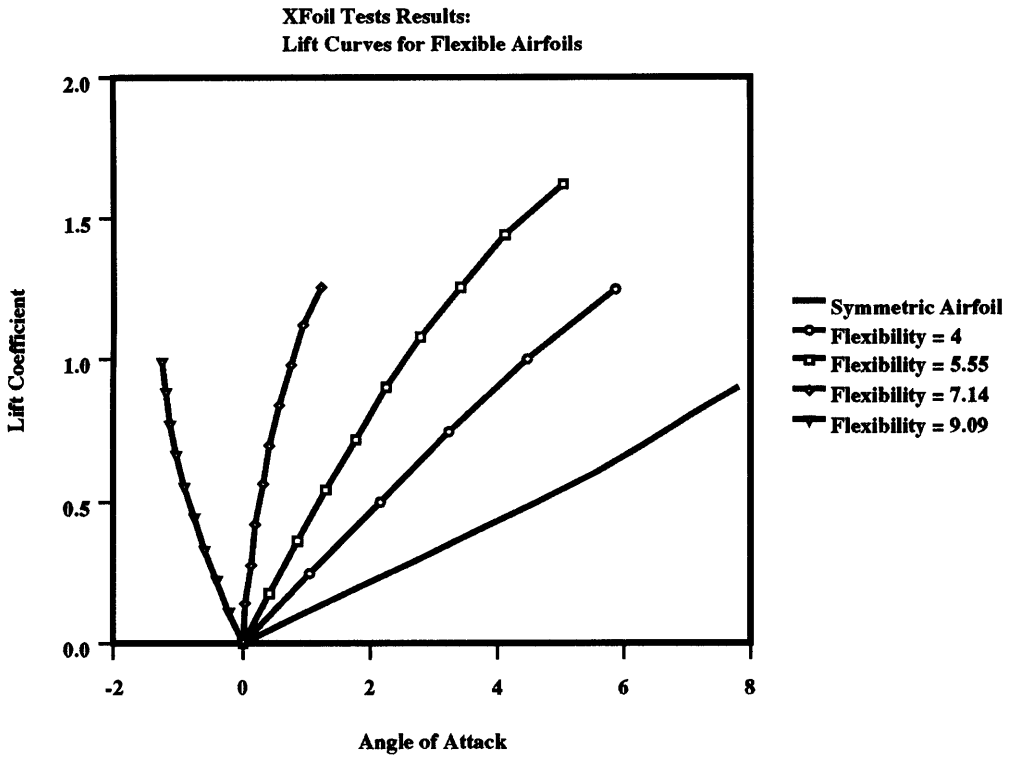

Figure 2-5: XFOIL Results: Lift curves for Viscous Airfoils

going up rapidly. As the flexibility goes up, the angle of attack change associated with a lift coefficient change is smaller, as is shown by the lift curves in Figure 2-5. The drag associated with a given lift coefficient initially decreases due to the fact that more of the lift is being generated by camber and less by angle of attack. This drag performance is optimized at a flexibility near 5.55 and for flexibilities above this, the drag goes up. This is mainly due to turbulent flow on the pressure surface of the airfoil due to the low and even negative angles of attack.

The viscous drag coefficient is affected by the flexibility of the airfoils. For the reynolds number chosen for these XFOIL tests, the minimum drag occurred for a flexibility around 5.5. There is an optimal flexibility for a flexible wing where the viscous drag is minimized. for a fixed planform, the total drag is also minimized for this flexibility. In general there is an optimal flexibility for the flexible airfoil in order to minimize the drag and thus maximize the lift to drag ratio of the wing.

The important result of this XFOIL study showed that the optimal lift curve occurs when the approximately 3/4 of the lift is produced by camber and the remaining

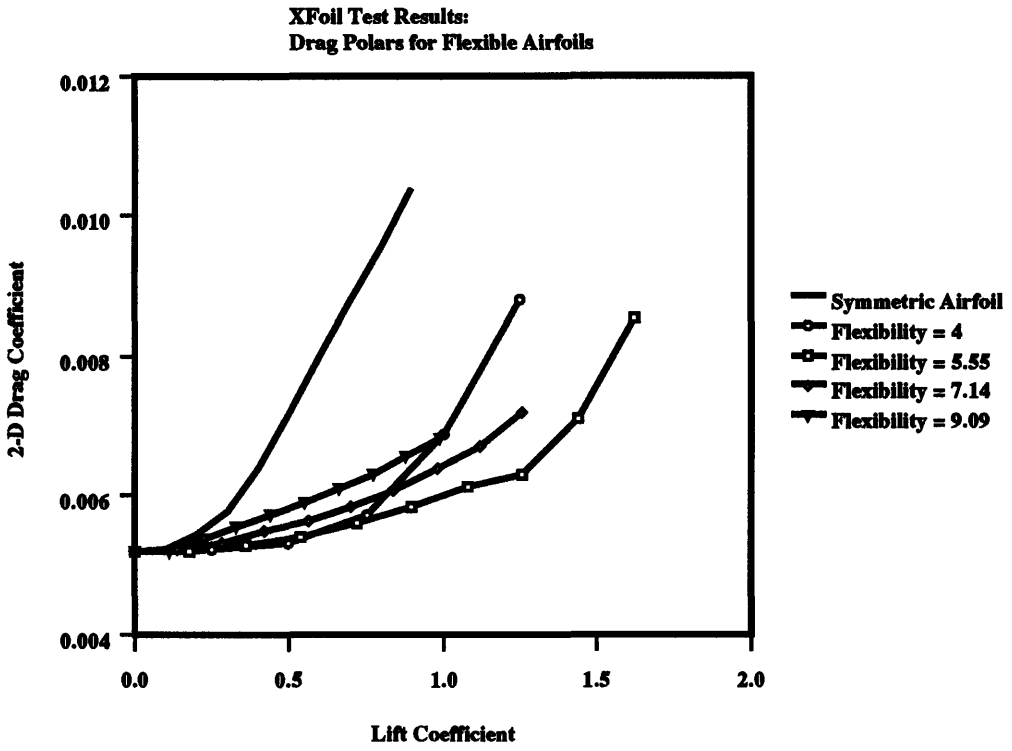

Figure 2-6: XFOIL Results: Drag Polars for Viscous Airfoils

1/4 by angle of attack. The slope of this optimal lift curve is approximately 3 times greater than the rigid airfoil lift curve slope.

2.4 Three-Dimensional Extension

Airfoil theory gives a great deal of information about the flow over the wing in terms of lift, but cannot account for the span affects on the flow and the resulting induced drag. The flow over finite span wings differ from the flow over airfoils because the lift is zero at the wing tips and varies along the span of the wing. The spanwise variation in lift results in a sheet of vortices trailing downstream from the wing. This shed vorticity results in a downward fluid velocity often referred to as *downwash.* The downwash velocity adds to the freestream velocity causing a change the apparent angle of attack often referred to as the induced angle of attack, α_i. This induced angle of attack changes the amount of lift that the wing generates as well causing induced drag.

The performance of finite wings is affected by the induced downwash. The induced angle of attack reduces the angle of attack of the wing thereby reducing the lift. However, since the actual angle of attack, α_a, of the wing is referenced to the far field flow (which remains unchanged), the wing appears to have lower lift than airfoil theory predicts and the slope of the lift curve for the wing is reduced. This effect is shown in Figure 2-7.

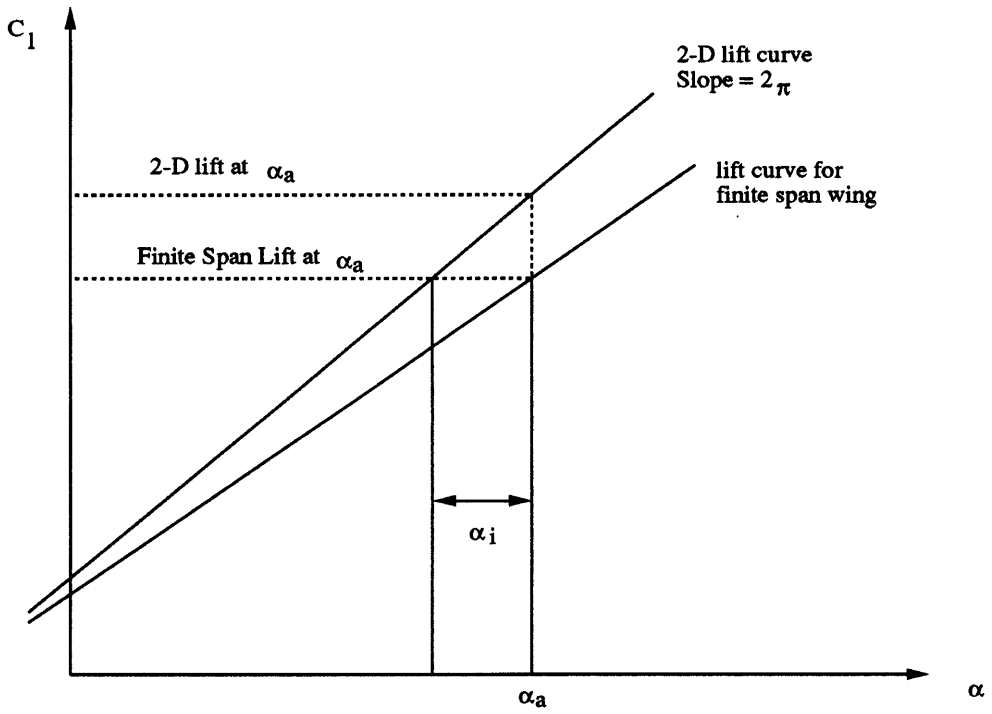

Figure 2-7: Lift curve for a Finite Wing

The magnitude of α_i depends on the strength of the downwash with respect to the free stream strength. The downwash depends on the gradient of the spanwise loading of the wing. Higher aspect ratio wings have lower spanwise loading gradients and thus smaller downwash and resulting in a smaller induced angle of attack for a given lift coefficient. The higher the aspect ratio of the wing, the smaller the induced angle of attack will be in relation to the geometric angle of attack, and thus the closer its lift curve slope will be to the theoretical two-dimensional slope of 2π.

The minimum induced drag occurs when the downwash is a constant value across the wing. This occurs when the spanwise lift distribution is elliptical as shown in

Figure 2-8. Rigid wings have been designed with some combination of spanwise chord distribution, twist distribution or camber distribution. An elliptic chord distribution with no twist or camber produces an elliptic lift distribution for all angles of attack. However, this uncambered wing will, in general, not be as efficient as a properly designed camber wing for the same application. However, a fixed camber distribution that produces an elliptic lift distribution for one angle of attack will, in general, not produce an elliptic lift distribution for other angles of attack.

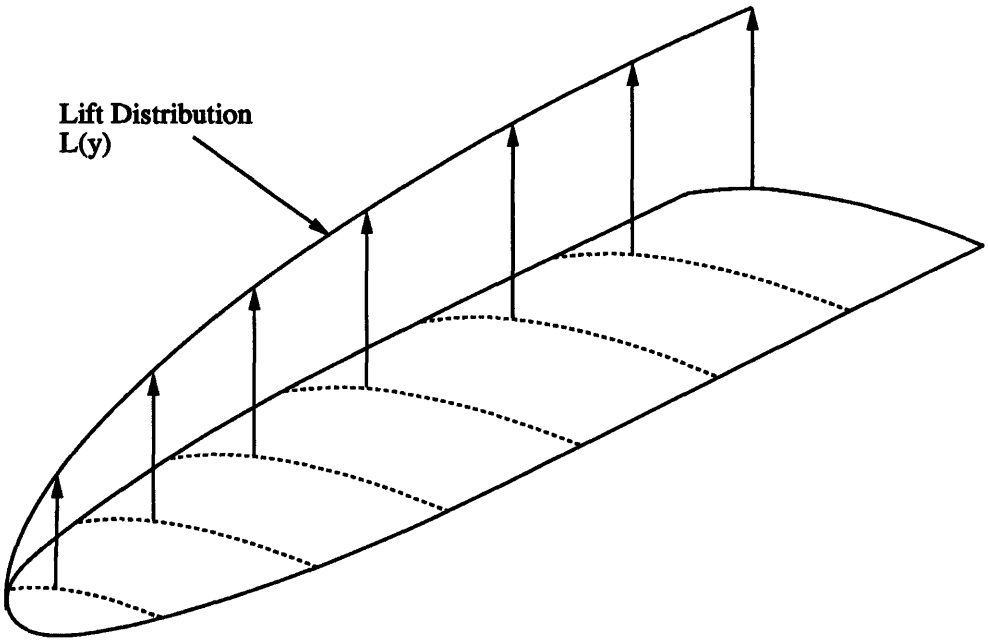

Figure 2-8: Elliptic Lift Distribution for a Finite Wing

For such an elliptically loaded wing, the lift curve slope is given by

$$m = \frac{m_0}{1 + \frac{m_0}{\pi AR}} \tag{2.14}$$

where m is the lift curve slope for the finite span wing, m_0 is the 2π theoretical two-dimensional lift curve slope and AR is the aspect ratio of the wing.

Tapered planforms can very nearly match the elliptic span loading. According to Glauert [4], a tip chord to root chord ratio between 0.3 to 0.5 produces the best

approximation of an elliptic span loading. The lift curve slope for a finite span tapered planform is shown compared to that of an elliptic planform over a range of aspect ratios in Figure 2-9.

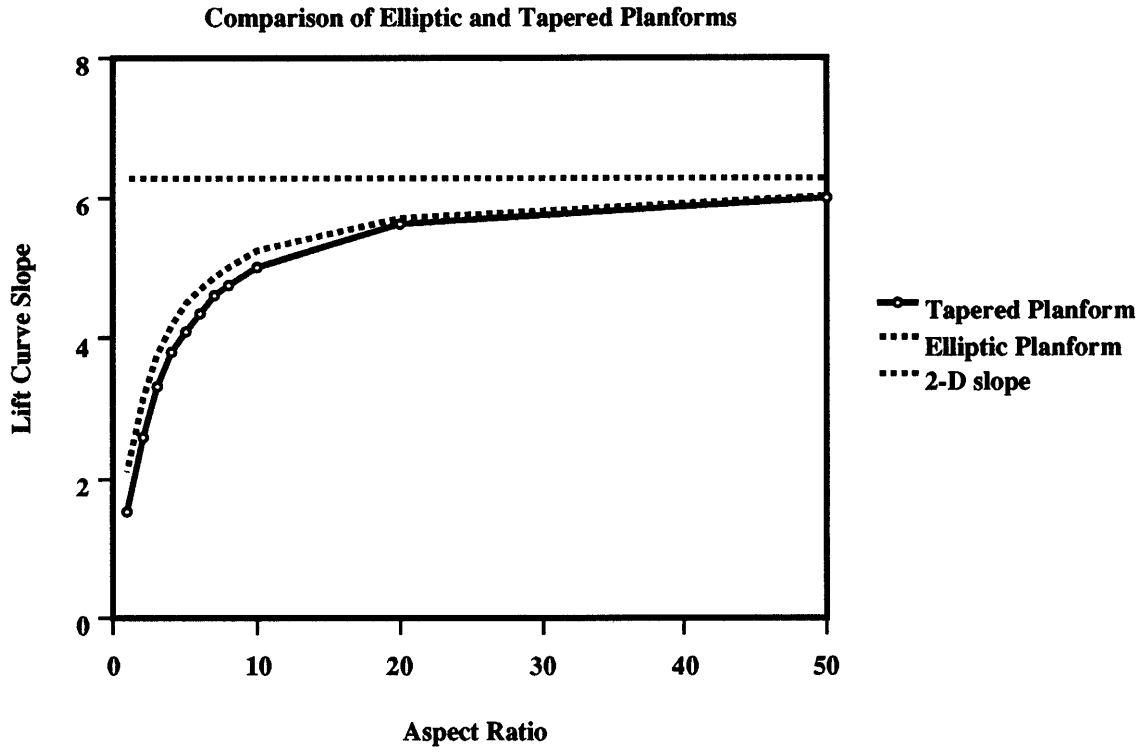

Figure 2-9: Lift Curve Slopes of Tapered and Elliptic Planforms

2.4.1 Flexible Wings of Finite Span

The performance of finite span flexible wings are affected in much the same way as rigid wings. Downwash affects the lift curve of the flexible wing in the same way as it affects rigid wings. The lift curve slope is reduced and induced drag is formed. However flexible wings have a theoretical two-dimensional lift curve slope greater than 2π, so it is possible for a finite span wing to have a lift curve slope greater than 2π as well.

However the effective strength of the flow changes as well when the aspect ratio changes. This changes the critical stiffness value, K_{crit}. For high aspect ratio flexible wings, this effect is summarized in Equation 2.15 from as defined by Widnall *et. al.*

in [10].

$$K_{wing} = K_{airfoil}\,(1 - \frac{1.3}{AR}) \tag{2.15}$$

Thus, $K_{crit\ wing}$ is decreased for a finite span wing.

This theory was developed assuming that each spanwise cross-section of the plate behaved like an ideal two-dimensional plate and assumed the proper chordwise bending for the local loading only. However, in a real wing, the plate is continuous and thus the bending at any point along the plate will be affected by the loading over the entire plate (See Mansfield [6]). For high aspect ratio wings, the gradient of the loading in the spanwise direction are much less steep and the spanwise stations are able to more closely conform to the predicted beam behavior. Lower aspect ratios on the other hand, have very steep gradients in the load and thus the camber response conforms less closely to the local loading.

2.4.2 Effective Stiffness

The question of the determining the stiffness parameter for a finite span wing has been addressed by Widnall *et. al.* in [10]. The stiffness of the wing is determined by an effective stiffness test and non-dimensionalized in the same way as the two-dimensional stiffness parameter. This method involves applying a load to the wing and measuring the deflection of the wing. Specifically, the test involves applying a uniform distributed span load, $P(load/unit\ length)$, to a line that lies halfway between the axis of rotation of the two spars as Shown in Figure 2-10. The effective stiffness of the wing, S_{eff}, is then given in terms of the deflection at the midspan, $w_{midspan}$, as

$$S_{eff} = \frac{P}{w_{midspan}}\,. \tag{2.16}$$

The effective stiffness gives a single stiffness value for a wing that may or may not have a constant value for K over the span. The choice of measuring the deflection at the midspan rather than the root or tip is relatively arbitrary. However, this convention

is used by Widnall *et.al.* in [10], and is presented here to keep notation consistent.

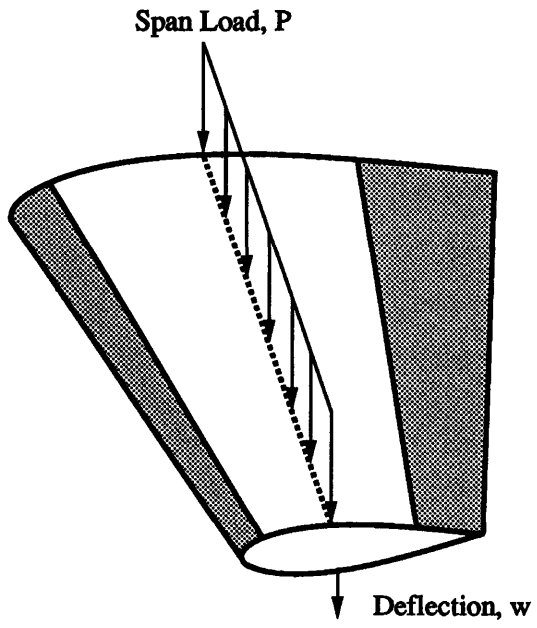

Figure 2-10: Effective Stiffness Test Setup

The critical dynamic pressure of the wing, q_{crit} can be determined from the effective stiffness by

$$q_{crit} = AS_{eff}(\frac{1}{1-\frac{1.3}{AR}}) . \tag{2.17}$$

where A is a coefficient around 0.1.

Since Real wings are constructed from a particular material with a particular elastic modulus, thickness distribution and spar placement, once it has been constructed, it is virtually impossible to modify the structural properties and in particular the plate stiffness. For such a real wing, the stiffness changes as the dynamic pressure changes rather than the plate stiffness. Thus, the critical stiffness, K_{crit} is related to a critical dynamic pressure, q_{crit}. The critical stiffness for the wing, $K_{crit\ wing}$ is given as

$$K_{crit\ wing} = \frac{D}{q_{crit}\,(\frac{c}{2})^3} \tag{2.18}$$

In general, the exact value of K_{crit} for a given wing planform should be determined numerically or experimentally, but the effective stiffness test provides a good estimate for the cases where numerical or experimental analysis is unavailable.

Chapter 3

Numerical Methodology

The study of the behavior fo flexible wings is accomplished by modifying and combining two existing computer programs to solve for the steady aeroelastic behavior of the flexible wings. The Fluid Dynamics are modeled with a vortex lattice program originally coded by Harold Youngren and the Structure is modeled in the ADINA finite element program. The vortex lattice program solves for the aerodynamic loads due to an inviscid flow over the wing. These loads are then passed to the finite element program, ADINA, that models the structural behavior of the wing. The ADINA program solves for the linear elastic static response of the wing structure to the steady aerodynamic loads. The static deflection state is then passed back to the vortex lattice program which solves for a new set of loads given the new wing geometry. The new loads are passed to the finite element program and it solves for a new deflection state. This process continues until the solution converges to a steady equilibrium state.

3.1 Vortex Lattice Aerodynamic Model

The potential flow over a thin wing can be modeled by a distribution of vorticity on the surface of the wing and the corresponding vorticity shed into the wake (See [8]). The vortex lattice program discritizes the vorticity into a finite number of bound "horseshoe" vortices which have a vortex segment bound to the surface of the body

and two trailing segments that extend downstream with the wake. The circulation of each segment of the horseshoe vortex is the same such that the correct amount of vorticity is shed into the wake from the vortex according to Helmholtz's law. The total circulation of the wing is then modeled by a group of these horseshoe vortices that are distributed over the surface in both the chordwise and spanwise directions. The vorticity on the wing at any point is then modeled by varying strengths of the bound segments of the horseshoe vortices near that point. From the vortex distribution and strengths, the lift and drag of the wing can be modeled in a discrete set of loads.

3.1.1 Geometry

The wing is represented in a 3-D cartesian space with the x axis pointed downstream along the root chordline, the y axis pointed in the right spanwise direction and the z-axis pointed up. The origin is located at the leading edge of the root of the wing. The freestream vector is assumed to be at a small angle to the x-axis allowing the use of small angle linearizations. The leading edge of the wing can be swept (an angle to the y-axis) and the wing can have dihedral out of the $x - y$ plane.

The full wing planform is symmetric across the $x - z$ plane. The full load state can be determined from the load state on only one half of the planform (in this case the $+y$ half). The load on the other half of the planform is the mirror image of that load state. Thus by treating the $x - z$ plane as a symmetry plane, only half of the wing needs to be constructed. This half, referred to as the real wing, is constructed by specifying the geometric placement of the vortices and the collocation points. The other half of the planform, referred to as the image wing, is constructed by the enforcement of a reflective boundary condition on the $x - z$ plane.

The wing is sectioned into spanwise strips. Each of these strips is represented by the chordline at each edge. The edges of these strips are parallel to the $x - z$ plane but may be at a different angle of attack than the root chordline. The camberline is prescribed by a set of (x, y, z) coordinates at the edge of each strip. Thus, all geometric considerations such as sweep, twist, and dihedral can be accounted for. The spanwise geometry is assumed to be linear between the strips.

The strip is then divided into a set of chordwise panels. A vortex is placed at the 1/4 chord point of each panel and extends from the 1/4 chord point of root edge of the panel to the 1/4 chord point of the tip edge of the panel. Thus it need not be parallel to the y-axis or leading edge of the panel. It is also not necessary for the bound segment to be perpendicular to the trailing segments of the horseshoe vortex. The vortex lies in the $x - y$ plane in a purely mathematical sense, but it may be considered to lie on the surface of the wing in order to better visualize the geometry of the lattice. The Geometry for a typical wing is shown in Figure 3-1.

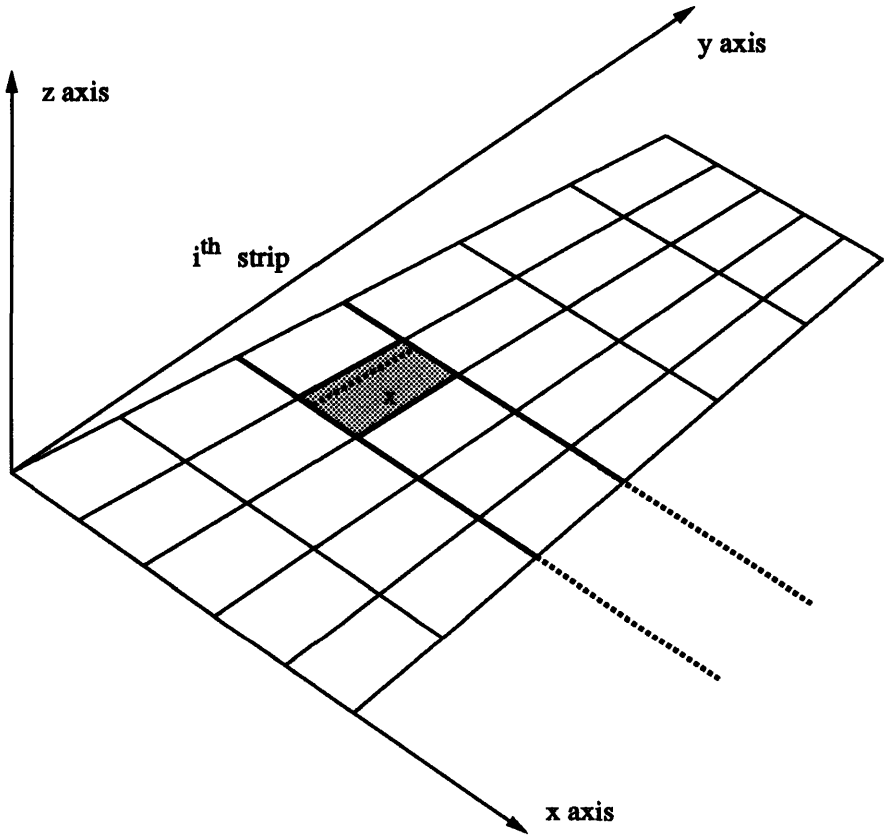

Figure 3-1: Vortex Lattice Geometrical Representation

A "collocation point" is placed at the 3/4 point of the midspan of the panel. Flow tangency is enforced at this point during the solution process. The tangent vector at this point is given by the linear interpolation of the camberline slopes at the 3/4

chord point of the two edges of the panel. Since the camberline data set is made of discrete (x, y, z) points, the slopes are interpolated from the data set by the use of cubic splining. Again, this point lies on the $x - y$ plane for purely mathematical purposes, but may be considered to lie on the surface of the wing for visualization purposes.

In order to accurately represent the flow, the corners of the panels in one strip match with the corners of the panels in the next strip. Thus there are the same number of vortices in each strip and the coordinate of the tip end point of the bound segment of a vortex in one panel matches the root coordinate of the bound segment of a vortex in the next panel. Thus there are a set of continuous vortex segments extending form the root to the tip that vary in strength in the spanwise direction and shed the differential vorticity downstream.

3.1.2 Formulation of the Vortex Lattice

Once the geometry of the lattice has been established, each of the horseshoe vortices can be described by the location of the two endpoints of the bound segment of that vortex, $\vec{r_1}$ and $\vec{r_2}$. The velocity vector $\vec{u}$ at any point in the flow due to the circulation around the vortex can be calculated using the Biot-Savart Law

$$\vec{u} = \frac{\Gamma}{4\pi} \int \frac{\vec{ds} \times \vec{r}}{\vec{r}^3} \tag{3.1}$$

and integrating along the three segments of the horseshoe vortex. By assuming a unit circulation strength, we can determine the influence of that horseshoe vortex on each of the control points. It is also easy to calculate the influence of an image vortex on the control points by setting the y coordinate of the endpoints to be the negative of the actual vortex. By calculating the influences for each of the vortices, an "influence coefficient matrix" can be constructed.

3.1.3 Determination of vortex strength

The actual strengths of each of the vortices should cause the flow to be tangent to the surface at each of the collocation points. The normal vector to the surface at each of the collocation points can be determined from the geometry. By setting the vector dot product of the normal vector with the velocity vector that is induced by the vortices to be zero, the flow is enforced to be tangent to the surface. Since the induced velocity is caused by all the vortices, the flow tangency at any control point can be expressed by a linear equation involving all N vortices. The N equations for the N control points, form a $N \times N$ system of linear equations that can be solved simultaneously for the N vortex strengths. In the program, the solution to this matrix equation is found using Gaussian Elimination since the Matrix is, in general, fully populated.

3.1.4 Solution and Discrete Forces

The strength of a given vortex is related to the lift force it generates by the Kutta-Joukowsky Theorem. Given the bound segment of the horseshoe vortex, $\vec{c}$, is the vector sum of the position vectors of the endpoints, $\vec{r_1}$ and $\vec{r_2}$, as

$$\vec{c} = \vec{r_2} - \vec{r_1}. \tag{3.2}$$

The force vector that the m^{th} vortex generates is then given by

$$\vec{F_m} = \Gamma_m \vec{u_m} \times \vec{c_m} \tag{3.3}$$

where $\vec{u_m}$ is the total velocity vector and Γ_m is the vortex strength of the m^{th} vortex.

These discrete forces are stored so that they can be sent to the finite element program. The finite element program, takes as an input, the modulus of the material. This modulus is expressed in a dimensional way, so in order to describe the relationship of the loads to the stiffness of the wing in terms of the stiffness parameter, K, the loads need to be dimensionalized. The dynamic pressure and lift coefficient are

chosen so that the total lift is 100.

3.1.5 Total Forces and Non-Dimensional Force Coefficients

Summing the discrete force vectors gives the total force on the wing. The total force of the full wing takes into account the image half of the wing as well as the real half.

$$\vec{F_{total}} = 2 \sum_{m=1}^{N} \vec{F_m} \tag{3.4}$$

This total force can be resolved into drag and lift forces by taking the dot products of the Total force vector with the freestream and its normal respectively.

$$\vec{L} = \vec{F_{total}} \cdot [-(\sin\alpha)\hat{i} + (\cos\alpha)\hat{k}] \tag{3.5}$$

$$\vec{D} = \vec{F_{total}} \cdot [(\cos\alpha)\hat{i} + (\sin\alpha)\hat{k}] \tag{3.6}$$

The lift and drag forces can be expressed more generally by non-dimensional force coefficients. The lift coefficient is defined as

$$C_L = \frac{L}{\frac{1}{2}\rho V_\infty^2 S_{ref}} \tag{3.7}$$

where L is the total lift, $\frac{1}{2}\rho V_\infty^2$ is the free stream dynamic pressure and S_{ref} is the surface area of the wing. Similarly, the drag coefficient is defined as

$$C_D = \frac{D}{\frac{1}{2}\rho V_\infty^2 S_{ref}} \tag{3.8}$$

where D is the total drag.

3.1.6 Trefftz Plane Drag Calculation

The drag calculated by Equation 3.6 is very sensitive to numerical errors. In most cases, the force vectors near the leading edge of the wing have substantial forward

components and the vectors near the trailing edge of the wing have substantial aft components. These should mostly cancel out leaving only the induced drag component of the total force. A small error in these vectors, however, could result in a large error in the drag vector given all of the vector cancellation. Thus the drag calculation has a very low accuracy.

One solution to this problem is to calculate the induced drag by looking at the induced velocities in the wake far downstream from the wing. This is most commonly done by constructing a plane, known as the *Trefftz Plane*, parallel to the $y - z$ plane in the far field wake as shown in Figure 3-2, and looking at the induced flow velocity in that plane.

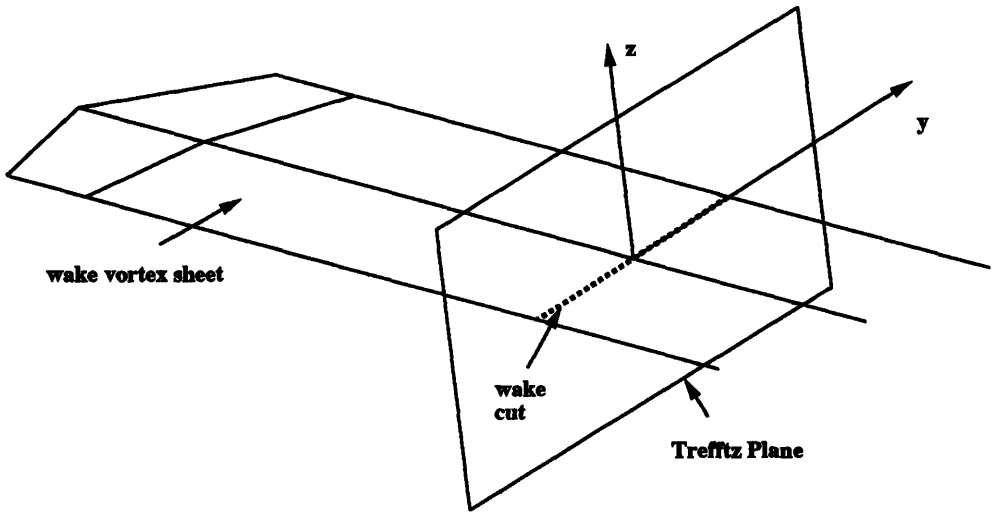

Figure 3-2: Trefftz Plane Intersecting Wake Vortex Sheet

The work done by the induced drag force can be calculated from the residual velocity vector, $\vec{w}$. The induced velocity field $\vec{w}$ is irrotational and can be expressed as the gradient of a crossflow potential.

$$\vec{w} = \nabla\phi \tag{3.9}$$

The kinetic energy per unit volume can be written as simply $\frac{1}{2}\rho\|\vec{w}\|^2$. Thus the induced drag is simply the integral of the kinetic energy per unit volume over the

entire Trefftz Plane.

$$D = \frac{1}{2}\rho \int\int \|\vec{w}\|^2 \, dy \, dz \tag{3.10}$$

$$D = \frac{1}{2}\rho \int\int \nabla\phi \cdot \nabla\phi \, dy \, dz \tag{3.11}$$

By taking a contour that completely encloses the wake, the area integral becomes, by Gauss's Theorem, a contour integral.

$$D = -\frac{1}{2}\rho \oint \phi \vec{w} \cdot \vec{n} \, ds \tag{3.12}$$

The velocity component of $\vec{w}$ normal to the wake is the same on either side of the wake cut. Thus the contour integral can be changed into a line integral in terms of the potential jump across the wake.

$$D = -\frac{1}{2}\rho \int \Delta\phi \vec{w} \cdot \vec{n} \, dl \tag{3.13}$$

The potential jump, $\Delta\phi$, at any spanwise station of the wake must be equal to the bound circulation, Γ, at the point on the wing directly upstream of that point. Thus it is trivial to calculate the Trefftz Plane drag by taking the integral along the wing of the bound circulation, $\Gamma(y)$.

$$D = -\frac{1}{2}\rho \int \Gamma(y) \, \vec{w} \cdot \vec{n} \, dl \tag{3.14}$$

Given the discrete nature of the circulation distribution on the wing, Γ, at any spanwise station can be expressed as a sum of the horseshoe vortex strengths at that spanwise point. Thus the integral can be evaluated by summing over all of the N bound vortices on the wing.

$$D = -\frac{1}{2}\rho \sum_{n=1}^{N} \Gamma_n \, \vec{w} \cdot \vec{n} \, \Delta l_n \tag{3.15}$$

This total drag can be expressed in terms of the drag coefficient as in Equation 3.8.

Both the trefftz plane analysis and the vector analysis are calculated by the vortex lattice program. Both are given as output for comparison, however it is generally accepted that the trefftz plane analysis gives the better result and this result will be given as the total drag coefficient for the wing in the results.

3.1.7 Vortex Lattice Program Overview

The actual program that is used in this study is a modified version of a vortex lattice program written by Harold Youngren for the Project Athena Todor facility in 1990. The geometric shape of the wing is read into the vortex lattice program from a datafile. The user then inputs the desired lift coefficient and the stiffness of the wing. The program determines the influence coefficint matrix and solves for the vortex strengths at the desired lift coefficient and determines the angle of attack of the reference line at the root of the wing. The program also determines the downwash distribution along the span of the wing and the induced drag of the wing.

The accuracy of the method depends to a large degree on the geometry of the wing and the number and placement of the vorticies. Some of the problem that arise in the accuracy are due to sweep discontinuities at the root and the drastic variation in spanwise loading at the tip (See Moran [8]). Given the low sweep of the wings in this study as well as the large number of vorticies placed on the wing, the method should be quite accurate. In particular, the accuracy of the lift is much better than the accuracy of the drag and by calculating the drag in the Trefftz Plane, much of this inaccuracy is overcome. for the very linearized models in this study, the accuracy of the method is more than adequate.

3.2 Finite Element Model

The elastic response of a structure to an applied load state can be analyzed numerically by breaking the structure into small pieces known as finite elements (See [2]). Each of these finite elements is essentially a small plate acted on by a very simple set of loads applied at discrete points within the element called *nodes*. Since

the elements are simple, it is easy to find their response to the simple load states that can be applied to them. Then the entire structure can be put back together and the more complex real load state applied to it. Each element feels some simple part of that real load and responds accordingly. The response of the entire structure is then the combination of the responses of all the elements put together.

By using the *Principle of Virtual Work*, the general response of each of the elements to imaginary loads can be determined. The response is represented in an influence matrix called the element stiffness matrix. This matrix describes the displacements of each of the nodes of the element to imaginary loads applied to each of the nodes.

By then assembling the elements into a mesh, the response of the entire structure to an imaginary load state is determined. The element stiffness matrices are added together into a much larger global stiffness matrix. This matrix describes the response of each of the nodes in the entire structure to imaginary loads applied at any of the other nodes. The response of the structure to the real load state is then simply a combination of several imaginary load states.

3.2.1 Formulation of the Finite Element Mesh

The elemental boundaries are determined mainly by geometric constraints. A set of points, called *nodes*, are defined on the midplane of the plate. These nodes define the corners of the elements. The elemental boundaries are defined by lines connecting the nodes. There are *nodal degrees of freedom* (d.o.f.s) defined at each node. Theses d.o.f.s define the displacement and rotation of the structure at the nodes.

For the plate bending/stretching case that is modeled here, each node must have 5 d.o.f.s., the 3 displacements (u, v, w) and two rotations (θ_x and θ_y). The displacements u, v and w are in the x, y and z directions respectively, and θ_x and θ_y are the rotations from the x axis and the y axis respectively as shown in Figure 3-3.

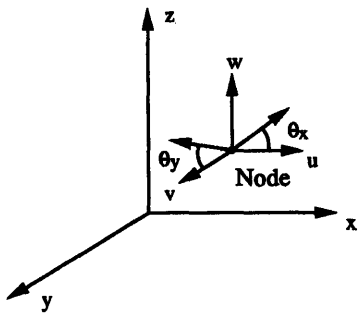

Figure 3-3: Nodal d.o.f.s

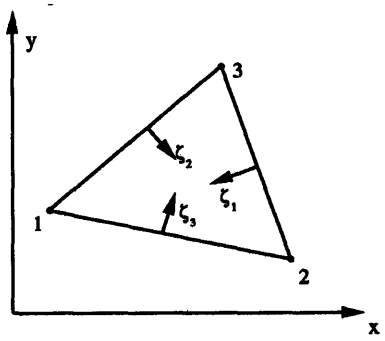

Figure 3-4: Triangular Area Coordinates

3.2.2 Local Element Coordinate System

For the plate structure of the wing, a Finite Element mesh involving 3 node triangular plate elements is utilized. These triangular elements utilize a generalized triangular area coordinate system $(\zeta_1, \zeta_2, \zeta_3)$ as shown in Figure 3-4. Properties of the element such as the displacement, strain or stress are only known at the nodes. The properties of the element can be interpolated within the element by the use of *interpolation functions.* The three node isoparametric triangular element has interpolation functions N_1, N_2 and N_3.

$$N_1 = \zeta_1, \quad N_2 = \zeta_2, \quad N_3 = \zeta_3 = 1 - \zeta_1 - \zeta_2 \tag{3.16}$$

The coordinates within the element are interpolated from the interpolation functions with respect to the coordinates of the 3 nodes, (x_1, y_1), (x_2, y_2) and (x_3, y_3).

$$x = N_1 x_1 + N_2 x_2 + N_3 x_3 \tag{3.17}$$

$$y = N_1 y_1 + N_2 y_2 + N_3 y_3 \tag{3.18}$$

The Jacobian matrix to transform from the $(\zeta_1, \zeta_2, \zeta_3)$ coordinate system to the (x, y) coordinate system is given by

$$J = \begin{vmatrix} \frac{\partial x}{\partial \zeta_1} & \frac{\partial y}{\partial \zeta_1} \\ \frac{\partial x}{\partial \zeta_2} & \frac{\partial y}{\partial \zeta_2} \end{vmatrix} \tag{3.19}$$

For the triangular elements, the determinant of the Jacobian is simply twice the are of the triangle. The shape interpolation functions and the Jacobian matrix describe the relationship between the local coordinate frame of the element and the global coordinate frame of the entire structure.

3.2.3 Element Stiffness Matrix

Each of the elements is described by a element stiffness matrix. For triangular 3 node triangles, the element stiffness matrix describes the response of the structure to imaginary unit loads or *virtual loads* at each of the nodes of the element.

The formulation of the element stiffness matrix comes from the principle of minimum potential energy. The potential energy Π_p is defined as

$$\Pi_p = U - W \tag{3.20}$$

where U is the internal strain energy of the structure and W is the work done by the applied loads. U and W are defined as

$$U = \int_V \frac{1}{2} \{\epsilon\}^T [E] \{\epsilon\} \, dV \tag{3.21}$$

$$W = \int_A p_z(x, y) \, w \, dA \tag{3.22}$$

where $\{\epsilon\}$ is the strain vector, $[E]$ is the elasticity matrix, p_z is the loading and w is the deflection.

The variational form of the potential energy equation is given as

$$\delta\Pi_p = \delta U - \delta W \tag{3.23}$$

The structure will tend toward a minimum potential energy state. This minimum energy state can be found by taking $\delta\Pi_p = 0$. The element stiffness matrix $[k]$ is

derived from the internal strain energy term, δU.

The plate that models the flexible ceneterline of the wing, undergoes stretching as well as bending due to the loads that are applied to it. The structural problem of plate bending and plate stretching are, for an isotropic material, separable. The plate bending case uses the plate bending modulus matrix, $[D]$, to relate the out of plane displacements w, θ_x and θ_y to the transverse loading p_z. The plate stretching case uses the plate stretching modulus matrix, $[E]$, to relate the in-plane displacements u and v to the in-plane loading p_x and p_y. As long as the deflection state is small relative to the plate dimensions, these problems remain separate and the FEM formulation for each can be done separately.

For the bending plate case, the internal energy, U, for the element is formulated as

$$U = \frac{1}{2} \int \int_A [\kappa]^T [D][\kappa] \, \|J\| \, d\zeta_2 \, d\zeta_1 \tag{3.24}$$

The curvature matrix, $[\kappa]$, is defined as

$$\kappa = \begin{vmatrix} -\frac{\partial^2 w}{\partial x^2} \\ -\frac{\partial^2 w}{\partial y^2} \\ -2\frac{\partial^2 w}{\partial x \partial y} \end{vmatrix} = [M]\vec{q} \tag{3.25}$$

$[M]$ is defined from geometry as

$$M = \frac{1}{4A^2} \begin{vmatrix} -(y_3 - y_1)^2 & -(y_2 - y_1)^2 & 2(y_2 - y_1)(y_3 - y_1) \\ -(x_3 - x_1)^2 & -(x_2 - x_1)^2 & 2(x_2 - x_1)(x_3 - x_1) \\ 2(x_3 - x_1)(y_3 - y_1) & 2(x_2 - x_1)(y_2 - y_1) & -2[(x_3 - x_1)(y_2 - y_1)(x_2 - x_1)(y_3 - y_1)] \end{vmatrix} \begin{vmatrix} \frac{\partial^2 N}{\partial \zeta_1^2} \\ \frac{\partial^2 N}{\partial \zeta_1^2} \\ \frac{\partial^2 N}{\partial \zeta_1 \partial \zeta_2} \end{vmatrix} \tag{3.26}$$

Then the energy, U, can be written

$$U = \frac{1}{2}\vec{q}^T [\int_0^1 \int_0^{1-\zeta_1} [M]^T [D][M] \, d\zeta_1 \, d\zeta_2] \vec{q} \tag{3.27}$$

giving $U = \frac{1}{2}\vec{q}^T [k]_b \vec{q}$, where $[k]_b$ is the bending stiffness matrix

$$k_b = \int_0^1 \int_0^{1-\zeta_1} [M]^T [D][M] \, d\zeta_1 \, d\zeta_2] \tag{3.28}$$

The bending stiffness matrix, $[k]_b$, is a 9x9 matrix relating the three out-of-plane deflections, w, θ_x and θ_y, for the three nodes to the out-of-plane load, p_z, and the applied moments, M_x and M_y, at the three nodes.

For the stretching plate case, the internal energy, U, for the element is formulated as

$$U = \frac{1}{2} \int \int_A [\epsilon]^T [E][\epsilon] \, \|J\| \, d\zeta_2 \, d\zeta_1 \tag{3.29}$$

Formulating the internal energy equation into the form $U = \frac{1}{2}\vec{q}^T [k]_s \vec{q}$ gives

$$k_s = \int_0^1 \int_0^{1-\zeta_1} [B]^T [E][B] \, t \, \|J\| \, d\zeta_2 \, d\zeta_1 \tag{3.30}$$

where t is the thickness of the element, $\|J\|$ is the determinant of the Jacobian Matrix and $[B]$ is the spatial derivative matrix

$$B = \begin{vmatrix} 1 & 0 & 0 & 0 \\ 0 & 0 & 0 & 1 \\ 0 & 1 & 1 & 0 \end{vmatrix} \begin{vmatrix} [J]^{-1} & 0 \\ 0 & [J]^{-1} \end{vmatrix} \begin{vmatrix} \frac{\partial N_1}{\partial \zeta_1} & 0 & \frac{\partial N_2}{\partial \zeta_1} & 0 & \frac{\partial N_3}{\partial \zeta_1} & 0 \\ \frac{\partial N_1}{\partial \zeta_2} & 0 & \frac{\partial N_2}{\partial \zeta_2} & 0 & \frac{\partial N_3}{\partial \zeta_2} & 0 \\ 0 & \frac{\partial N_1}{\partial \zeta_1} & 0 & \frac{\partial N_2}{\partial \zeta_1} & 0 & \frac{\partial N_3}{\partial \zeta_1} \\ 0 & \frac{\partial N_1}{\partial \zeta_2} & 0 & \frac{\partial N_2}{\partial \zeta_2} & 0 & \frac{\partial N_3}{\partial \zeta_2} \end{vmatrix} \tag{3.31}$$

The stretching stiffness matrix, $[k]_s$, is a 6x6 matrix relating the two in-plane deflections, u and v, for the three nodes to the in-plane loads, p_x and p_y at the three nodes.

The plate element must solve for both the bending and stretching of the structure. Thus the element stiffness matrix needs to have both the bending and stretching terms in it. By defining the element d.o.f. vector, $\vec{q}_e$, to be

$$q_e = \lfloor u_1, v_1, u_2, v_2, u_3, v_3, w_1, \theta_{x,1}, \theta_{y,1}, w_2, \theta_{x,2}, \theta_{y,2}, w_3, \theta_{x,3}, \theta_{y,3} \rfloor \tag{3.32}$$

then the element stiffness matrix, $[k]_e$, can be formed by combining the bending and stretching element stiffness matrices $[k]_b$ and $[k]_s$ to form a 15 x 15 matrix.

$$k_e = \begin{vmatrix} k_s & 0 \\ 0 & k_b \end{vmatrix} \tag{3.33}$$

3.2.4 Global Stiffness Matrix

The element stiffness matrix for each element relates the nodal responses of that element to the applied nodal loads. By combining all of the element matrices together such that the global d.o.f.s match, the global stiffness matrix can be constructed. This global stiffness matrix relates the global displacements to the global loading state.

A given non-boundary node (one that is shared by more than one element), there are terms in the element stiffness matrices of all the elements that share that node which relate the displacement of that node to the forces applied at that node. The terms in the global stiffness matrix for that node are then simply the sum of the elemental terms. Each term of the global stiffness matrix is constructed by summing all the terms that relate a given force to a given displacement of a given node.

3.2.5 Solution Method

Once the Global stiffness matrix is constructed, the solution involves simply finding the solution of the system of algebraic equations that are given by the matrix.

The work term, δW, gives the discritized load vector, $\vec{Q}$. Thus from the global stiffness matrix, $[K]$, the d.o.f. vector, $\vec{q}$, and the load vector, $\vec{Q}$, we get the matrix equation

$$[K]\vec{q} = \vec{Q} \tag{3.34}$$

This matrix is solved by a general matrix solution technique. The solution is given in terms of the d.o.f. vector, $[q]$. The displacements u, v and w for each of the nodes are given in the solution vector, $[q]$. These displacements are printed out to a data file so that they can be read by the input routine of the vortex lattice program.

3.2.6 ADINA program overview

The finite element program used for this study is the ADINA program developed by ADINA R&D Inc.. The ADINA (Automatic Dynamic Incremental Non-Linear Analysis) package is capable of performing finite element calculations for a wide variety of problems, however, a very limited set of the capabilities of the package are needed for this study. The program itself is licensed to the MIT Supercomputing Facility and has been compiled to be run on the CRAY X-MP. For this study, access to the CRAY X-MP has been through the experimental Transparent Computing Module that has been developed by the MITSF.

The ADINA package consists of three programs, ADINA-IN, ADINA and ADINA-PLOT. ADINA-IN is used to setup the Finite Element mesh from inputed geometric and load information. ADINA-IN creates a formatted database containing all the information so that a solution to the problem can be determined by ADINA. ADINA-PLOT takes that solution and presents it in graphical or tabular formats that give information about the problem that is requested by the user.

ADINA-IN exectues a series of commands contained in a ".in" file. This file contains all the geometric information about the problem as well as the boundary conditions loading and material type. It also contains information on how the mesh should be created and what type of elements should be used. This study is interested in the linear elastic behavior of flexible wings only. Thus, all materials have been specified as ELASTIC in the ADINA input files such that the model will respond in a completely linear way to the loading. The wing has been modeled with 3-node, triangular PLATE elements. The formulation of these elements is done automatically by the ADINA-IN program.

ADINA is the actual finite element solver. It takes the geometric information from the ADINA-IN database and constructs the element stiffness matricies for all of the elements. It then assembles the global stiffness matrix from the element stiffness matricies. By inverting this matrix and the corresponding load vector, ADINA solves for the deflections of all the nodal d.o.f.s for the structure.

This solution is formatted into a useful, readable output by the ADINA-PLOT

program. This program reads commands form a ".plot" file that contains information about what aspects of the solution the user would like to study. In many cases, numerical information about the structure such as the deflection or stresses are desired and the ADINA-PLOT program can write a ".plist" file that contains such information.

3.3 Interaction of Numerical Programs

For the problem of the flexible wing solved by these numerical schemes, there is an interaction of the aerodynamic forces and the structure. This interaction must be modeled by the numerics. This interaction is handled by the programs in an iterative fashion rather than solving the two systems simultaneously. The programs pass back and forth information on the loads and the shape.

3.3.1 Geometric Relationship

To ease the interaction of the two numerical schemes, the mesh nodes of the finite element portion of the program are chosen so as to match the load points of the vortex lattice program. This allows trivial interaction of the two schemes. A node of the finite element mesh is placed at center of the bound segment of each of the horseshoe vortices. Thus, the lift force produced by that vortex acts directly at the node.

Many other nodes are placed so as to fill out the mesh. The placement of these nodes is such that they lie on the spanwise edges of the vortex lattice strips. Thus, the new camber distribution of the wing at each of these spanwise stations can be easily splined directly from the nodal displacements at that station.

The vortex lattice itself is geometrically constructed so that the finite element mesh that is constructed from it is well formulated. There are panel edges that correspond directly to the locations of the axle boundary conditions. The panels are placed such that the mesh has a good resolution in the flexible bending section of the wing.

3.3.2 VL: Lift Load Information

The vortex lattice program generates a set of discrete aerodynamic loads that act on the lifting wing. These loads act at the center of the bound vortex segment of each of the horseshoe vortices. These load forces can be passed directly to the Finite Element Program.

The vortex lattice is initialized with the the planform information and initial camber information. For most of the data runs, the initial camber state is assumed to be that of an uncambered wing. Thus the performance information can be assumed to be related for both positive and negative loading cases.

Subsequent iteration steps read geometric information from the finite element program. The finite element routine passes displacement information to the vortex lattice program that it then turns into planform and camber information.

The vortex lattice program is set up to maintain a constant lift coefficient throughout a data run. Thus the angle of attack will change at each iteration step as the camber changes. This is necessary to prevent divergent behavior in the wing. It also models the response of a real wing more accurately since real wings have a finite load to lift and must respond to that lift requirement. It should be noted that this is different from the behavior of such wings in wind tunnel experiments since in wind tunnels, the angle of attack is usually fixed and the lift measured.

The vortex lattice program is a modified version of a progam that was originally coded by Harold Youngren for use in the MIT Project Athena Todor package. The core section of the program that builds the influence coefficient matrix and solves for the vortex strength distribution is largely unchanged from the original program. However, to deal with the special requirements of the flexible wings, the geometry input and output routines of the program have been significantly altered.

The program has been modified to maintain a constant lift coefficient throughout the iterative solution process. Since the vortex lattice program models the wing without any viscosity, the phenomenon of stall is completely ignored as are any other nonlinearities in the lift curve of the wing. Thus the program has been easily be modified to find the angle of attack from the specified lift coefficient by a modified

linear interpolation method of the angle of attack along the lift curve.

The input routine has been modified so that the exact placement of the vortices is possible. This is necessary so that the vortices will be properly aligned near the spars and will have consistent distributions elsewhere. The placement of a vortex in the lattice can be explicitly defined in the geometry input datafile by the cartesian coordinates of the endpoints of the bound segment of the horseshoe vortex.

The output routine has been modified to write the ADINA-IN file that will allow the finite element program, ADINA, to read in the wing shape, material properties, boundary conditions and loads. This routine specifies the details of the FEM mesh such that the nodes of the mesh correspond to specific features of the vortex lattice mesh. FEM nodes are placed along the chord strip edges and at the midpoints of each of the bound vortices.

A second input routine has been added to read in the wing shape and camber from the ADINA output file. The output from ADINA gives the coordinates of each of the nodes in the finite element mesh. Since the mesh was constructed from information from the vortex lattice program, the same information can be used to interpret the ADINA output file and thus the new wing shape can be constructed based on that file.

3.3.3 FEM: Displacements

The finite element program generates a deflection state based on the load information passed to it by the vortex lattice program and material information supplied by the user. The program solves for the displacements of the nodes that make up the finite element mesh. These displacements are then given back to the vortex lattice program as the loaded geometry for the wing.

The nodal locations for the finite element solution are chosen to correspond directly to the loading points and other geometric information in the vortex lattice program. Thus the nodal displacements from the finite element program directly relate to changes in the geometry of the vortex lattice.

3.3.4 Iteration of Solution

The solution process proceeds in an iterative way by passing load information from the vortex lattice program to the finite element program and passing geometry information from the finite element program back to the vortex lattice program. The process starts with an undeformed wing geometry. The lift coefficient of the wing is then set and the vortex lattice program finds the discrete lift loads. These loads are passed to the finite element program which solves for the deflection of the wing. The new geometry is passed back to the vortex lattice program which finds the new discrete load distribution. The new loads are passed to the finite element program which finds a new deflection state. This process continues until the solution converges to a stable lift and geometric state. This solution is assumed to be the steady state response of the flexible wing at that load coefficient.

The iteration proceeds with a high rate of convergence. The initial step provides a large change in camber from the undeformed state. since the magnitude of the total lift load does not change from iteration to iteration, the subsequent camber changes of the wing become much smaller with each iteration step. Essentially the camber changes position but not in magnitude with each additional iteration.

3.3.5 Special considerations for a flexible wing

Traditional tests to determine the lift curves for wings set the angle of attack and measured the resulting lift. For a flexible wing with a very low stiffness parameter, this would result in unstable modes where the lift due to camber would increase faster than the restoring force in the plate due to the bending. Thus the camber would increase until some physical restraint stopped it. By fixing the lift of the airfoil, by setting the lift coefficient, the amount of camber would be relatively stable and the angle of attack would vary until an equilibrium was reached. In this way, the instabilities would be avoided.

A dynamic pressure is chosen for the method so that the vortex strengths can be expressed in terms of force rather than force coefficients. Similarly the modulus of

the plate is chosen such that the plate stiffness compared to the dynamic pressure gives the desired stiffness. In this way actual loads and material data can be sent to the FEM program. The units cancel out in the analysis when the non-dimensional parameters such as Aspect ratio and the stiffness parameter are use to define the properties of the wing.

The geometry of the two models are specified in such a way as to allow the easy correlating of the discrete loads between the vortex lattice program and the finite element program. A typical paneling scheme for the wings is shown in Figure 4-6 and Figure 4-21. The exact details of the paneling varies from model to model depending on the aspect ratio and the boundary conditions that are chosen for the particular data run.

The Finite Element mesh is constructed by the vortex lattice progam and utilizes very particular geometric information about the vortex lattice. Thye finite element mesh and the lortex lattice are shown together in Figure 3-5. The geometrical placement of the finite element nodes corresponds to particular features of the vorex lattice.

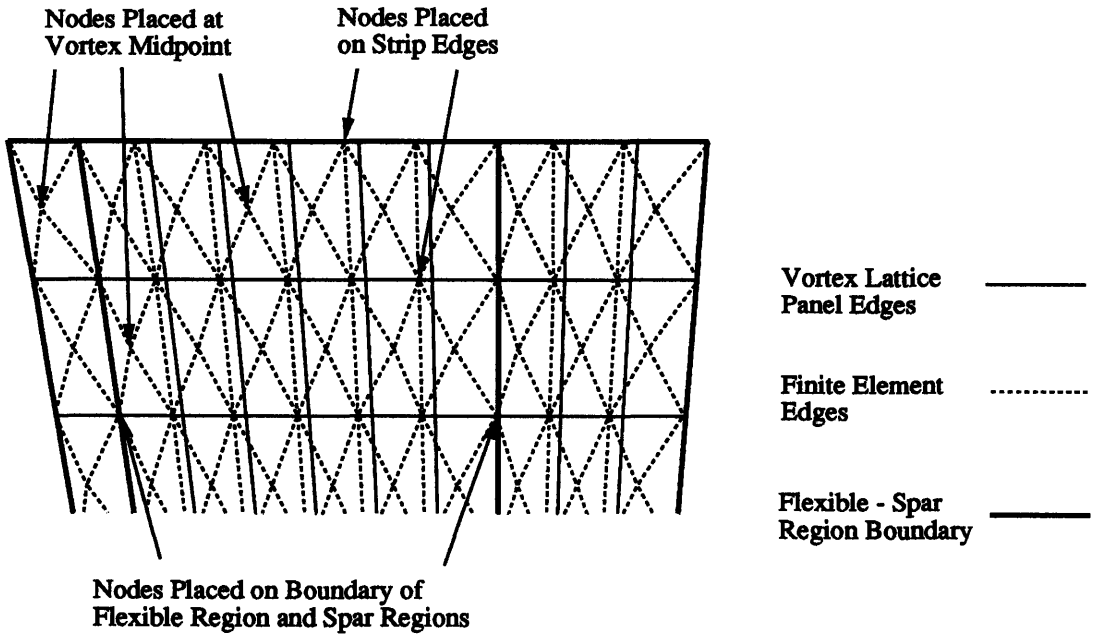

Figure 3-5: Overlay of Finite Element Mesh and Vortex Lattice

Each of the vortices in the vortex lattice program generate a discrete load that

acts through the midpoint of the bound segment of that vortices. In order to easily deal with these loads in the finite element model, nodes of the finite element model are placed at the geometric location of these vortex midpoints. Thus the loads generated by the vortex lattice can be directly applied to the corresponding nodes in the finite element model. The typical placement of these nodes are shown in Figure 3-5.

The remainder of the finite element nodes are placed on the edges of the strips in the vortex lattice model. Thus the displacements at these nodes directly correspond to the chordlines at the strip edges. This allows the vortex lattice program to easily construct the geometry of the deformed wing shape for the next iteration. This is shown in Figure 3-5.

Vortex Lattice panel boundaries as well as Finite Element boundaries are placed in the geometric location of the boundaries between the flexible region and the stiff axle regions in the real wing. This boundary line is shown in Figure 3-5. This boundary is specifically prescribed so that the material discontinuity between the flexible region and the spar regions could be handled by the finite element program. The curvature of the structure in the chordwise direction is typically discontinuous across this boundary due to the material difference. Placing a Vortex lattice panel edge along this boundary allows better resolution of the exact details of the camberline. This interface also corresponds to the axis of rotation of the spars. Having nodes along the axis of rotation allows the displacement of the spars to be specifically measured so that the exact response of the spars can be determined for design purposes.

Chapter 4

Numerical Analysis of Flexible Wings

The numerical methodology described in the previous chapter is used to determine the steady state behavior of a given flexible wing operating at a certain dynamic pressure and lift coefficient. In order to establish general performance characteristics, several different planforms are examined numerically over a range of operating points and the results expressed in terms of the stiffness parameter and the aspect ratio. These results are then used to generate performance curves that describe the behavior of a general flexible wing at any operating point.

Of primary interest in the numerical results is the lift curve slope for a wing. The lift curve for flexible wings differ significantly from those for rigid wings. These calculations develop theoretical lift curves for flexible wings. Traditional lifting line theory calculations provide the lift curve slope of a rigid wing with a given planform. The cambering response of the flexible wing increases the lift curve slope of the wing. Thus the lift curve depends on the stiffness of the wing as well as the planform.

In this study, the drag polars are of secondary interest. Since this is an inviscid calculation, only induced drag is obtained which depends primarily on the span and the span load distribution of the wing. The span load distribution depends mainly on the planform of the wing and varies only slightly due to the camber distribution. Thus, the drag polars should not vary significantly as the value of the stiffness parameter

of a given wing changes.

4.1 Analysis Goals

The numerical analysis is used to calculate the behavior of flexible wings and generate performance curves. The performance curves relate the lift curve slope of a wing to the planform and stiffness parameter and can be used to predict how a wing with given values of each of these parameters will perform. The performance curves are derived from a limited set of planforms, but give general trends for more general flexible wings. Although the inviscid calculations cannot show the increases lift to drag ratio of a cambered wing, they can show the effects of flexibility on the lift curve.

4.1.1 Convergence

The converged solution of the numerical method gives a good approximation to the behavior of the flexible wing at a steady operating point. As with any iterative method, complete convergence is impossible. However, a solution can be said to be converged if the change in a particular parameter per iteration is small enough that this change does not change the solution beyond an acceptable resolution.

For this method, several parameters are measured such as the angle of attack, the induced drag and several other aerodynamic performance factors. Each of these quantities should be constant to within an acceptable change per iteration for a converged solution. The lift coefficient remains constant during the convergence progression, and the changes in camber result in changes in the angle of attack of the wing. Thus the angle of attack is the primary measure of convergence. For this study, the solution is considered to be converged if the angle of attack does not change by more than 0.0001 degrees per iteration. The camber shape of the wing also changes at each iteration. This change in the shape of the wing is measured by the root mean squared change in the z-deflection of the nodes. This error serves as a benchmark quantity by which changes in the wing from one iteration to the next can be measured.

The iteration progression toward the solution also shows the stability of the method and can be related to the stability of real flexible wings. A high rate of convergence indicates a very stable behavior of the real wing, whereas a slower convergence may indicate a less stable wing. The convergence rate should be faster for wings with a higher stiffness parameter. The convergence rate should decrease for wings with very low aspect aspect ratio and for wings below an aspect ratio of about 1.3 the method should not converge at all.

4.1.2 Parameter Range

Several parameters of the wing are specified at the beginning of the solution process. The input datafile into the vortex lattice program contains the planform geometry of the wing. This geometry information includes the aspect ratio of the wing and the boundary conditions. An operating point for the wing of that planform is then defined by the lift coefficient and value of the stiffness parameter. Since the lift coefficient and stiffness parameter account for the dynamic pressure and the chord of the wing in their non-dimensionalizations, the performance of a general wing can be completely described by these parameters.

A set of data points for a range of lift coefficients, stiffness parameters and planforms are needed in order to adequately resolve the performance curves for the wings. To study the effect of stiffness on wing performance, lift curves are generated for each planform for a range of values of the stiffness parameter. Wings with similar planforms and boundary conditions that differ only in aspect ratio are tested to quantify the effects of aspect ratio on the performance as well.

This study also looks at the effects of spar placement and plate thickness distribution on the performance of flexible wings. In order to quantify the effects of these parameters on performance, representative sets of planforms with different boundary conditions and thickness distribution are tested. It is important to be able to include the effects of these real wing parameters. These occur due to the physical limitations that are encountered when constructing a real flexible wing. Quantifying these effects allows wing designers to utilize the performance results in developing

real applications.

4.1.3 Data and Results

The primary result of this study is the lift curve of the wing. Given the linearity of the numerical method, the lift curves are very linear and can described in terms of the just the slope. The lift curve slope is calculated from the angle of attack data for the given operating point. Since the wings tested have no camber in their unloaded state, the lift curve passes through the origin and the slope of the lift curve is given by a simple relation between one non-zero lift and the corresponding angle of attack.

For a given planform, lift curve slopes are calculated for a range of stiffness parameters. A performance curve is generated for a given planform to relate the lift curve slope to the stiffness parameter. One particular quantity of interest is the critical stiffness of the wing which is defined as the value of the stiffness parameter that produces a lift curve slope of infinity. The critical stiffness gives a consistent quantity that can be used to relate wings of differing planform and aspect ratio.

The lift curve slope to stiffness parameter relationship is determined for a range of planform aspect ratios. Several parameters are needed to describe in a general way this relationship including the critical stiffness and the slope of the lift curve for a rigid wing for that planform. Once all of these parameters have been determined, the wing's performance can be completely described in terms of the planform, stiffness, and lift curve slope.

4.2 Verification Tests

In order to verify that the numerical algorithm works properly, several verification tests are performed. The first set of tests are convergence tests to show the convergence rate of the algorithm. A second set of verification tests are run to show that the lift curves produced by the method are linear. These test show the characteristics of the numerical method.

The linearity and convergence tests are done for a typical planform for each type

of boundary condition and thickness distribution in order to verify the numerical accuracy of the results for each type of planform. An initial verification test for a simple rectangular flexible wing is presented here to show the methodology of the verification tests and typical results.

4.2.1 Rectangular Planform

In order to verify that the numerical method produces answers that agree with the two-dimensional theory discussed earlier calculations are done for a rectangular wing with an aspect ratio of 10. The aerodynamics and structural response of a high aspect ratio flexible wing should closely approximate the two dimensional theory. This wing is modeled as an isotropic, linearly elastic plate with constant bending stiffness. The wing is simply supported with leading edge pinned and the trailing edge pinned but allowed to displace in the chordwise direction. The chord of the wing is constant from the root to the tip and the leading edge of the wing is perpendicular to the root.

4.2.2 Convergence Tests

In order to show the convergence characteristics of the method, the method is iterated until the solution converges. At each step of the iteration, the average change in the z-displacement is measured. This average displacement is expressed in terms of the Root Mean Square change in the z-displacement of the camberline nodes as given by

$$RMS\ \Delta z_{nodes} = \sqrt{\sum_{N}(z^{n}_{node} - z^{n-1}_{node})^2} \tag{4.1}$$

where z^{n}_{node} is the z location of the camberline node located at the vortex midpoint at iteration n. This $RMS\ \Delta z$ gives a good indication of the average change over the entire wing of the camberline. Thus, a converged solution would have a very small $RMS\ \Delta z$. For these tests, a $RMS\ \Delta z$ on the order of 10^{-7} proved to be a fully converged solution. At this point the accuracy of the method due to the number of significant figures that are stored proves to be the limiting factor in further

convergence. The angle of attack is converged to within .0001 degrees and the induced drag coefficient is converged to within .000001.

The convergence of the method is very fast. The $RMS\ \Delta z$ for the first iteration is on the order of 10^{-2} which represents the initial deflection under the flat plate loading. Since the total magnitude of the load does not change from one iteration to the next, the average deflection does not change significantly either. However, the cambering of the wing has the effect of changing the load shape and thus the shape of the camberline. Thus, the deflection at any location on the wing may change significantly from one iteration to the next as the shape changes. The $RMS\ \Delta z$ takes this into account and measures the average *magnitude* of the deflection change. However, due to the constant magnitude of the loading, even the $RMS\ \Delta z$ decreases very quickly. The convergence rate depends on the stiffness, K, of the wing, but in general, is on the order of an order of magnitude decrease in $RMS\ \Delta z$ per iteration.

To verify that the numerical method works, a rectangular planform with an Aspect Ratio of 10 is tested for several stiffness values. The convergence rate for this wing is shown in Figure 4-1. The convergence is very rapid for all cases, but the stiffer wings converge more rapidly.

The lift coefficient, dynamic pressure, and thus the lift, are held constant through the convergence process. Thus, as the camber changes from one iteration to the next, the angle of attack must change as well to keep the lift constant. The angle of attack converges to its final steady state value very quickly. This convergence is shown in Figure 4-2. The angle of attack for the more flexible wings slightly overshoot their final steady state angle of attack as the wing initially cambers too much due to the flexibility of the material. This is the main cause of the slower convergence rate seen in Figure 4-1.

4.2.3 Linearity of Lift Curve

Due to the linearity of all aspects of the algorithm, the lift curve should be completely linear. The vortex lattice code is completely inviscid so the wing's lift response should be perfectly proportional to the camber and the angle of attack. The finite

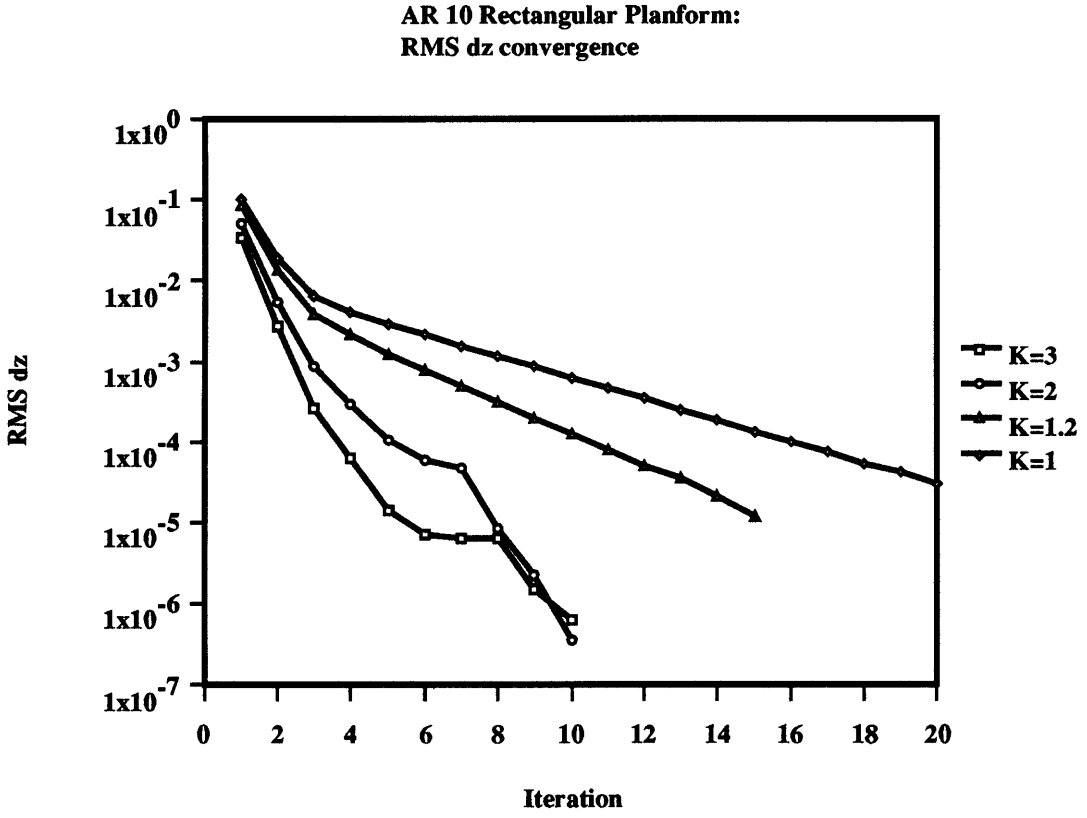

Figure 4-1: Verification Test: Convergence Rate

element code is run in an linearly elastic mode to insure that the deflection is proportional to the load. Thus, the lift curve should be linear.

To confirm this linearity, several lift curves for the rectangular planform are generated over a range of stiffnesses to demonstrate the linearity of the lift curves. The lift curves each have enough data points to ensure good resolution of the statistical linearity of the slope. These lift curves are then analyzed to determine their linearity.

In order to determine the linearity of the lift curves, a statistical characteristic of the data set known as the correlation coefficient as defined in [5] was determined for each of the lift curves. This correlation coefficient expresses the strength of the relationship in the data. A perfectly linear data set has a correlation of 1 or -1 depending on whether the slope of the line is positive or negative. For data that is not perfectly linear, the correlation will be between 1 and -1 with 0 representing a perfectly random data set. The closer the data is to a perfectly linear relationship,

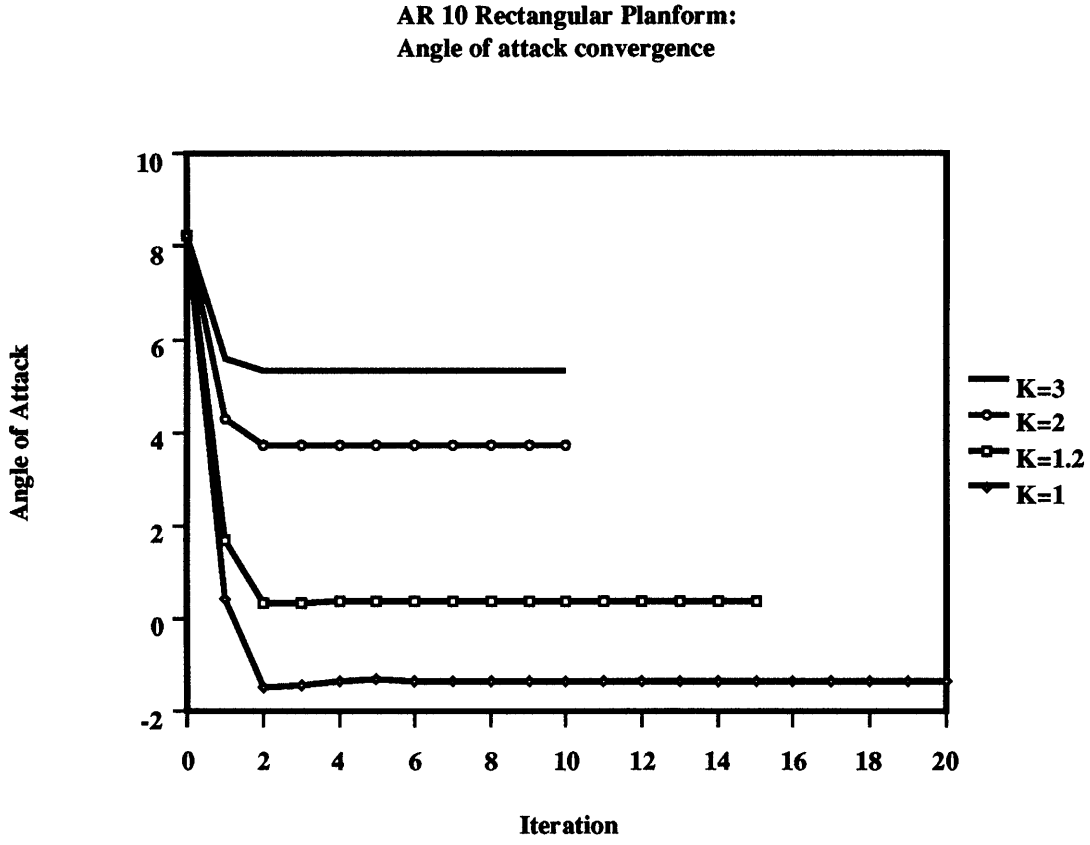

Figure 4-2: Verification Test: Angle of Attack Convergence

the closer the correlation coefficient is to either 1 or -1. The correlation coefficient r is given by

$$r = \frac{\frac{1}{n-1}\sum_{i=1}^{n}(X_i - \bar{X})(Y_i - \bar{Y})}{S_x \times S_y} \tag{4.2}$$

where the data is given by n (X_i, Y_i) pairs, $\bar{X}$ and $\bar{Y}$ are the statistical averages of the X and Y data as given by the equations

$$\bar{X} = \frac{1}{n}\sum_{i=1}^{n} X_i \tag{4.3}$$

and

$$\bar{Y} = \frac{1}{n}\sum_{i=1}^{n} Y_i \tag{4.4}$$

and S_x and S_y are the statistical standard deviation of the data as given by the equations

$$S_x = \sqrt{\frac{\sum_{i=1}^{n}(X_i - \bar{X})^2}{n-1}} \tag{4.5}$$

and

$$S_y = \sqrt{\frac{\sum_{i=1}^{n}(Y_i - \bar{Y})^2}{n-1}} \, . \tag{4.6}$$

The Data that is used for the lift curve is given in (α, C_L) pairs. Since the denominator of the correlation coefficient contains the standard deviation of both variables, the accuracy of the correlation coefficient degrades significantly as the line gets close to vertical or horizontal. In the case of a vertical data set with good linearity for example, the standard deviation of x, S_x is very close to zero as is the $(X_i - \bar{X})$ term in the numerator. Thus, small errors, such as truncation errors cause large changes in the correlation coefficient. A perfect data set for a vertical line would result in a 0 in both the numerator and the denominator.

Table 4.1 gives the correlation coefficients for several lift curves for various stiffnesses of the rectangular planform. These correlations are very close to 1 (-1 for the negatively sloped lift curve) showing the high degree of linearity of the lift curves. Since the lift curves are very linear, they can be expressed in terms of their slope and their intercept. However, all the flexible wings have no camber at $C_L = 0$, and thus the lift curves can be described in terms of their slope alone. Similarly, this slope can be determined by one data point (since the intercept is always zero).

Table 4.1: Correlation Coefficients for Rectangular Planform

K	r
Rigid	0.99999
3	0.99998
2	0.99997
1	-0.99889

4.2.4 Numerical Results

The performance of the flexible wing is described in terms of the lift curve slope. As the value of the stiffness parameter changes, the slope of the lift curves change. This behavior can be quantified and expressed in terms of general performance curves for the wing.

Lift curves are generated for the rectangular wing for several different values of the stiffness parameter over a range of lift coefficients. These lift curves for the wing are shown in Figure 4-3. It is clear from this figure that the lift curves are very linear and that they intercept the origin. This linearity shows the that the method is linear and allows the lift curve to be expressed in terms of the slope and the intercept. This wing (and all of the wings in this study) is uncambered in its unloaded state, so all the lift curves intercept the origin and the lift curves can be expressed in terms of only their slope.

The lift curve slope for the wing increases as the stiffness parameter decreases. The relationship between the lift curve slope and the stiffness parameter is shown in Figure 4-4. This figure only shows the values of the stiffness parameter greater than the critical stiffness of the wing. For stiffness lower than the critical stiffness, the lift curve slopes are negative. These stiffnesses are not shown here mainly because the beneficial operating points are all in the positively sloped region.

The results of the numerical calculations show that for values of the stiffness parameter below the critical stiffness, this relationship follows an inverse proportionality such that the slope, m, is roughly given by

$$m \propto \frac{1}{K}. \tag{4.7}$$

The slope is infinite for the critical stiffness and asymptotically approaches the lift curve slope for the rigid symmetric tapered wing for very high stiffnesses. The relationship can be given by a curve fit to the numerical results of the form

$$m = m_{rigid} + \frac{3.65}{K - K_{crit}}. \tag{4.8}$$

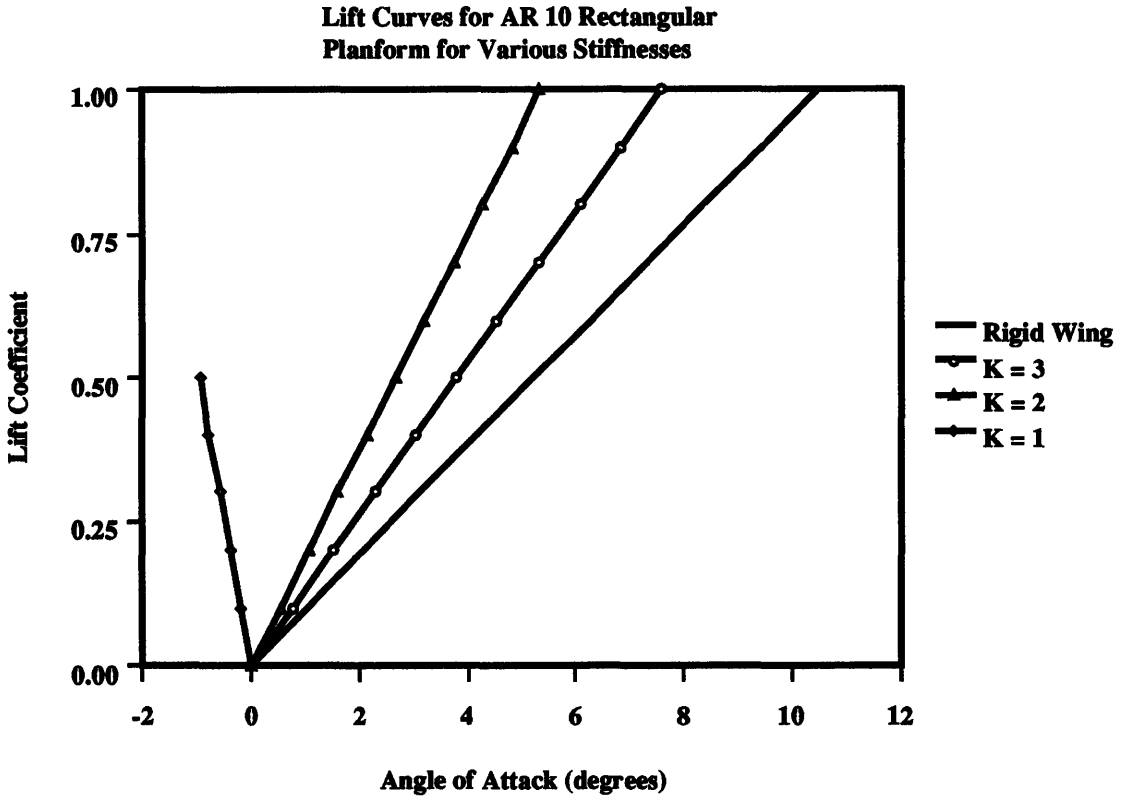

Figure 4-3: Linearity of Lift Curves for Rectangular Planform

where m_{rigid} is the lift curve slope of the rigid wing with the same planform. This relationship is shown by the curve fit shown in Figure 4-4.

The critical stiffness for this wing is given from the numerical analysis to be 1.16. The theory given by Widnall *et. al.* in Equation 2.15 gives the the value of K_{crit} for an elliptically loaded wing of aspect ratio 10 as 1.218. The numerical result is within 5% of the predicted value.

4.2.5 Drag Polar

The induced drag drag of the rectangular flexible wings for a range of stiffness is shown in Figure 4-5. The drag varies very little as the stiffness changes. This is due mainly to the fact that induced drag is primarily a function of the span loading which depends mostly on the aspect ratio and the planform and very little on the camber distribution.

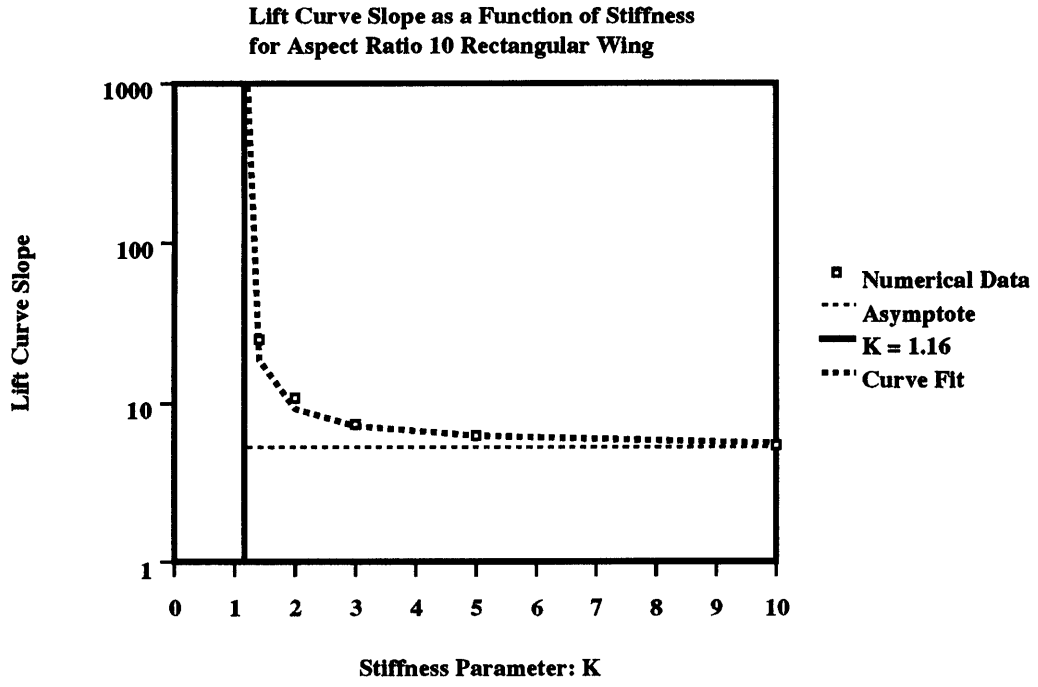

Figure 4-4: Stiffness Effects on Lift Curves Slope for Rectangular Planform

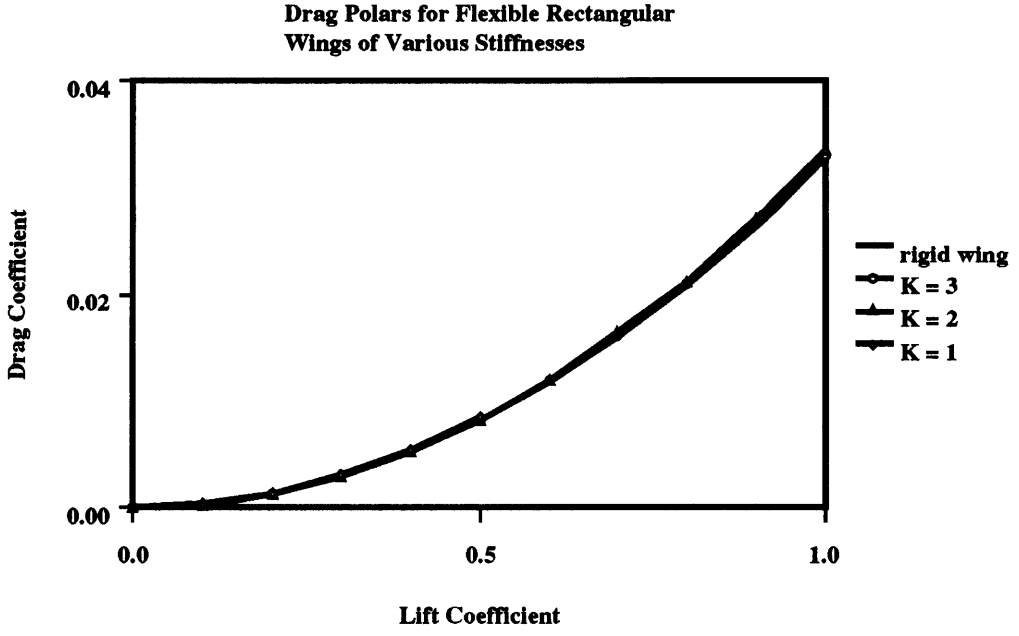

Figure 4-5: Induced Drag Polar for Rectangular Planform

4.3 Analysis of Ideal Tapered Wings

The theory that is discussed in Section 2.4.1 describes the performance of high aspect ratio elliptically loaded flexible wings that are modeled as two-dimensional plates at every point along the span and boundary conditions right at the leading and trailing edge of the wing. This theory should also offer insight into the performance of wings that are nearly elliptically loaded. To verify this theory, a numerical analysis is performed of several tapered flexible wing planforms. The results of this numerical analysis are compared to the elliptic theory to show its accuracy for wings that are not high aspect ratio elliptical wings.

4.3.1 Tapered Wing Planforms

The tapered planforms that are studied here have a very simple geometry. The planform is trapezoidal with the tip chord equal to one half of the root chord. This taper ratio is shown by Glauert [4] to give a close approximation to elliptic span loading. The leading edge is swept back and the trailing edge is swept forward as shown in Figure 4-6. The 70% chord line is perpendicular to the root chord (this is important for comparison to the case where the axis of rotation of the trailing edge spar is placed on this line).

The tapered planforms are used for several reasons. The leading and trailing edges are straight allowing easy enforcement of the leading and trailing edge boundary conditions. In the case where the spar boundary conditions are used, the locations of the spars relative to the local chord is constant along the span of the wing and the spars are straight. The value of the stiffness parameter, when corrected for axle placement is also constant over the span. There is a good amount of prior work on tapered planforms that can be used for comparison.

The lift curve slope for rigid tapered planforms are known from the prior work of Glauert [4]. Thus, it is easy to compare the lift curves for flexible wings to those for rigid wings with the same planform. For the case of rigid wings, the lift curve slope of the tapered wing compared to the elliptic wing is shown for a range of aspect ratios

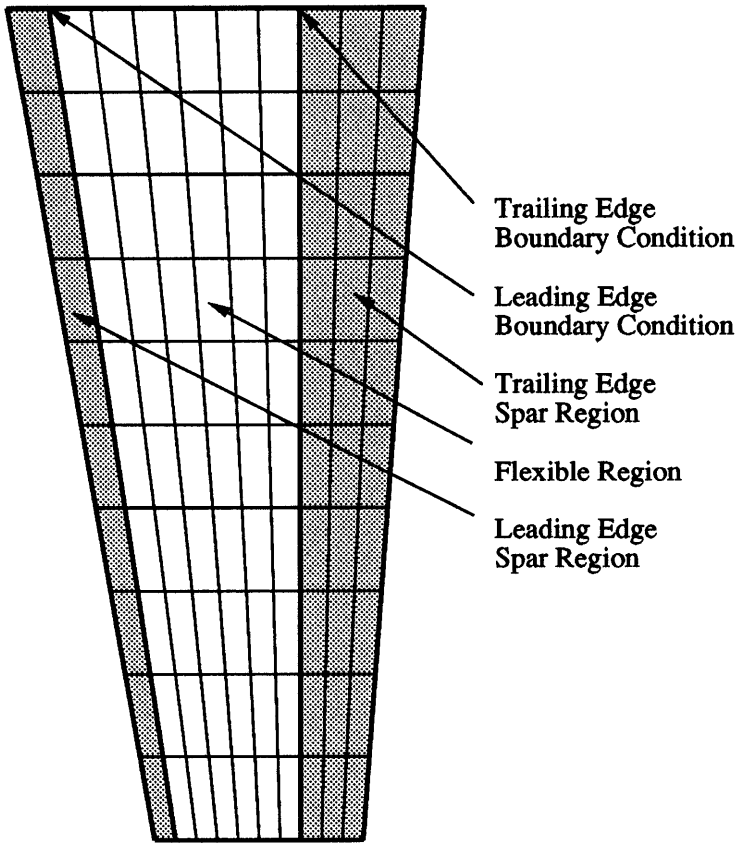

Figure 4-6: Typical Tapered Flexible Wing Model

in Figure 4-7.

The lift curve slope for the family of tapered flexible wings depends on the value of the stiffness parameter of the wing as well as the aspect ratio. For a given aspect ratio the lift curve slope increases as the stiffness decreases until the lift curve becomes completely vertical. The value of the stiffness parameter where this occurs is defined to be the critical stiffness of the wing and depends on the aspect ratio of the wing. For values of the stiffness parameter less than the critical stiffness, the lift curve slope becomes negative.

To determine the effect of aspect ratio on the critical stiffness, K_{crit}, the tapered planforms are modeled without the spar section such that the boundary conditions are enforced at the leading and trailing edges. The plate is modeled as a uniform isotropic linearly elastic material. The plate stiffness in the chordwise direction is constant (constant thickness). The thickness in the spanwise direction is proportional to the

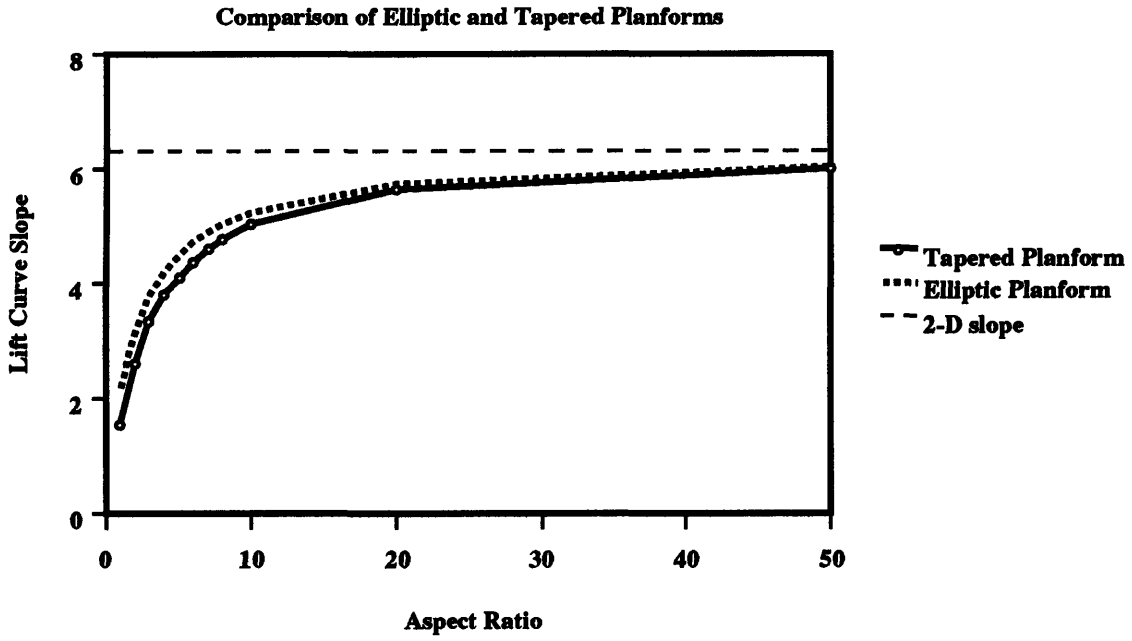

Figure 4-7: Lift Curve Slopes for Tapered Planforms of Various Aspect Ratio

local chord of the wing such that the local value of the stiffness parameter is constant over the span. The leading and trailing edges of the wing are simply supported such that the x and z displacement of the leading edge is constrained and the z displacement of the trailing edge is constrained (the y displacement is also constrained at the root). The root and tip of the wing are free from supports.

A series of such ideally modeled flexible wings with varying aspect ratios are tested to find their critical stiffness, K_{crit}. The theoretical K_{crit} is given by Equation 2.15. This theory was developed for elliptically loaded planforms with no structural interaction between spanwise locations. There should be correction to this theory for non-elliptic distributions and real plates where there is interaction in the spanwise direction. As described in Section 2.4.1, the camber distribution depends to a large degree on the aspect ratio. The bending of the plate at the tip of a low aspect ratio wing will be much more affected by the root bending loads that a high aspect ratio wing.

4.3.2 Numerical Convergence of Tapered Planform

As a check to prove that the numerical model is appropriate for this planform, the convergence rate of the numerical method is checked. As shown in Figure 4-8, the change in the shape of the wing as measured by the average nodal displacement decays very quickly. The shape of the wing converges in well under 20 iterations. Once again the convergence rate depends on the stiffness of the wing, but even for wings with a stiffness less than the critical stiffness, the convergence is good.

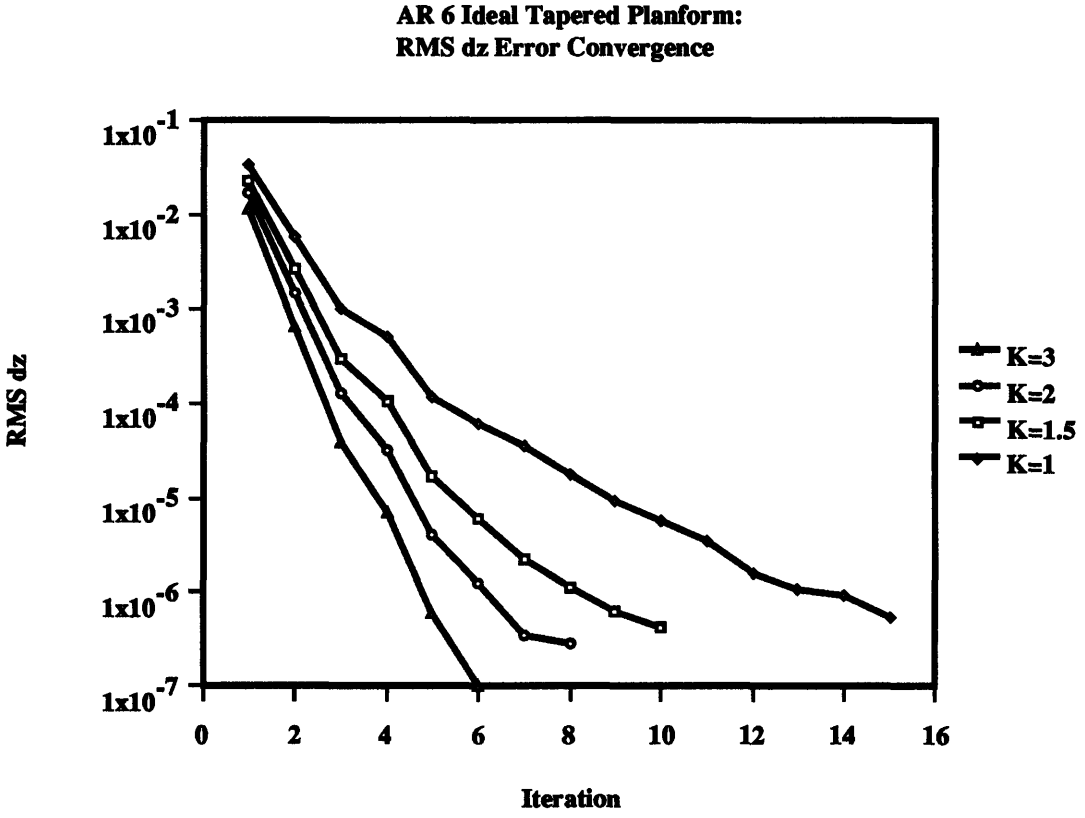

Figure 4-8: Convergence Rate for Tapered Planform

As the nodal displacements converge to a final steady state shape, the angle of attack of the wing also converges. Once again, the angle of attack of the wing converges to within 0.0001 degrees for a RMS error an the order of 10^{-6} to 10^{-7}. The convergence of the angle of attack is shown in Figure 4-9.

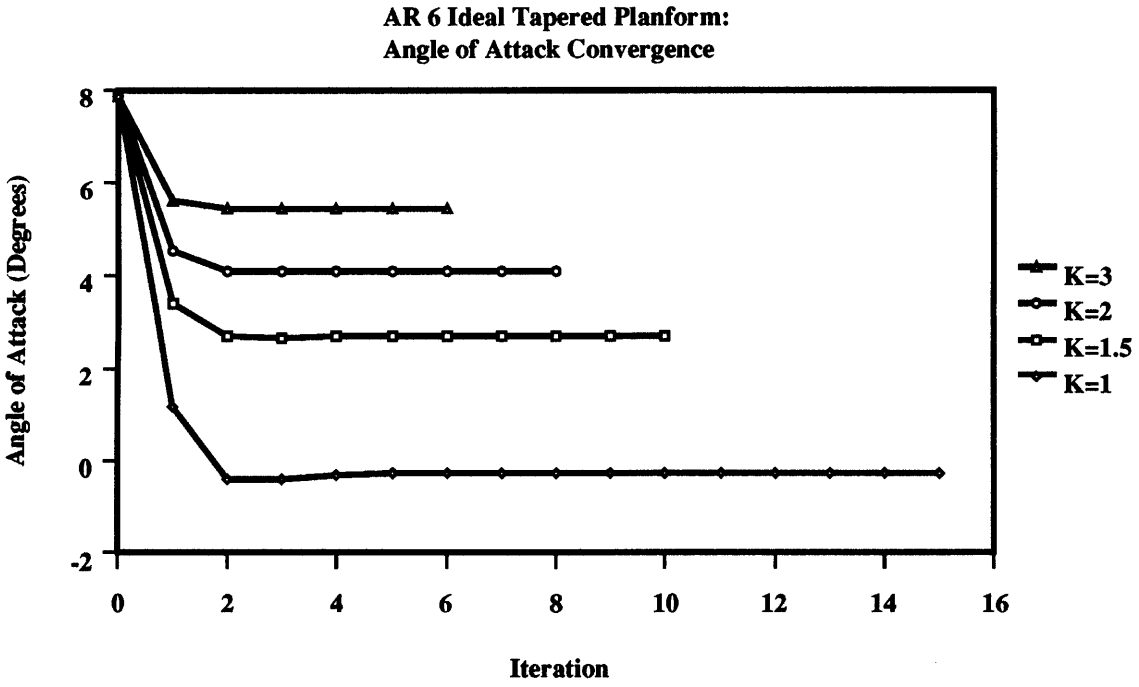

Figure 4-9: Convergence Rate for Tapered Planform

4.3.3 Linearity of Lift Curve

The lift curves for a flexible tapered wing of aspect ratio 6 over a range of flexibilities are shown in Figure 4-10. Using the statistical analysis described in Section 4.2.3, the linearity of each curve can be determined. The very high correlation coefficients shown in Table 4.2 show that the lift curves generated by the numerical method are very linear for the tapered planforms. Thus a lift curve can be described simply by its slope which is determined by a single non-zero lift data point (since the lift curves all go through the origin).

Table 4.2: Correlation Coefficients for Tapered Planform

K	r
Rigid	0.99996
3	0.99990
1.5	0.99990
0.75	-0.99893

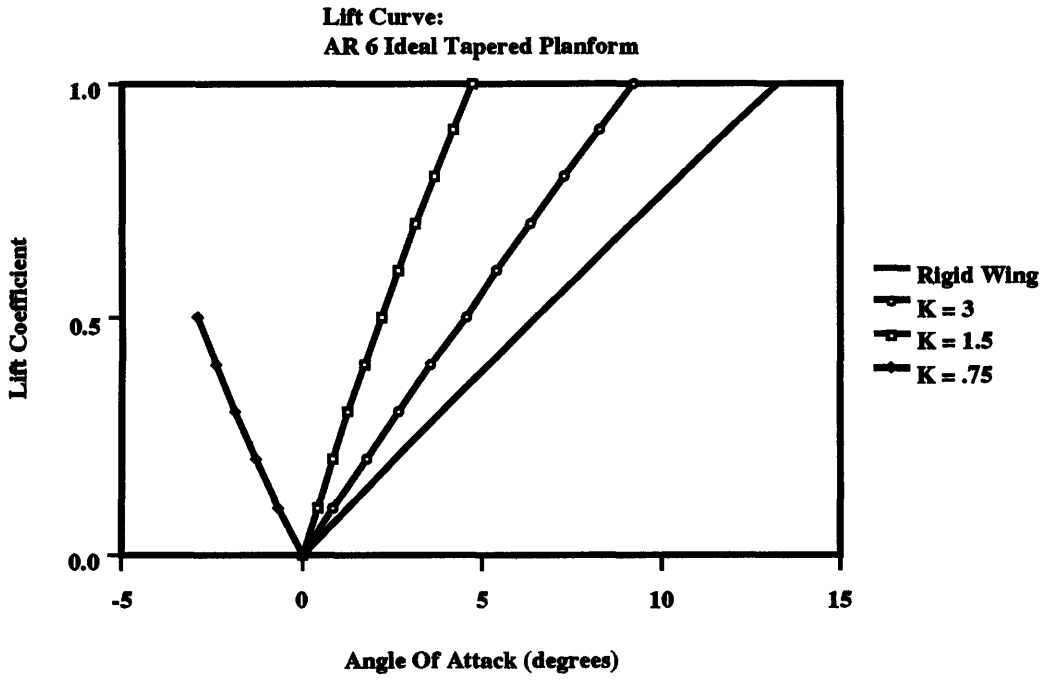

Figure 4-10: Linearity of Lift Curves for Tapered Planform

4.3.4 Induced Drag Polars

The drag polars for several stiffnesses of the aspect ratio 6 flexible tapered wings are shown in Figure 4-11. The change in stiffness has a minimal effect on the induced drag of the wing as can be seen by the similarity among all the curves.

Camber primarily affects the pressure distribution in the chordwise direction. Since this pressure distribution is the main factor in influencing the boundary layer, the camber distribution can have large effects on the viscous drag. This drag often makes a significant contribution to the overall drag on the wing and proper camber can dramatically improve the viscous and overall drag. However, the computer programs used in this study do not predict the viscous drag on the wing.

4.3.5 Stiffness Effect on Lift Curve Slope

As the stiffness of the wing changes, the amount of camber for a given lift point and thus the lift curve slope changes. For very high stiffness when the wing is essentially rigid, there is little cambering and the lift curve nearly matches that of a rigid wing of

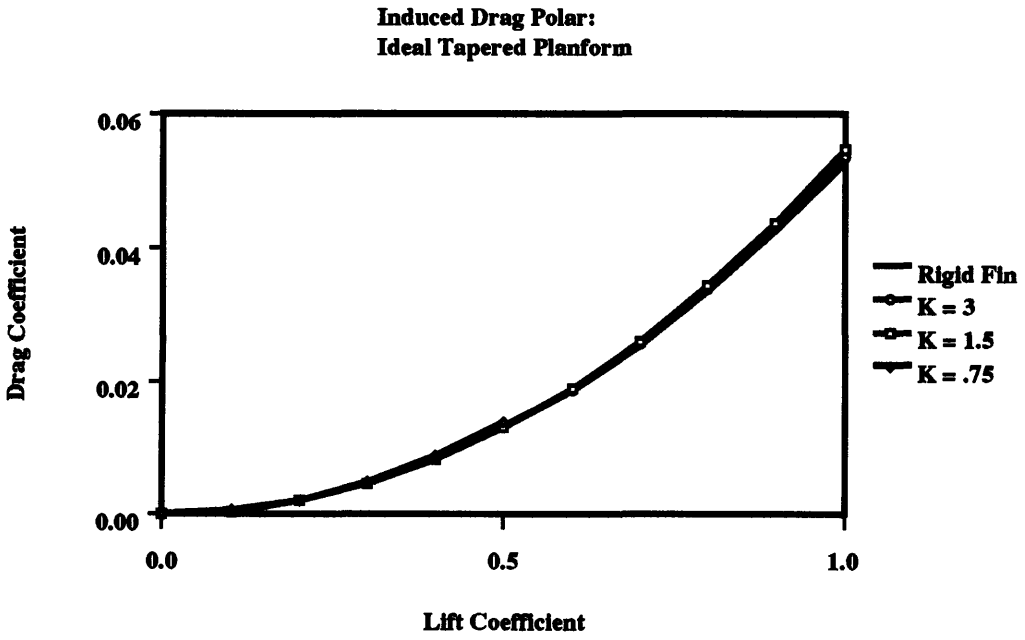

Figure 4-11: Similarity of Drag Polars for Tapered Planform

identical planform. As the stiffness decreases, the slope increases until the lift curve eventually becomes vertical and then negative as seen in Figure 2-3. The critical stiffness, K_{crit}, of the wing is defined as the point at which the lift curve slope of the wing becomes completely vertical. Figure 4-12 shows the relationship of the lift curve slope to the stiffness, K for the ideally constrained tapered wing planform of Aspect Ratio 5.

As with the rectangular planform, the relationship of lift curve slope to stiffness for the tapered planform follows an inverse proportional relationship such that

$$m \propto \frac{1}{K}. \tag{4.9}$$

The slope is again infinite for the critical stiffness and asymptotically approaches the lift curve slope for the rigid symmetric tapered wing for very high stiffnesses. Thus the relationship can be given by a curve fit similar to Equation 4.8 of the form

$$m = m_{rigid} + \frac{F}{K - K_{crit}}. \tag{4.10}$$

where m_{rigid} is the lift curve slope of a rigid wing and F is a proportionality coefficient

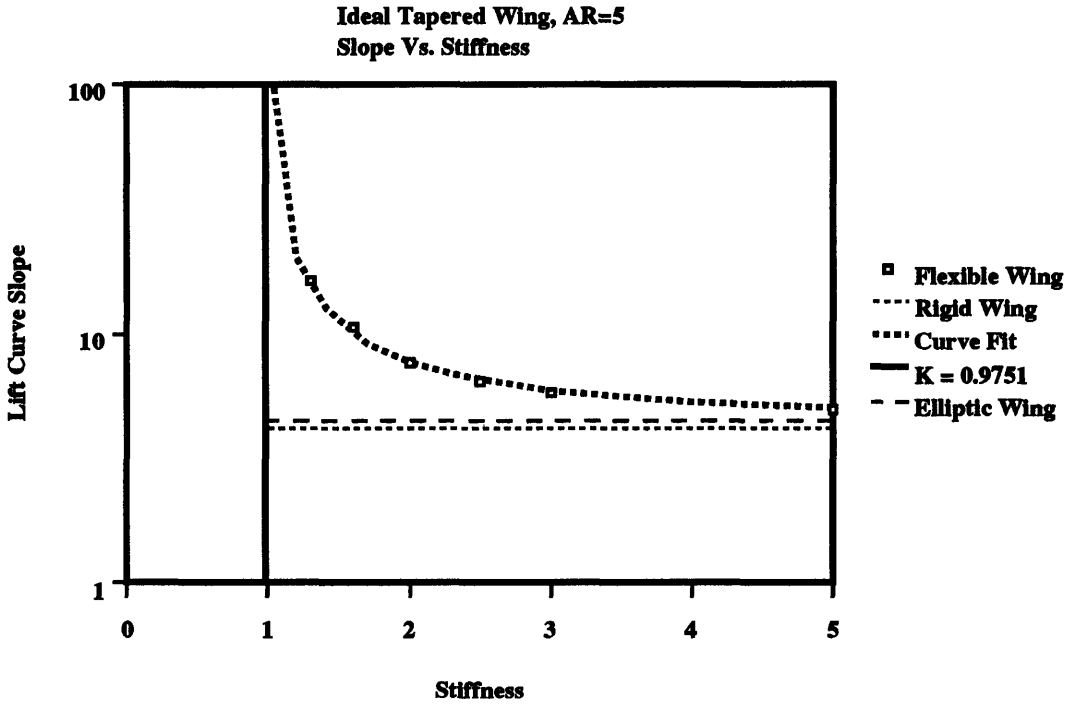

Figure 4-12: Lift Curve Slope as a Function of Stiffness

that depends on the aspect ratio of the wing. This inverse proportionality relationship fits the data extremely well as shown by the curve fit data in Figure 4-12.

4.3.6 Aspect Ratio Effect on Flexible Wings

The value of the critical stiffness depends on the aspect ratio of the wing. As the wing aspect ratio goes down, the critical stiffness, K_{crit}, decreases. A relationship is given by Widnall *et. al.* in [10] that relates K_{crit} to the aspect ratio of the wing. This relationship is based on lifting line theory and given in Equation 2.15 where the airfoil $K_{crit} = 1.4$. This relationship is shown by the theoretical line in Figure 4-13.

The performance shown by the numerical analysis matches the lifting line performance prediction curve fairly well. For high aspect ratios, the numerical performance of the flexible wing shows the same asymptotic behavior of the critical stiffness as the lifting line theory predicts. For lower aspect ratios, the lift curve slope decreases. For extremely low aspect ratios, the camber has very little affect on the lift of the wing and thus the lift curve slope is not affected by the stiffness of the wing. For aspect

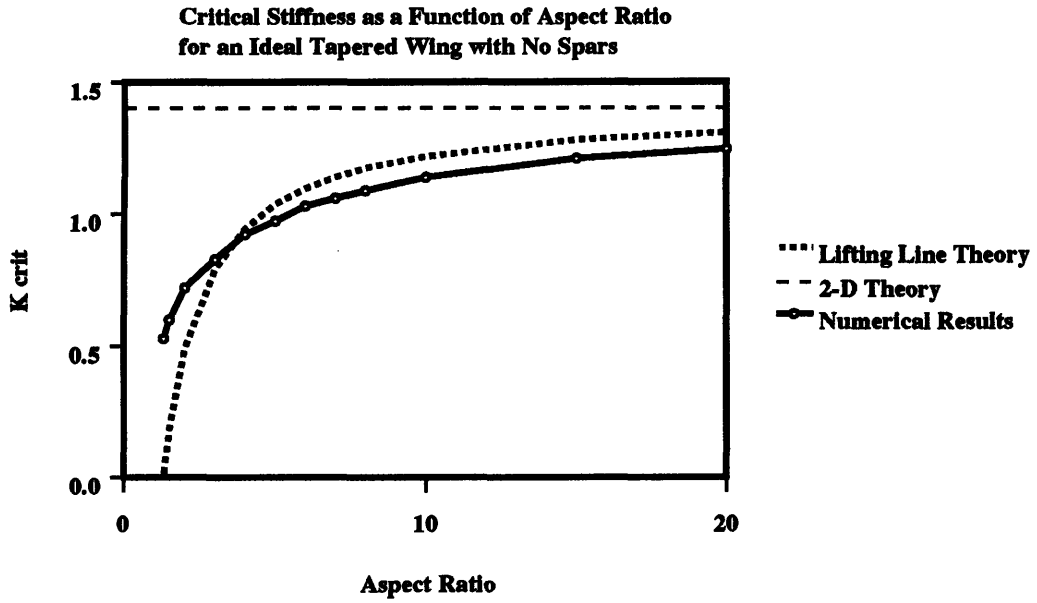

Figure 4-13: Aspect Ratio Effects on Critical Stiffness

ratios below about 1.2, the numerical method would not converge.

The numerical results show a lower critical stiffness for most aspect ratios than the lifting line theory predicts. This lower K_{crit} is mainly attributable to the difference in the way the structure is modeled between the lifting line calculations and the numerical analysis done here. In the lifting line calculations, the camber at any span station responds only to the local loading and there is no structural stiffness in the spanwise direction. In the numerical model used here, the structure is modeled as a real plate such that there is significant interaction in the spanwise direction. This has a tendency to decrease the camber at the root and increase it near the tip as compared with the lifting line theory.

In the low aspect ratio range, the critical stiffness calculated from the numerical method is greater than that from the lifting line theory. For low aspect ratios the swept leading edge boundary condition acts to change the bending behavior of the plate. At higher aspect ratios, the bending is nearly cylindrical where for low aspect ratios the bending is more conic. This effect causes the structure to actually camber

more than the lifting line theory predicts near the root and increases the critical stiffness.

The proportionality coefficient, F, for an ideal tapered wing is also affected by aspect ratio as shown in Figure 4-14. The curve fit shown in this figure is given as

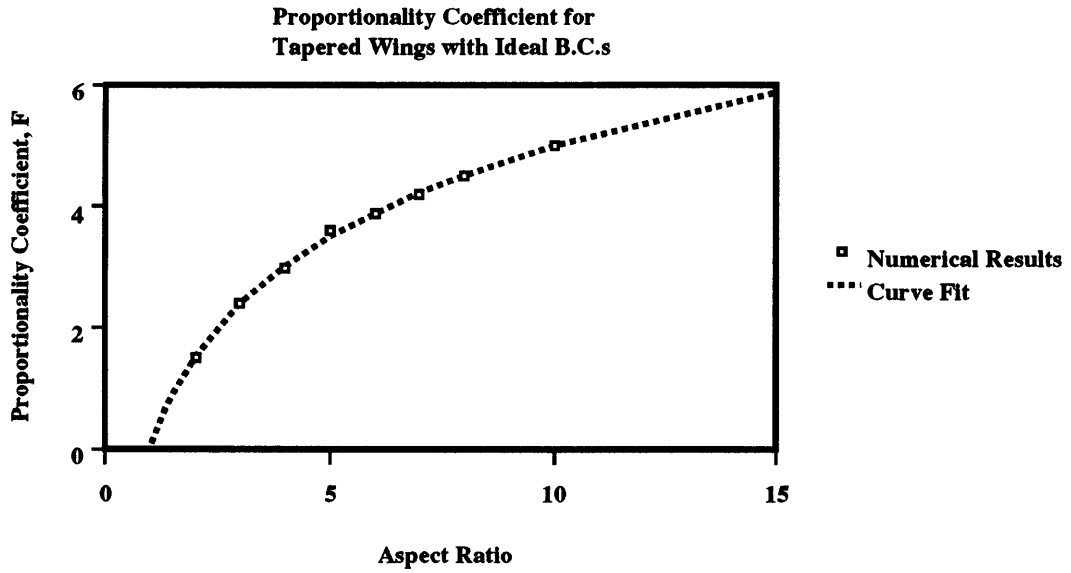

Figure 4-14: Proportionality Coefficient for ideal Tapered Planform

$$F = 5 \log AR + 0.05 \,. \tag{4.11}$$

The lift curve slope of a flexible wing can be determined from Equation 4.10. From the planform alone, the slope of the rigid wing, m_{rigid}, can be determined. K_{crit} depends on several factors including aspect ratio, span loading and spar placement. This equation can be used to determine the lift curve slope for flexible wings with stiffnesses greater than K_{crit}. It has been found from prior work that most of the useful operation of flexible wings occurs above the critical stiffness.

4.3.7 Lift Performance Of Ideal Tapered Wings

The lift coefficient of tapered wings with boundary conditions enforced along the leading and trailing edges can be expressed as a function of the angle of attack as

$$C_L = \left(\frac{2\pi}{1 + \frac{2}{AR}} + \frac{5 \log AR + 0.05}{K - 1.4(1 - \frac{1.3}{AR})}\right)\alpha \tag{4.12}$$

This equation gives the lift coefficient for a wing of given aspect ratio and stiffness.

The comparison of the critical stiffness for the wing with the effective stiffness for the aspect ratio 5 flexible wing is shown in Appendix A. The comparison to the stiffness test gives a value for the constant, A. For this wing, $A = 0.115$ (Widnall gives the range of A as $0.9 < A < 0.12$ in [10]).

The two-dimensional case for these boundary conditions gives $A = 0.103$ which is well within the range given by Widnall and very close to $A = 0.1$ that she gives as the most likely value for A.

4.4 Analysis of Non-Ideal Tapered Wings

The performance of real wings does not match the ideal performance models that are characterized in Section 4.3. Two of the major effects on the performance are caused by the placement of spars and the non-uniform chordwise thickness distribution of real flexible wings. Real wings cannot be supported by the idealized boundary conditions of the ideal wings. The thickness of real wings varies along the chord changing the plate stiffness over the chord. By modifying the models, the effects of these real wing non-idealities on the wings' performance can be determined.

4.4.1 Spar Boundary Conditions

The idealized supports at the leading and trailing edges that constrain the wings in the previous section cannot be easily realized for real wings due to the thickness constraints. All real wings must have spars that are placed where the airfoil is thicker. The leading edge spar is placed aft of the leading edge in the wing but must be forward

of the 25% chord location in order to allow the wing to camber properly. The trailing edge spar is placed forward of the trailing edge but must be aft of the 60% chord location for proper bending. Design tradeoffs for real wings have shown that placing the spars at the 10% and 70% chord stations gives a reasonable compromise between the bending behavior and the spar strength.

The spars of each of the wings are modeled as a relatively high modulus isotropic region of the wing. The spars are designed for very minimal deflection under the lifting loads by having a modulus that is 7 or 8 orders of magnitude greater than that of the flexible region. The spar is cantilevered at the root and allowed to rotate such that the axis of rotation forms a boundary condition for the flexible region. The spar regions of the wing extends from the axis of rotation to the leading and trailing edges such that only the region between the spar axes of rotation is allowed to bend substantially under the loading.

Real wings need to support a substantial spanwise bending loads due to the lift. This load is supported by the spars or their structural equivalent. The cross-sectional moment of inertia of the spars is, in general, rather large so as to react the bending moments. Thus, they are usually placed in the thickest region of the airfoil. For flexible wings, the spars must be near the leading and trailing edges of the airfoil so as to provided the proper boundary conditions for the flexible region. Airfoils are invariably thin near the leading and trailing edges, so the spars need to be rather large in size to make up for the lack of bending moment of inertia of their cross-sections. The trailing edge spar, in particular, must be as far forward as possible to take advantage of the thicker part of the airfoil.

In order to closely model a real wing, the spars in the model have been made rather large and are placed as close to the center of the airfoil as possible. The trailing edge spar region makes up the first 10% of the chord of the wing. This location is far enough from the leading edge as to allow a sizable spar thickness, while still far enough forward to allow proper bending of the flexible region. The trailing edge spar makes up the last 30% of the wing at the root and a similar percentage over the span of the wing. Again, this location allows the spar thickness to be large yet still allows

the flexible region to bend. The wing is made rigid in front of the leading edge axle and behind the trailing edge axle to keep these regions from deforming under load. This is particularly important for the trailing edge so as to provide a solid trailing edge that enforces the Kutta condition. These two regions are shown in Figure 4-21

These realizable spar locations dramatically effect the stiffness of the wing. This effect comes from several factors. First, the bending region of the plate is shorter in length effectively increasing its stiffness. Second, the loading between the axles is less than the total load (some of the load acts in front of the leading edge spar or behind the trailing edge spar) thus reducing the bending loads on the plate. Finally, the load that acts in front of the leading edge spar and behind the trailing edge spar act to "uncamber" the wing due to the adverse moments they apply. All of theses factors combine to make the plate appear much stiffer than the stiffness parameter indicates.

This effect decreases the value of K_{crit} for a given planform. Using the spar location correction formula from Widnall *et. al.* [10],

$$K_{crit} = 1.3 - 2.6\frac{x_{L.E.\ Spar}}{c} - 2.3(1 - \frac{x_{T.E.\ Spar}}{c}) \tag{4.13}$$

the critical stiffness for an airfoil section with the spars at the 10% and 70% locations is reduced from 1.4 to 0.35. For an elliptically loaded wing with an aspect ratio of 8, the finite span correction formula

$$K_{crit\ wing} = K_{crit\ airfoil}\ (1 - \frac{1.3}{AR}) \tag{4.14}$$

further reduces K_{crit} from 0.35 to 0.293. The interaction of the various spanwise locations of the bending plate reduce K_{crit} further. The numerical analysis for this tapered wing with an Aspect Ratio of 8 and spars at the 10% and 70% locations gives $K_{crit} = 0.255$.

The lift curve slope for this wing as a function of its stiffness is shown in Figure 4-15. This Figure shows how the lift curve slope increases as the stiffness decreases. As the stiffness decreases, the lift curve slope goes up as more of the lift is generated by camber and less by angle of attack. The slope becomes infinite for the case where all

the lift comes from camber and none from angle of attack. The stiffness where this occurs is defined to be the critical stiffness of the wing, K_{crit}.

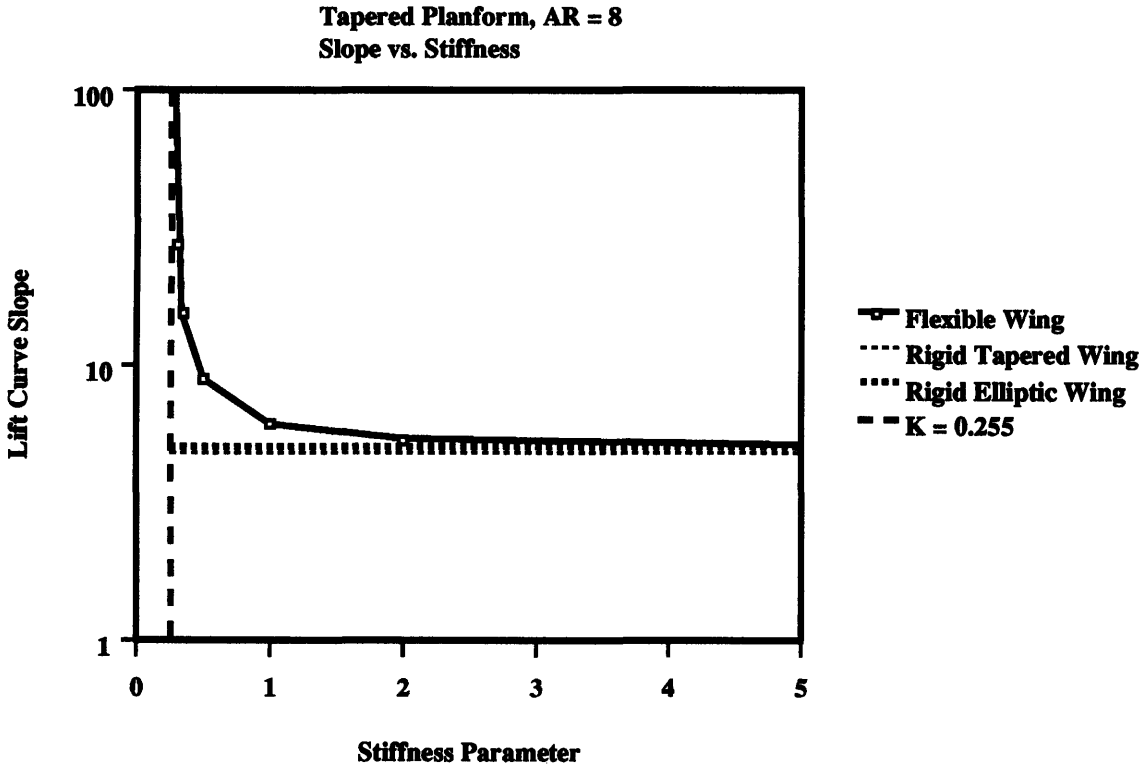

Figure 4-15: Stiffness Parameter Affect on Lift Curve Slope

The relationship between lift curve slope and stiffness follows a similar inverse relationship as the ideal case. The proportionality coefficient for the tapered planform with the spar boundary conditions is shown in Figure 4-16. The curve fit that is shown in that figure gives the functional form for F for this case of a tapered wing with spars at the 10% and 70% chord positions. This curve fit is given by

$$F(AR) = \log AR + 0.05 \,. \tag{4.15}$$

Correcting for aspect ratio follows Equation 2.15, but uses the two-dimensional airfoil $K_{crit} = 0.35$. Thus the curve is similar to the curve for the ideal boundary conditions, but proportionally lower. This curve along with the numerical data are presented in Figure 4-17.

The critical stiffness for the wing displays a similar comparison to the lifting line

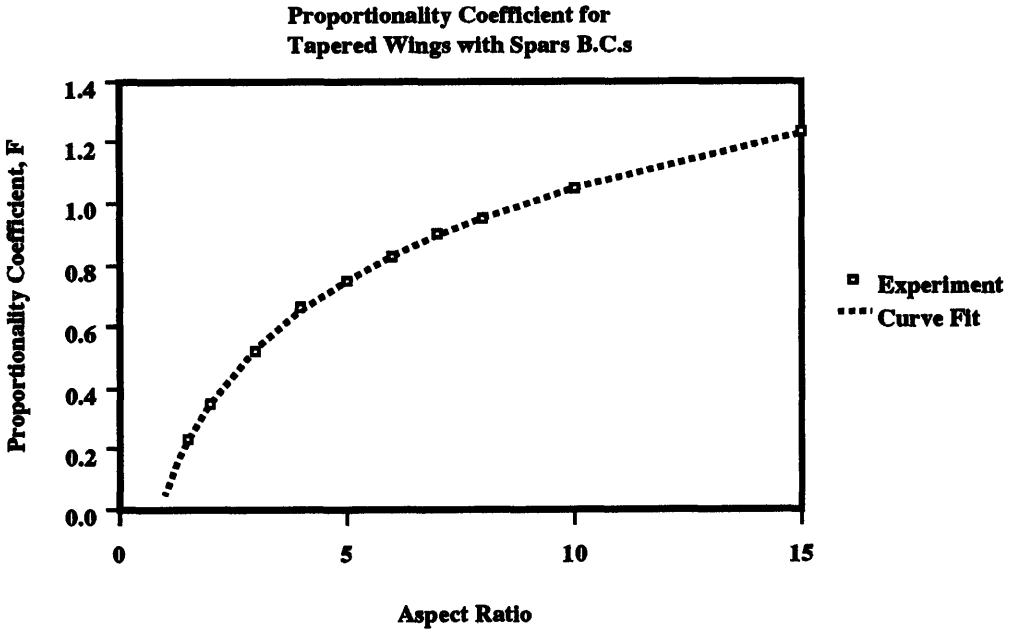

Figure 4-16: Aspect Ratio effect on F

prediction as the ideal tapered wing. The critical stiffness falls below the lifting line prediction at high aspect ratios and for very low aspect ratios are higher than predicted. However, the vales are close to the lifting line prediction. Thus, a performance curve that utilizes the lifting line prediction gives a good estimate of the critical stiffness for the wing.

The lift coefficient of tapered wings with spars at the 10% and 70% chord locations, uniform plate stiffness in the chordwise direction and constant stiffness in the spanwise direction can be expressed as a function of the angle of attack as

$$C_L = \left(\frac{2\pi}{1 + \frac{2}{AR}} + \frac{\log AR + 0.05}{K - 0.35(1 - \frac{1.3}{AR})}\right)\alpha \tag{4.16}$$

The comparison of the critical stiffness for the wing with the effective stiffness for the aspect ratio 5 flexible wing is shown in Appendix A. The comparison to the stiffness test gives a value for the constant, A. For this wing, $A = 0.122$ which is slightly higher than predicted by Widnall *et. al.* in [10]. The two-dimensional case for these boundary conditions gives $A = 0.104$ which is well within the range given by Widnall and very close to $A = 0.1$ that she gives as the most likely value for A.

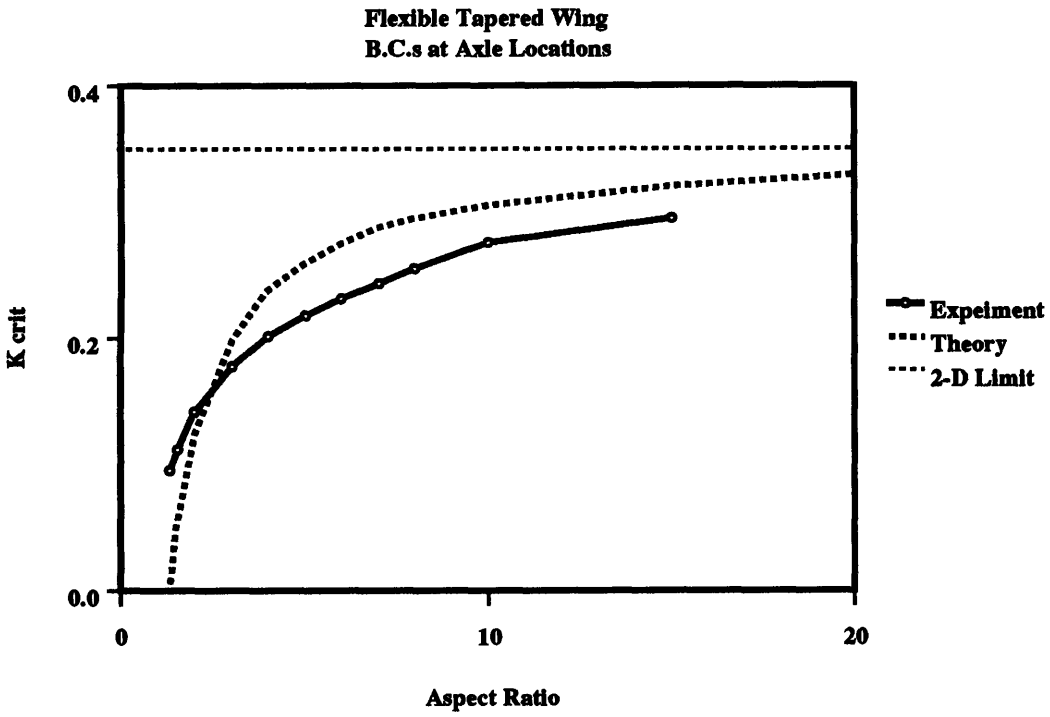

Figure 4-17: Aspect Ratio Effects on Critical Stiffness for Wing with Spars

4.4.2 Non-Uniform Plate Stiffness

A further correction to the theory involves the non-uniformities in the plate stiffness due to the thickness distribution of the airfoil sections. The wings considered in the previous sections are modeled as having a uniform plate distribution in the chordwise direction in the flexible region of the wing. If a constant isotropic material is used however, the plate stiffness will vary in the chordwise direction as the thickness varies. This should affect the behavior of the wing slightly.

The plate stiffness, D, for an isotropic plate is given by

$$D \equiv \frac{E\, h^3}{12(1 - \nu^2)} \tag{4.17}$$

where E is the modulus of the plate, ν is Poisson's ratio and h is the thickness of the plate. For a NACA 4 digit series airfoil with 15% max thickness (such as a NACA 0015), the thickness distribution is given in [1] as

$$h(x) = 1.5(0.2969\sqrt{\frac{x}{c}} - 0.126\frac{x}{c} - 0.3516(\frac{x}{c})^2 + 0.2843(\frac{x}{c})^3 - 0.1015(\frac{x}{c})^4) \; . \quad (4.18)$$

Since the only significant plate bending occurs in the flexible region between the spars, the average thickness in this region can be determined by taking the integral of the thickness over this flexible region and dividing by the length of the flexible region,

$$h_{ave} = \frac{1}{0.6c} \int_{\frac{x}{c}=0.1}^{0.7} h(x)dx \quad (4.19)$$

giving an average thickness of $h_{ave} = 0.132467$. The average plate stiffness, D for this airfoil section is then defined using the average thickness as

$$D_{ave} = \frac{E\, h_{ave}^3}{12\,(1-\nu^2)} \quad (4.20)$$

giving finally a stiffness for the airfoil section as

$$K = \frac{D_{ave}}{q_\infty \frac{c}{2}^3} \; . \quad (4.21)$$

where D_{ave} is the local plate stiffness and c is the local chord of the wing.

For airfoils with this stiffness distribution, The K_{crit} correction for axle placement has not been determined in any of the prior work. However, the correction can be determined from the effective stiffness test. The results of the two-dimensional effective stiffness test for spars placed at the 10% and 70% chord locations, as shown in Appendix A, give an estimate for the airfoil $K_{crit} = 0.30$. Figure 4-18 shows the effect of non-uniform thickness on the lift curve slope to stiffness relationship.

The lift curve slope for the NACA thickness wing is slightly lower that of the uniform thickness wing of the same aspect ratio as shown in Figure 4-18. The lift curve slope again follows the inverse proportionality relationship to the stiffness parameter.

The value of K_{crit} for the wing of finite span again depends on the aspect ratio of the wing. The comparison of K_{crit} for wings of several planforms with both uniform and NACA thicknesses are shown in Figure 4-19. For this definition of the average

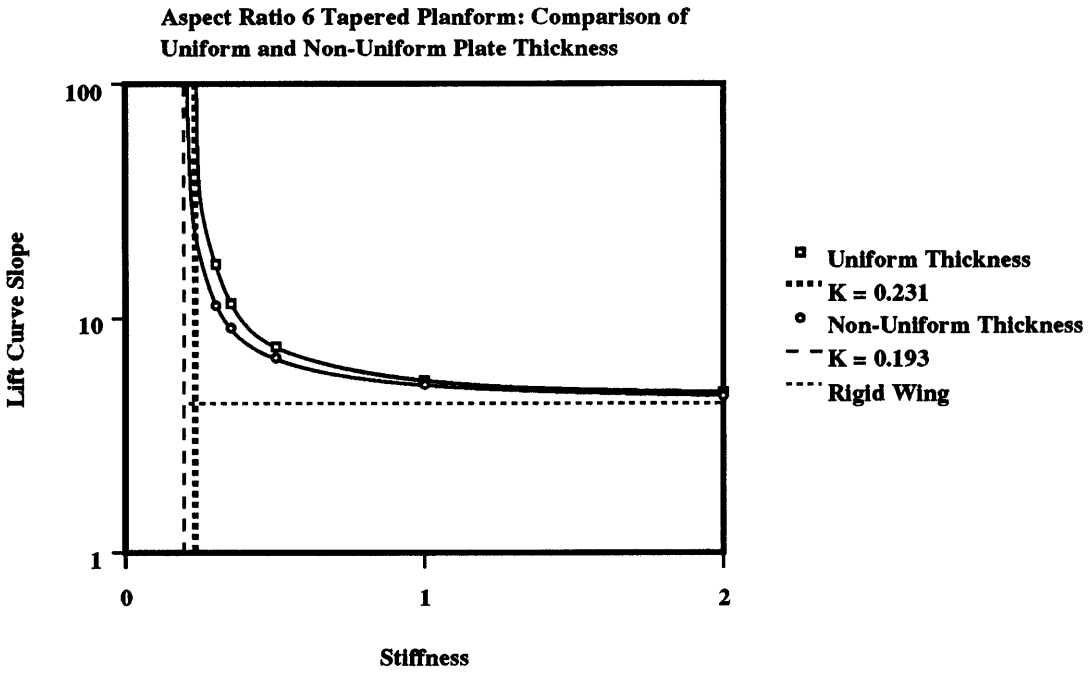

Figure 4-18: Comparison of Uniform and Non-Uniform Thickness Wings

plate stiffness, the critical stiffnesses for the NACA thickness wings are below those of the uniform thickness wings.

There is also a correction to F based on the non-uniform plate thickness distribution. For the aspect ratio 6 wings shown in Figure 4-18, the proportionality coefficient, F, is decreased from 0.825 to 0.725 for the non-uniform thickness distribution. The Proportionality Coefficient is affected in a similar way for wings of other aspect ratios. A comparison of The proportionality coefficients for a uniform thickness and a NACA 0015 thickness distribution are shown in Figure 4-20. For the wing with the non-uniform thickness distribution, F is given from the curve fit as

$$F(AR) = 0.868 \log AR + 0.05 \, . \tag{4.22}$$

Thus, the lift coefficient for the flexible wing with NACA thickness distribution is given by

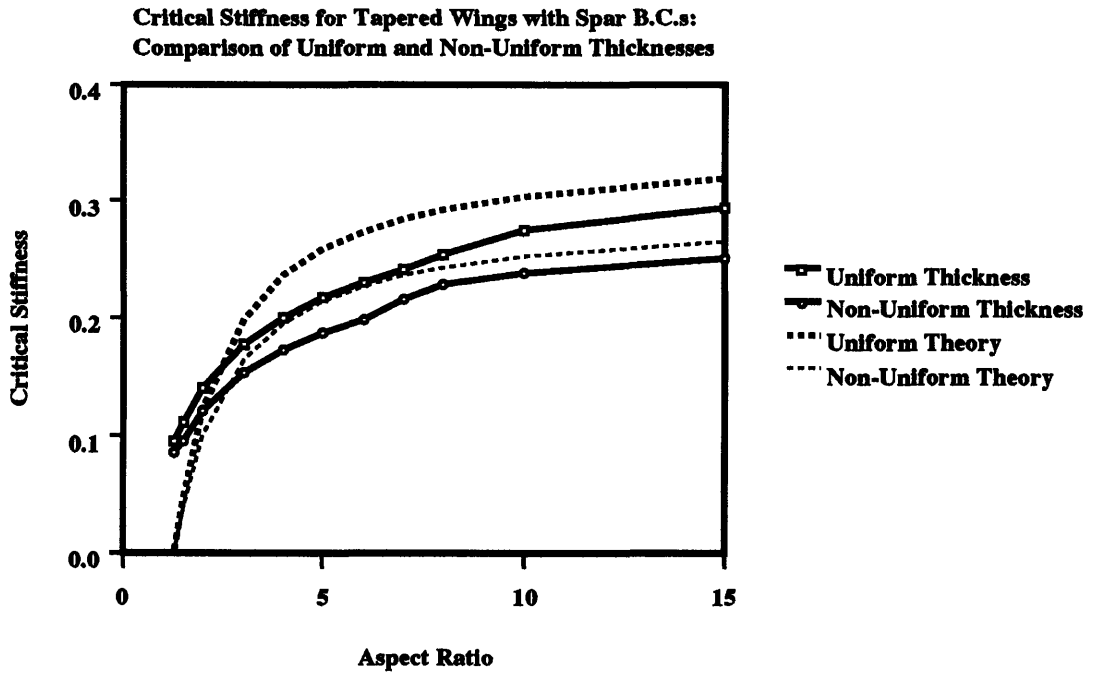

Figure 4-19: Effect of Non-Uniform Thickness on Critical Stiffness

$$C_L = \left(\frac{2\pi}{1 + \frac{2}{AR}} + \frac{0.0868 \log AR + 0.05}{K - 0.30(1 - \frac{1.3}{AR})}\right)\alpha \tag{4.23}$$

in terms of the aspect ratio and the stiffness parameter of the wing.

subsectionEffective Stiffness Comparison

An effective stiffness test for a tapered wing with an aspect ratio of 5 and the NACA chordwise thickness distribution is shown in Appendix A. Comparing the effective stiffness to the numerically calculated critical stiffness gives a value for $A = 0.20$. This value of A is higher than the A value for the uniform thickness wings. However, the similar comparison for the two-dimensional airfoil case gave a value for $A = 0.16$ indicating that the average plate stiffness for the airfoil may not adequately model the plate stiffness and would therefore change the stiffness parameter and the critical stiffness.

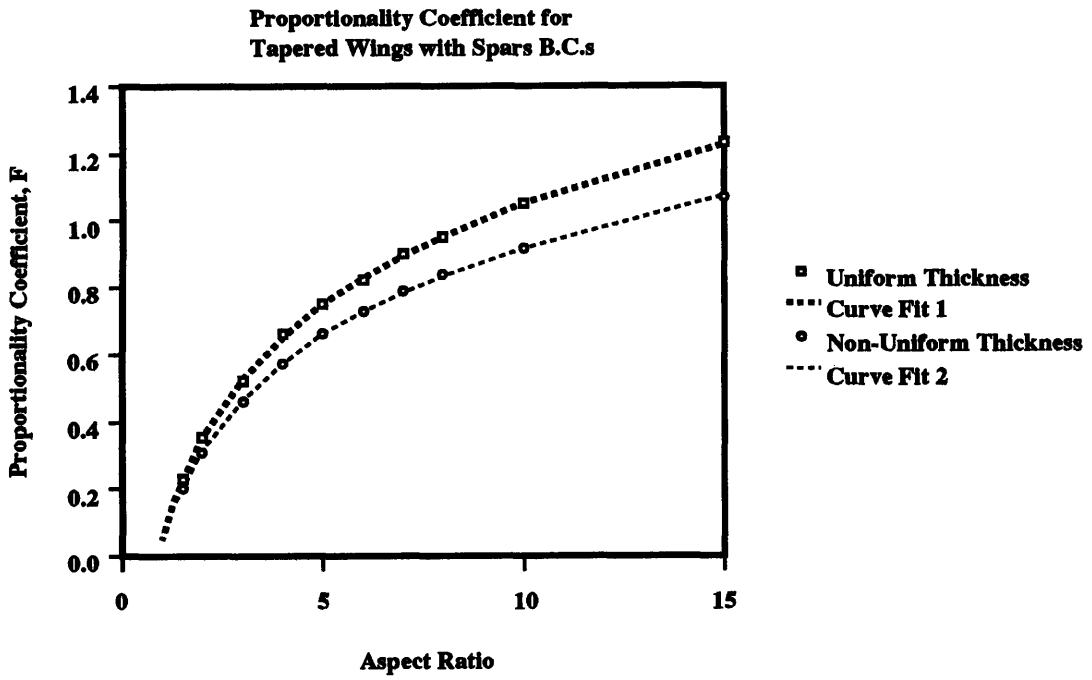

Figure 4-20: Effect of Non-Uniform Thickness on Proportionality Coefficient, F

4.5 Tests Involving Sailboard Fin Planforms

Several flexible wing planforms have been developed for sailboard fins. These fins were developed by Flex Foil Technology Incorporated and are referred to as the Flex Foil planforms. The analysis of these planforms demonstrates the performance of real wings. These wings were designed to more closely approximate elliptic loading than the tapered planforms. The numerical models tested here closely model actual sailboard fins that have been constructed and sailed.

4.5.1 Sailboard Fin Planforms

One application of flexible wings is in flexible sailboard fins. Several prototypes of such fins have been developed. These fins present difficult mechanical engineering problems for their designers. The fins are small yet generate a significant load making strength of the spars critical. The attachment to the windsurfer itself is also difficult given the available space inside the board. The fins are much smaller than traditional

windsurfer fins so that they can take advantage of the higher lift coefficients possible for cambered wings.

The latest prototype fin utilizes carbon fibers in the leading and trailing edge spars to solve the strength problem. Uni-directional fibers are molded into the leading and trailing edge regions to provide bending strength. These fibers are tapered into cylindrical axles at the root which are inserted into holes in the board. These cylindrical axles are allowed to rotate providing the proper boundary conditions for the fin. The hole for the trailing edge axle is elongated to allow it to slide. These same axles react the bending loads on the cantilevered wing due to the lift.

The flexible region between the spars is composed of solid polyurethane rubber. The modulus of this rubber is carefully controlled to provided the proper stiffness for the fins allowing them to camber under the lift loads that they generate. This rubber is molded directly onto the axles providing for a good mechanical joint.

These planforms reflect the design compromises that these real constraints impose upon flexible wings. The spars are placed at the 10% and 70% chord locations of the root rather than at the leading and trailing edges of the wing. The leading edge is straight rather than curved and swept at the root. They also have limited aspect ratios that reflect the need to react the lift loads by cantilevered supports at the root.

The geometry that is assumed for the wings takes into account the mechanical aspects of the camber deformation. The leading edge of the wing is swept back at a small angle but is straight so that the spar can rotate without deforming the wing out of the x-y plane. The trailing edge spar has a straight leading edge along the axis of rotation. The trailing edge is curved such that the planform takes on a nearly elliptical chord distribution. The model is shown in Figure 4-21.

The aerodynamic and structural considerations of the models are based on accepted wing design principles. The wings were designed with a reasonably high aspect ratio to minimize the induced drag coefficient. The span however is typically limited by structural considerations of the spars so the aspect ratio was not set too high. The shape of the planform is designed such that the lift distribution gives nearly elliptic loading.

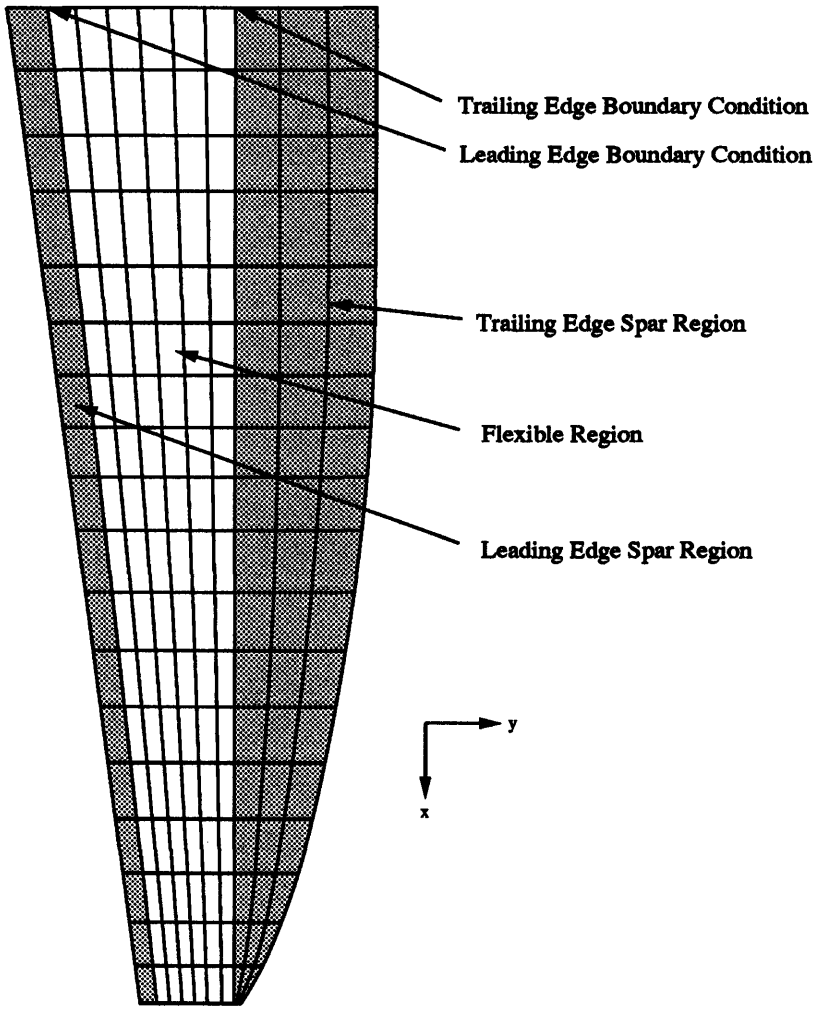

Figure 4-21: Typical Flexible Sailboard Fin Model

The 8 inch Flex Foil planform has a low surface area resulting in a high lift coefficient at typical operating point. The surface area is about half of a standard windsurfer fin. The higher lift coefficient takes advantage of the higher lift capabilities of the wing due to camber. The aspect ratio is moderately high for good induced drag performance.

The 10 inch planform has a larger surface area and higher aspect ratio than the 8 inch planform. This results in a lower operating lift coefficient than the 8 inch planform but better induced drag performance. The surface area is still significantly lower than standard fins again taking advantage of the higher lift capabilities of the

camber.

4.5.2 Convergence Tests

The convergence rate for the 8 inch Flex Foil Planform is shown in Figure 4-22 for a series of stiffness values. The initial $RMS\ \Delta z$ is higher for the lower stiffness numbers since the more flexible wings have a greater initial deflection than the stiffer wings. The stiffer wings converge faster as well.

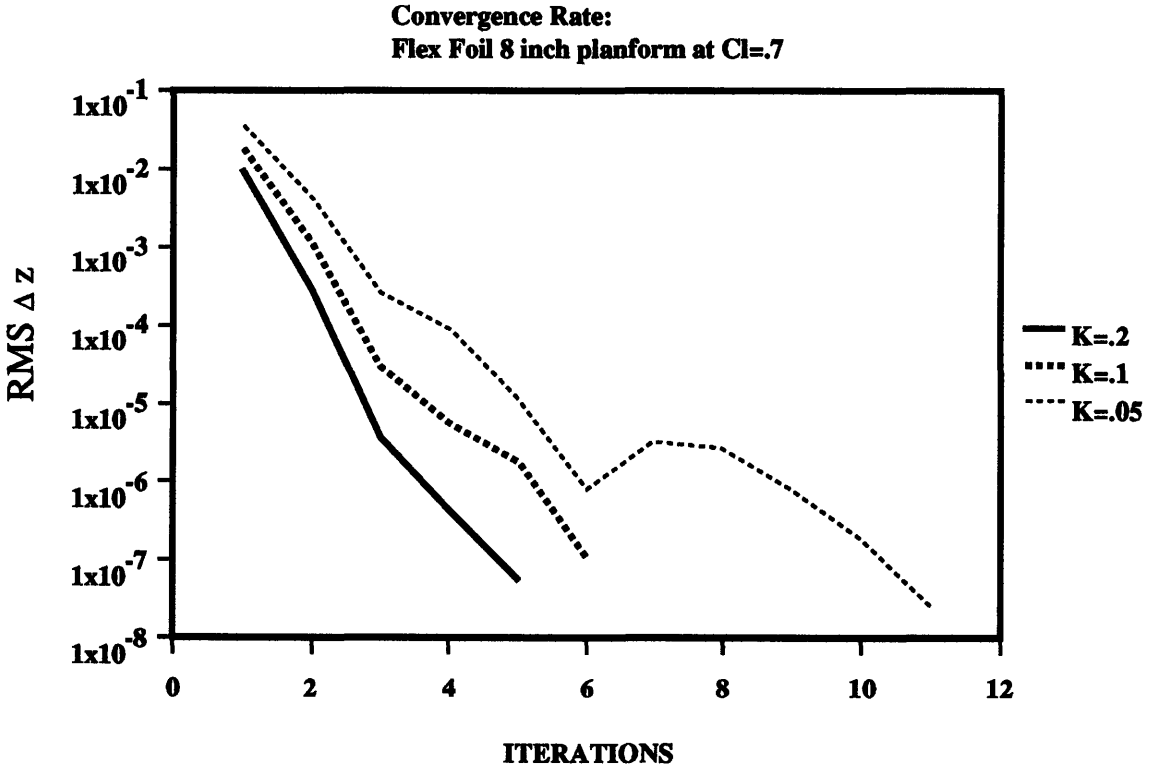

Figure 4-22: Convergence Rate

4.5.3 Linearity of Lift Curve

The lift curves for the Flex Foil 8 inch planform over a range of stiffnesses is shown in Figure 4-23. The lift curves are very linear for a broad range of stiffness values. The linearity of these lift curves is shown by the correlation coefficients very close to

1 (or -1) for each of the stiffness values in Table 4.3

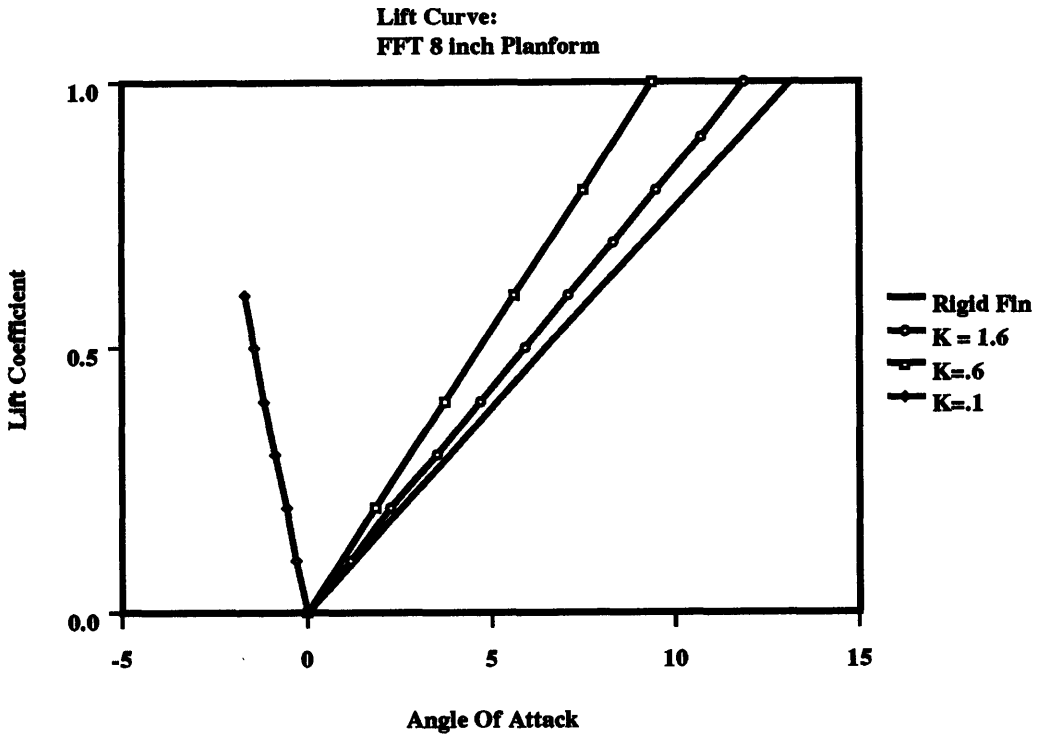

Figure 4-23: Linearity of Lift Curves for the 8 inch Flex Foil Planform

Table 4.3: Correlation Coefficients for 8 inch Flex Foil Planform

K	r
Rigid	0.99996
1.6	0.99996
0.6	0.99998
0.1	-0.99976

The linearity shown in these tests can be generalized to any of the wing planforms of any stiffness. The method produces completely linear lift curves due to the liearizations utilized in the numerics. Thus, any lift curve for any planform and any stiffness can be described by the line passing through any two lift points for this wing. The wings studied in this test are uncambered in their unloaded state, so their lift curves pass through $C_l = 0$ at $\alpha = 0$. Thus, the lift curves can be generated from this zero point and one non-zero data point. In fact the lift curve can be completely described by the slope of the lift curve. Thus for the actual tests, only one lift point

is generated.

4.5.4 Performance of 8 Inch Flex Foil Wing

The lift curve slope to stiffness relationship for the 8 inch Flex Foil Planform is shown in Figure 4-24. The data follows the inverse relationship shown for the tapered wings. Thus, the lift curve slope is given by

$$m = m_{rigid} + \frac{F}{K - K_{crit}} . \tag{4.24}$$

The curve fit shown in this figure follows this equation with $m_{rigid} = 4.345$, $F = 0.7$ and $K_{crit} = 0.18$. Thus the lift curve slope for this fin is

$$m = 4.345 + \frac{0.7}{K - 0.18} . \tag{4.25}$$

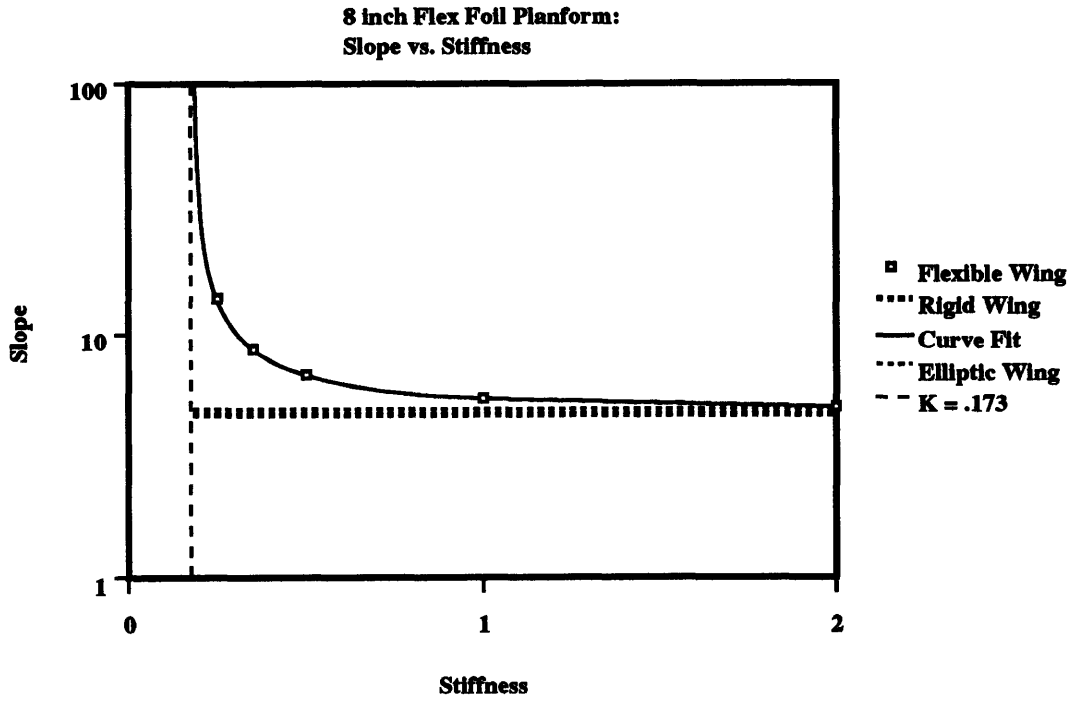

Figure 4-24: Performance Curve for 8 inch Flex Foil Planform

The results of the effective stiffness test for this planform are shown in Appendix A.

The comparison of the critical stiffness calculated numerically and the effective stiffness gives $A = 0.194$. This is close to A for the NACA thickness tapered wing which is 0.199.

4.5.5 Performance of 10 Inch Flex Foil Wing

The performance of the 10 inch planform is shown in Figure 4-25. For this wing, $K_{crit} = 0.173$, $F = 0.67$ and the rigid wing lift curve slope is $m_{rigid} = 4.636$. Thus the lift curve slope for the fin is given as

$$m = 4.636 + \frac{0.67}{K - 0.173} . \tag{4.26}$$

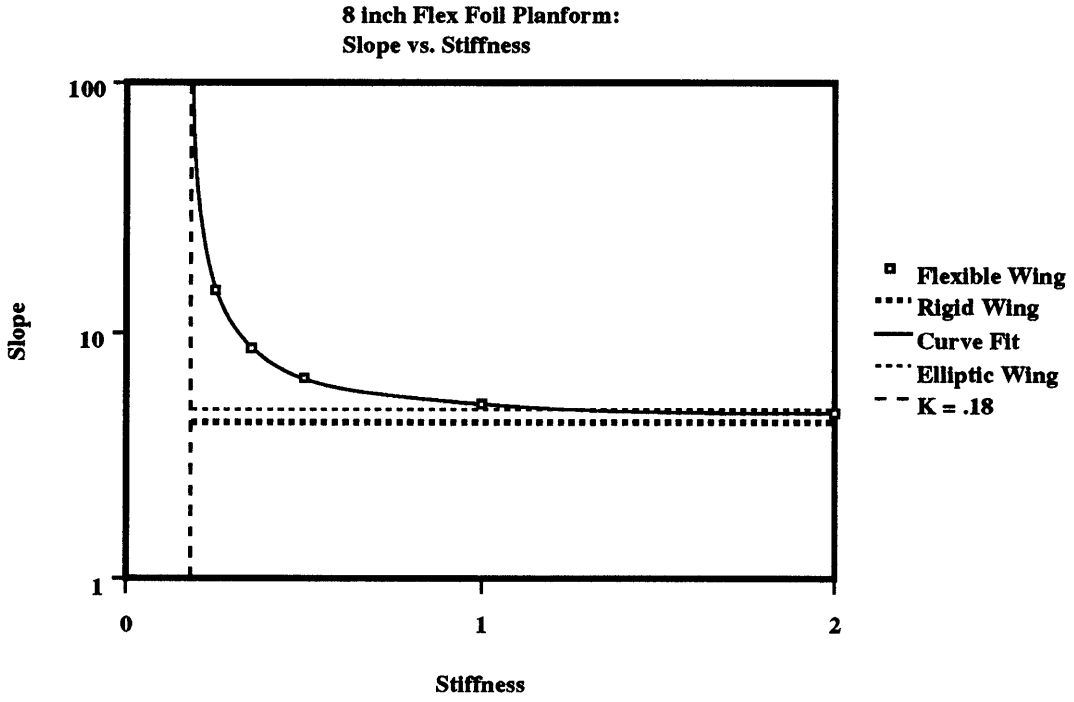

Figure 4-25: Performance Curve for 10 inch Flex Foil Planform

The results of the effective stiffness test for this planform are shown in Appendix A. The comparison of the critical stiffness calculated numerically and the effective stiffness gives $A = 0.203$. This is close to A for the NACA thickness tapered wing which is 0.199 as well as that for the 8 inch sailboard fin which is 0.194.

4.5.6 Critical Speed for 10 inch Fin

For the case of a wing that has been constructed of a particular material, the critical stiffness is related to a critical flow dynamic pressure. Since the plate stiffness, D, is fixed by the material properties of the wing, changes in the stiffness are related only to changes in the speed of the flow. Thus for a wing with fixed material properties, it is often useful to discuss the critical speed of the wing rather than the critical stiffness.

For the case of the 10 inch fin, a relationship between the flow speed and the lift curve slope can be determined. The modulus of the flexible material for this case is $4000psi$ and the airfoil is a 15% thick NACA section. The fin is operating in water. As can be seen in Figure 4-26, the slope of the lift curve increases as the speed increases until the wing reaches it's critical speed of approximately 30 knots.

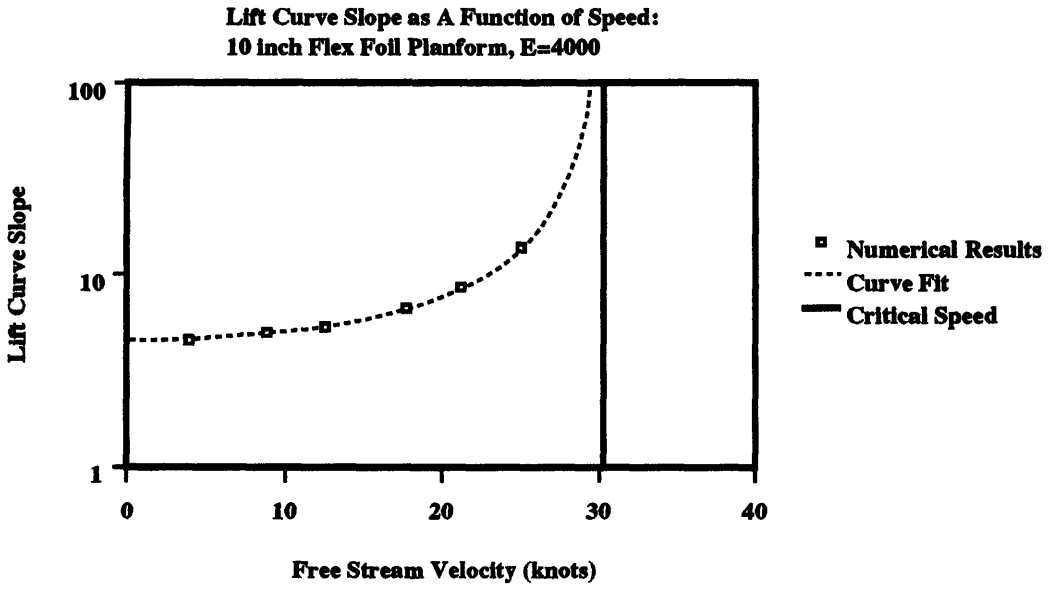

Figure 4-26: Critical Speed for 10 inch Flex Foil Planform

Chapter 5

Conclusions and Recommendations

The numerical analysis shown in Chapter 4 give the details on the performance of flexible wings. These curves can be unified into a concise set of performance curves that adequately describe the behavior of flexible wings. The following sections outline the results of the analysis in a simple set of performance equations.

5.1 Performance Characteristics of Flexible Wings

The results of the numerical analysis of flexible wings give a good indication of how they perform. The stability of the method and the quick convergence indicate the stability of real flexible wings and their response rate to changing operating points. The actual data shows how a flexible wing behaves at certain operating points.

5.1.1 Camber Stability

The quick convergence of the method indicates a strong stability of the camber of real flexible wings. As the wing changes shape, the loading quickly responds to the new shape. The numerical loading changes very little between iterations. The real loading acts in a similar way minimizing the dynamics of the structure and leading quickly to the final solution. The final camber shape is very stable for operation

above the critical stiffness.

5.1.2 Lift Performance

The lift coefficient for a particular wing is determined by the aspect ratio of the wing, its planform shape, its stiffness and its angle of attack. These parameters can be combined into a single equation for elliptically loaded wings:

$$C_L = \left(\frac{2\pi}{1 + \frac{2}{AR}} + \frac{F}{K - K_{crit\ airfoil}\left(1 - \frac{1.3}{AR}\right)}\right)\alpha \tag{5.1}$$

where AR is the aspect ratio of the wing, K is the stiffness of the the wing, α is the angle of attack and C_L is the lift coefficient as described earlier. $K_{crit\ airfoil}$ depends on the axle locations and the stiffness distribution along the chord. The proportionality coefficient, F, also depends on the Aspect Ratio of the wing and the spar placement.

For the case of the tapered wing ideally constrained at the leading and trailing edges, F is given from a curve fit of the data as

$$F = 5 \log AR + 0.05 . \tag{5.2}$$

Moving the spars to the 10% and 70% chord points changes F to

$$F = \log AR + 0.05 . \tag{5.3}$$

For the flexible wings, with the non,uniform thickness distribution, and the spars at the 10% and 70% chord locations, F is given as

$$F = 0.868 \log AR + 0.05 . \tag{5.4}$$

This equation is valid for nearly elliptically loaded wings as well. The more non-elliptic the span loading of the wing is, the further from the predicted lift the actual lift will be.

This equation shows the inverse relationship between the lift curve slope and the stiffness of the wing. For a given aspect ratio, the relationship of the lift coefficient,

C_L, and angle of attack,α, depends only on the stiffness, K in an inverse proportionality.

The proportionality coefficient gives an indication of the sensitivity of the lift curve slope to changes in the stiffness of the wing. The optimal drag performance of flexible wings has been experimentally determined to occur for a lift curve slope around 3 times greater than the rigid wing slope. The magnitude of F for the wing gives an idea of how close the design speed is to the critical speed. Low values of F indicate a sharp upturn in the lift curve slope near the critical stiffness and less difference between the optimal and critical stiffnesses. Larger values of F indicate a more gradual increase in the slope near critical and thus more of a difference between the optimal and critical stiffnesses.

The magnitude of F also indicates the range of near optimal stiffness. The flatter the slope to stiffness curve near the optimal stiffness, the wider the range of stiffnesses will result in near optimal performance. Larger F values give larger range of near optimal performance. Since F increases with the aspect ratio, the higher aspect ratio wings have a larger range of near optimal stiffnesses.

5.1.3 Angle of Attack

In order to avoid the aeroelastic divergence at K_{crit}, the numerical program for this study sets the lift coefficient and determines the angle of attack rather than the other way around. Although this is the reverse of the way wind tunnel experiments are performed, it is a valid method for analysis. However, the primary resulting equation given above, is monotonic allowing it to be inverted so that the more standard C_L, α formulation can be used. This inverse relationship is simply

$$\alpha = \frac{C_L}{\left(\frac{2\pi}{1+\frac{2}{AR}} + \frac{F}{K - K_{crit\ airfoil}\left(1-\frac{1.3}{AR}\right)}\right)}. \tag{5.5}$$

This is simply a rewritten form of Equation 5.1. This form is included since the numerical methodology that is used to gather the data, takes the lift coefficient as the input and determines the angle of attack. This form avoids the singularity at

the critical stiffness, K_{crit}. This form can even obtain the negative angles of attack that occur for stiffness values lower than K_{crit} (although there is very little numerical verification of this range of stiffnesses).

5.1.4 Variation of Parameters with Planform Type

The performance curves that have been generated for the tapered wing planforms can be used to predict the performance of a more general planform. However, the accuracy of the predictions depends on how closely the planform of the real wing is to the tapered model. In the case of the flexible sailboard fins, the trailing edge of the wing is not straight so that the load is closer to an elliptic distribution. However, the curve of the trailing edge also changes the positions of the spar rotation axes relative to the local chord. Near the midspan of the wing, the trailing edge spar makes up a larger percentage of the local chord than it does near the tip or root. The value of K_{crit} and F are both highly dependent on the placement of the boundary conditions. Thus, the values of K_{crit} and F that are predicted by the performance curves are not extremely accurate.

However, the effective stiffness test gives a very good prediction of the critical stiffness. The value of A for the tapered planform with the NACA thickness distribution is very close to the value of A for the sailboard fin planforms for the same thickness distribution. Thus, if the value of A for the tapered planform is used to predict K_{crit} based on the effective stiffness test for the sailboard fin planforms, the predicted K_{crit}s very closely match the K_{crit} calculated numerically.

5.1.5 Low Aspect Ratio Performance

Flexible wings do not perform well at very low aspect ratios. At low aspect ratios the loading due to camber is not positive over the chord but rather dips negative over the half of the chord loser to the leading edge. This not only does not provide lift, but also does not support the camber that causes it. Thus the flexible chordline will be unstable and the benefits of camber will not be achieved.

Lifting line theory suggests a flexible wing with an aspect ratio less than 1.3 can not achieve any significant performance advantages over a rigid wing. Below 1.3, the wing loading due to pure camber should not support that camber. For higher values of the stiffness parameter, the lift curve does increase slightly over the rigid wing, but the wing becomes unstable before reaching critical stiffness. For loadings due mainly to angle of attack and only partially to camber, the leading edge loads tend to offset the negative loads due to the camber and the camber is supported by these loads. However, as the lift curve slope increases, this leading edge load due to angle of attack decreases and the chord line becomes unstable. Thus the wing does not have a well defined critical stiffness nor useful operation at low angles of attack.

The numerical analysis tends to confirm this idea, although the aspect ratio where it occurs tends to be slightly lower than predicted by lifting line theory. A wing with an aspect ratio of 1.2 had a converged solution at zero angle of attack, indicating the critical stiffness for the wing and thus that the aspect ratio where wings no longer show the full range of behavior is actually lower than 1.2. However, in this aspect ratio range, the numerical method converges very slowly, indicating that the stability is weak. A numerical analysis for an ideal wing of aspect ratio 1 could not arrive at a converged solution for an angle of attack of zero.

Low aspect ratio flexible wings have very low proportionality coefficients F. The low value for F indicates that the range of stiffness parameter values where substantial benefits can be derived from camber is small. Thus the difference between the optimal operating stiffness parameter value and the critical stiffness is small.

5.1.6 Drag Performance

The numerical analysis used in this study to determine the performance of flexible wings is only capable of determining the induced drag on the wing. The camber of the wing does not affect the induced drag significantly since the induced drag is simply a function of the span loading which varies very little as the camber changes. For an elliptically loaded wing, the induced drag is simply a function of the lift coefficient and the aspect ratio of the wing.

$$C_{Di} = \frac{C_L^2}{\pi\, AR} \tag{5.6}$$

For non-elliptically loaded wings, the induced drag follows the same form as in Equation 5.6, but is slightly modified to account for the non-ellipticality with a planform efficiency coefficient, e.

$$C_{Di} = \frac{C_L^2}{\pi\, AR\, e} \tag{5.7}$$

This efficiency coefficient is a function of the shape of the span loading of the wing. For an elliptically loaded wing, it is one, and for any other wing it is less than one. In general, this coefficient is rather close to one for most planforms. The tapered planforms studied here have an efficiency coefficient on the order of 0.8 to 0.9.

The span loading of a flexible wing does not typically change significantly as the stiffness changes. This is mainly due to the cambering behavior of the wing. Since the camber at any spanwise location of the wing is not only affected by the loading at that point, but the overall plate bending induced by the total loading, the camber tends to be more evenly distributed than the span loading. Thus, at the tip where the load is low, the camber is greater than the two-dimensional plate theory would predict for that airfoil cross-section. Similarly, at the root, where the loading is high, the camber tends to be lower than the two-dimensional plate theory would predict. This camber distribution tends to distort the ellipticality of the loading by decreasing the load at the root and increasing it near the tip. Thus, the efficiency coefficient for the cambered wing remains relatively close to that of the rigid wing and the induced drag polar does not change significantly from that of the rigid wing. This is seen for the case of the tapered planforms in Figure 4-5 and Figure 4-11.

In general, for nearly elliptically loaded wings, the induced drag for the wing depends only on the planform and the lift coefficient only. Thus, the lift to induced drag ratio for a flexible wing is nearly constant for constant lift no matter what the flexibility or camber of the wing.

The camber does, in general, have a significant impact on the viscous drag of

the wing. The numerical analysis utilized in this study cannot determine the viscous drag effects on the wing and thus cannot determine the effect of flexibility on the viscous drag. However, once the steady state camber has been determined from this method, and a thickness distribution chosen, the viscous drag of the airfoils or the entire wing can be determined by utilizing other numerical analyses such as XFOIL mentioned earlier. The results of the analysis described in Section 2.3 give the optimal performance for a flexible airfoil. This minimum drag occurs when about 3/4 of the lift comes from camber and 1/4 from angle of attack. This should hold true for the airfoil sections of a flexible wing as well.

5.2 Design of Flexible Wings

The results of this study give a good indication of the performance characteristics of flexible wings. The results can be used by aerodynamic designers that wish to utilize flexible wings in their vehicle designs.

5.2.1 Steady Load Lifting Surfaces

Flexible wings can be applied to the steady lifting surfaces. However, in order for these wings to have an advantage over standard fixed geometry wings, the range of operating lift should be large. One example of a situation where this occurs is in the keels of sailboats or the fin on a windsurfer. The lift requirement for both of these devices is relatively constant in magnitude, but switches direction as the craft "tacks" or "jibes" from one direction of travel to another. In this case, the camber response of the flexible wing can switch direction as the direction of loading on the keel changes.

In order to properly design a keel of fin to perform at an optimal level for such an application, the designer must first understand the operating requirements of the craft such as speed and lift. A planform should be chosen that can generate high lift coefficients (0.5 to 0.8) for these operating requirements. The aspect ratio of the wing is often chosen due to structural constraints of the spars or depth requirements

of the keel itself. The spar placement is also determined by structural constraints.

The viscous analysis shown in Section 2.3 indicates that for an optimal lift to drag ratio occurs for a lift curve slope around three times that of a rigid wing for Reynolds Numbers on the order of 10^7. By performing a similar viscous drag analysis for the design operating point, the designer can determine a lift curve slope that maximizes the lift to drag ratio at the operating lift coefficients. The value of the stiffness parameter of the wing can be determined from the slope using some of the performance curves in this study. Finally, the material properties of the wing such as the modulus, can be determined from the stiffness and the operating point through the equations presented above.

5.2.2 Control Surfaces

Control surfaces are often required to operate over a wide range of lift requirements. Flexible wings can be used to enhance the performance of these surfaces by lowering the drag associated with the control actions and improving the control authority of the surface. By adding camber to the surface as the lift need goes up (or negative camber for negative lifts) the control surface can have a much greater range of lift outputs than a fixed geometry surface. This allows the designer to chose a lower surface area planform (with an associated lower drag) or to have greater control authority with the same planform as the rigid control surface.

The passive nature of the camber response allows the operator to achieve these advantages without the added complexity of mechanical actuators or other active shaping devices. The automatic response also allows keeps the surface in an optimal configuration through quick maneuvering. The lower drag associated with such maneuvers through the use of the flexible wings should be an advantage to nearly all vehicles. This device could be applied to the elevators or tail surfaces of aircraft as well as the rudders of sailboats.

The lift curve slope for control surfaces represents the control gain of the system. The designer can tailor the gain of the system by selecting the proper wing stiffness to achieve the desired lift curve slope. However, the designer should avoid the critical

stiffness, where the gain becomes infinite and the control forces can no longer be commanded. In most cases the design will provide lowest drag far enough from the critical stiffness that this should not pose a problem to the designer.

5.3 Recommendations for Further Study

This study looks at several of the important parameters that govern the behavior of flexible wings. However, there are several more characteristics of flexible wings that should be explored in the future. It is also important to verify these performance characteristics outside of the numerical environment of the program used here by conducting wind tunnels tests or other experimental tests.

5.3.1 Spar Placement

The spar placement correction given in Equation 2.12 from Widnall, is simply a curve fit of available 2-D data. This model should be explored more carefully to see if there is a better formula that could be used. It may also prove an interesting study to show the effect on the performance of other spar locations.

The spars in the wings in this model are placed in the model such that the proportions of the chord that are in front of, between and behind these spar locations are roughly constant over the span. It may be interesting to explore cases where this proportionality is not so constant or even cases where the axes of rotation of the spars are external to the structure for part of the span. For example, in the case of the tapered wing, if the leading edge spar axis of rotation were perpendicular to the root chord, the axis of rotation would be substantially ahead of the leading edge at the wing tip. The performance of such a wing would be drastically different from the tapered wings where the axis of rotation is within the structure.

5.3.2 Viscous Drag

This study utilized an extremely simplified model that did not include any of the effects of viscous drag, which is where cambered wings gain most of its performance advantages. The performance optimization must therefore include these viscous effects. This could be done by either replacing the vortex lattice with a viscous panel program or more simply, by post processing the converged result of a numerical program similar to the one presented here with a viscous flow solver.

5.3.3 Planforms

This study was mainly concerned with the simple tapered wing planforms. These planforms are nearly elliptically loaded and thus follow the theory reasonably well. Further study on other types of planforms with more or less elliptic load distributions may enhance flexible wing theory.

5.3.4 Non-Uniform Stiffness in the Spanwise Direction

The stiffness parameter, K, was considered to be constant over the span of the wing for these tests. However, better performance may be achieved by varying the stiffness in the spanwise direction. Making the wing stiffer near the tip or stiffer near the root may have beneficial or adverse affects on the spanwise camber distribution and change the performance characteristics.

5.3.5 Other Non-Uniform Chordwise Stiffness Distributions

Two chordwise stiffness distributions were chosen for this study. The uniform chordwise stiffness distribution gives a good simple model for the flexible wings. The plate stiffness that accounts for real airfoil thickness distributions gives a good idea of how the performance curves are modified for non-uniform stiffness distributions. These are two of only a large number of possible stiffness distributions that can be utilized.

In particular, the chordwise stiffness distribution could be modified to shift the camber closer to the leading edge or the trailing edge. Although the inviscid results presented here may not be drastically modified by a change in the stiffness distribution, a viscous analysis may show a marked performance improvement for a slightly different stiffness distribution.

There is also an issue of changing the spanwise stiffness distribution. By adding stiffness near the root or near the tip, it may be possible to modify the span loading of the wing to make it more elliptical. This would, in general, depend on the particular planform that is used.

5.3.6 Wind Tunnel Tests

As with other aerodynamic devices, wind tunnel tests can be used to verify or enhance numerical solutions. It is important to be able to reproduce the performance of the flexible wings in the wind tunnel to prove the stability and accuracy of the method.

5.3.7 Shred

One of the primary applications to date is the application to windsurfer fins as developed by Flex Foil Technology Incorporated. Possibly one of the best ways to see the benefits of flexible wings is to put one of these fins on your board and go sailing. The lower drag results in improved speed which any high performance sailor should feel.

Although these fins are not yet available to the general public, they may soon be on the market. Until they are, if you see a sailor fly by you on the water and you can't figure out why he is going so fast, it could be that he is one of the test pilots for Flex Foil trying out one of their new secret weapons.

Appendix A

Effective Stiffness Analysis

The numerical results for a number of effective stiffness tests are presented in this appendix to show a typical solution. The examples that have been selected and presented here are not the complete set of analyses, but rather give a few typical results to demonstrate the methodology of the test. These examples should give the reader a good idea of the details of the analysis process and allow the reader to more easily reproduce the results.

A.1 Two-Dimensional Effective Stiffness Tests

The Effective stiffness tests described in Section 2.4.2 can be used to determine the critical stiffness, K_{crit} of a two-dimensional flexible airfoil section. The bending of a infinite plate under an distributed line load gives the load to deflection ratio for the airfoil. This ratio gives the effective stiffness of the plate

$$S_{eff} = \frac{P}{w}. \tag{A.1}$$

where P is the load per unit span and w is the deflection of the plate at the point of loading.

The load is applied at the midpoint between the boundary conditions. For these two-dimensional tests, a unit square plate is loaded with a load of 100 distributed

along a line midway between the boundary conditions. The plate has 10 elements along each edge (11 nodes along each edge). The load is applied to a line spanning the plate containing 11 nodes. This load is applied in a consistent way by applying a load of 10 to all 9 interior nodes and a load of 5 to each of the 2 edge nodes. Thus a total load of 100 is applied to the plate.

The critical stiffness for the airfoils is given from calculations based on the plate equation

$$D \frac{\partial^4 w(x)}{\partial x^4} = p_z(x) . \tag{A.2}$$

From the definition of the stiffness parameter

$$K \equiv \frac{D}{q_\infty (\frac{c}{2})^3} \tag{A.3}$$

the critical dynamic pressure is given as

$$q_{crit} = \frac{D}{K_{crit} (\frac{c}{2})^3} . \tag{A.4}$$

This value for the critical stiffness is compared to the effective stiffness for the airfoil giving a value for A as

$$A = \frac{q_{crit}}{S_{eff}} . \tag{A.5}$$

A.1.1 Plate with Ideal Boundary Conditions

The effective stiffness test is used to determine the critical stiffness of an ideal flexible airfoil. The geometry and boundary conditions for the plate as well as the consistent nodal loading that is applied are shown in Figure A-1.

The plate used for this test has an elastic modulus $E = 3.000 \times 10^5$, a Poisson's ratio $\nu = 0.3$ and a thickness $h = 0.12$. The plate stiffness, D, is given by

$$D = \frac{E\, h^3}{12(1 - \nu^2)} \tag{A.6}$$

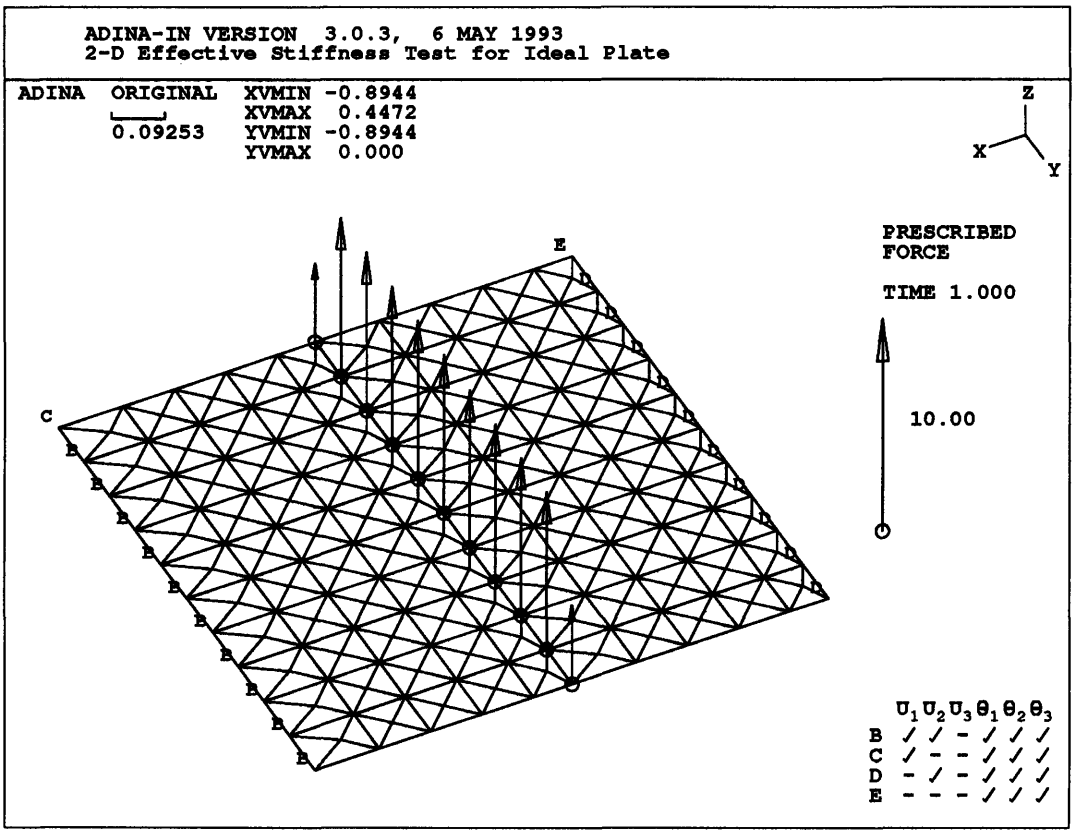

Figure A-1: Effective Stiffness Test: Ideal B.C.s

For this model, $D = 47.5$.

The deflection of the plate is shown in Figure A-2. Under the applied load of 100, the average deflection of the midchord, w, is 0.038 Thus, the effective stiffness, S_{eff}, is 2631.

The critical stiffness for an ideally supported airfoil is given as $K_{crit} = 1.4$. Thus, the critical dynamic pressure is

$$q_{crit} = \frac{D}{K_{crit}(\frac{c}{2})^3} \tag{A.7}$$

giving a value of $q_{crit} = 271.27$

Given $S_{eff} = 2631$ from the effective stiffness test, A is calculated to be 0.1031.

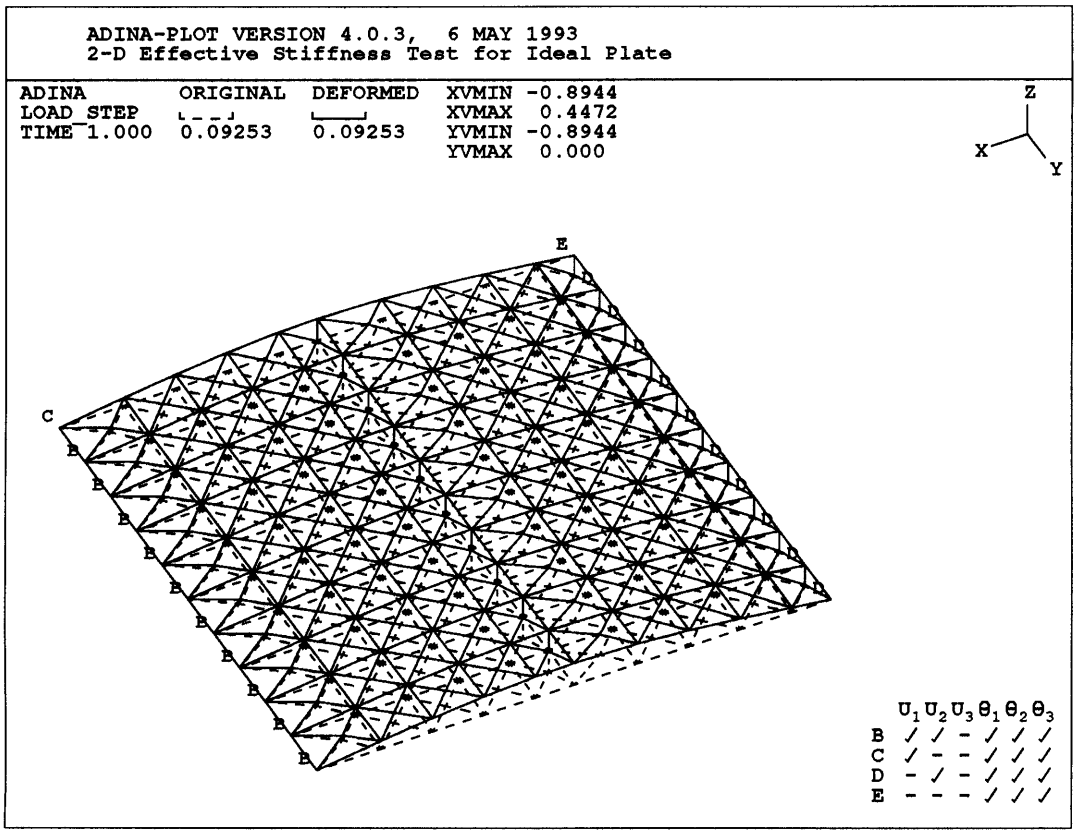

Figure A-2: Effective Stiffness Test: Ideal B.C.s

A.1.2 Plate with Spar B.C.s and Uniform Thickness

The critical stiffness for the two-dimensional airfoil sections for the wing with the boundary conditions at the 10% and 70% chord locations can be determined from the effective stiffness of a plate with these boundary conditions. The plate used for this test has a modulus of $E = 1.000 \times 10^5$, a Poisson's ratio of $\nu = 0.3$ and a uniform thickness of $h = 0.12$ giving a plate stiffness of $D = 15.82$. The load and boundary conditions for this effective stiffness test are shown in Figure A-3.

The displacement of the test plate is shown in Figure A-4. The deflection at the midspan for this test is 0.02878 giving an effective stiffness of $S_{eff} = 3475$.

For a flexible airfoil with a uniform plate thickness and the spars placed at the 10% and 70% chord positions, the critical airfoil stiffness is given by Widnall *et. al.* as K_{crit} is 0.35. The critical dynamic pressure is then $q_{crit} = 361.7$. Thus, the value for A for this airfoil is 0.1041.

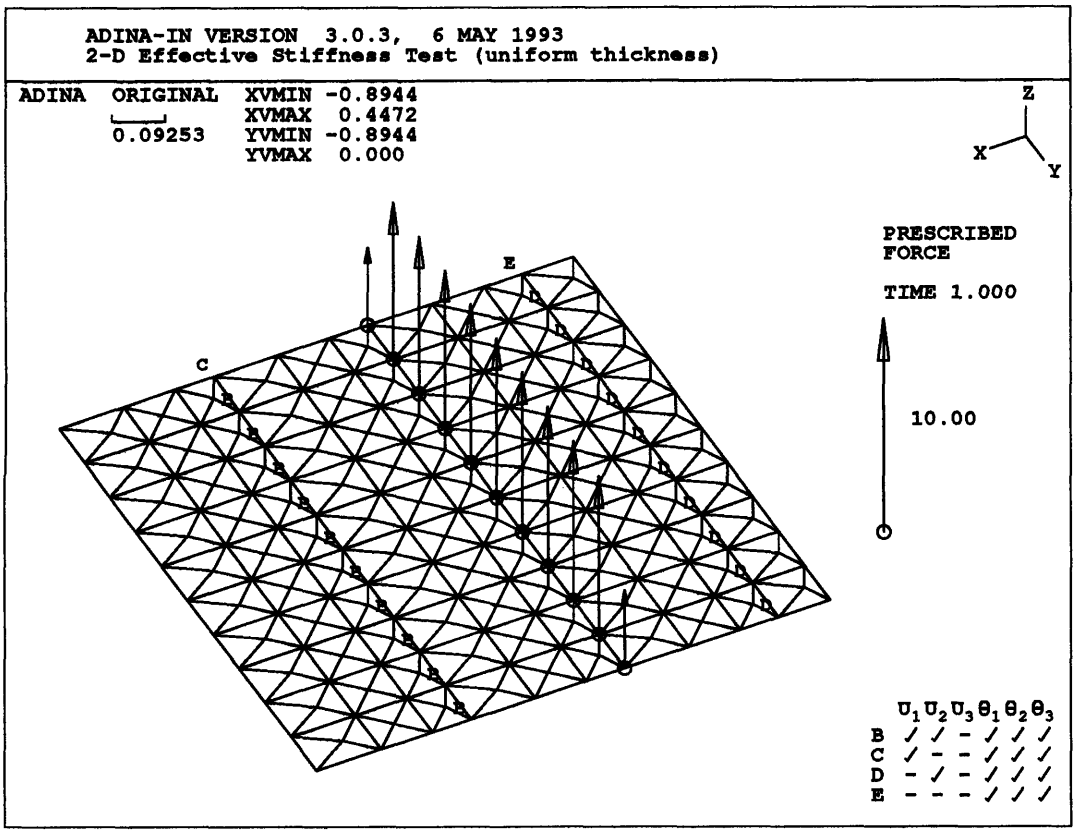

Figure A-3: Effective Stiffness Test: Spar B.C.s and Uniform Thickness

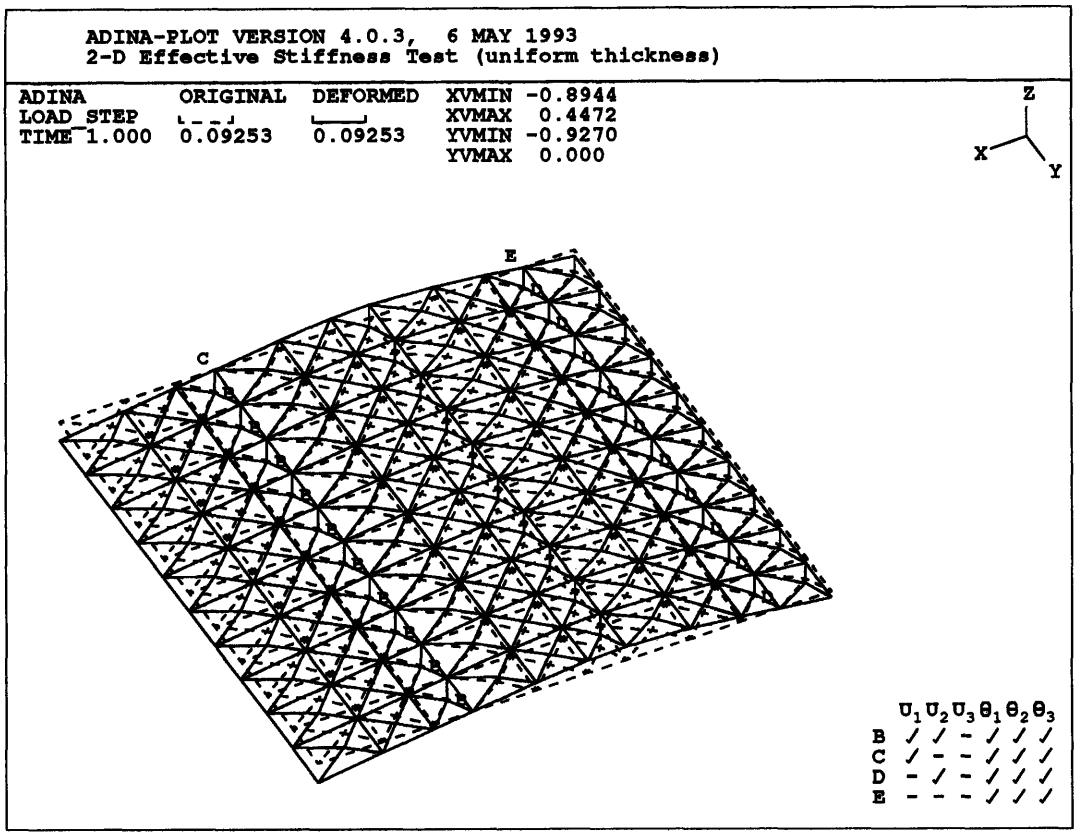

Figure A-4: Effective Stiffness Test: Spar B.C.s and Uniform Thickness

A.1.3 Plate with Spar B.C.s and NACA Thickness

The critical stiffness for the two-dimensional airfoil with the boundary conditions at the 10% and 70% chord locations and the NACA thickness distribution can be determined from the effective stiffness test. The plate used for this test has a modulus of $E = 1.000 \times 10^5$, a Poisson's ratio of $\nu = 0.3$ and an average thickness of $h = 0.132467$ giving an average plate stiffness of $D = 21.28$. The load and boundary conditions for this effective stiffness test are shown in Figure A-5.

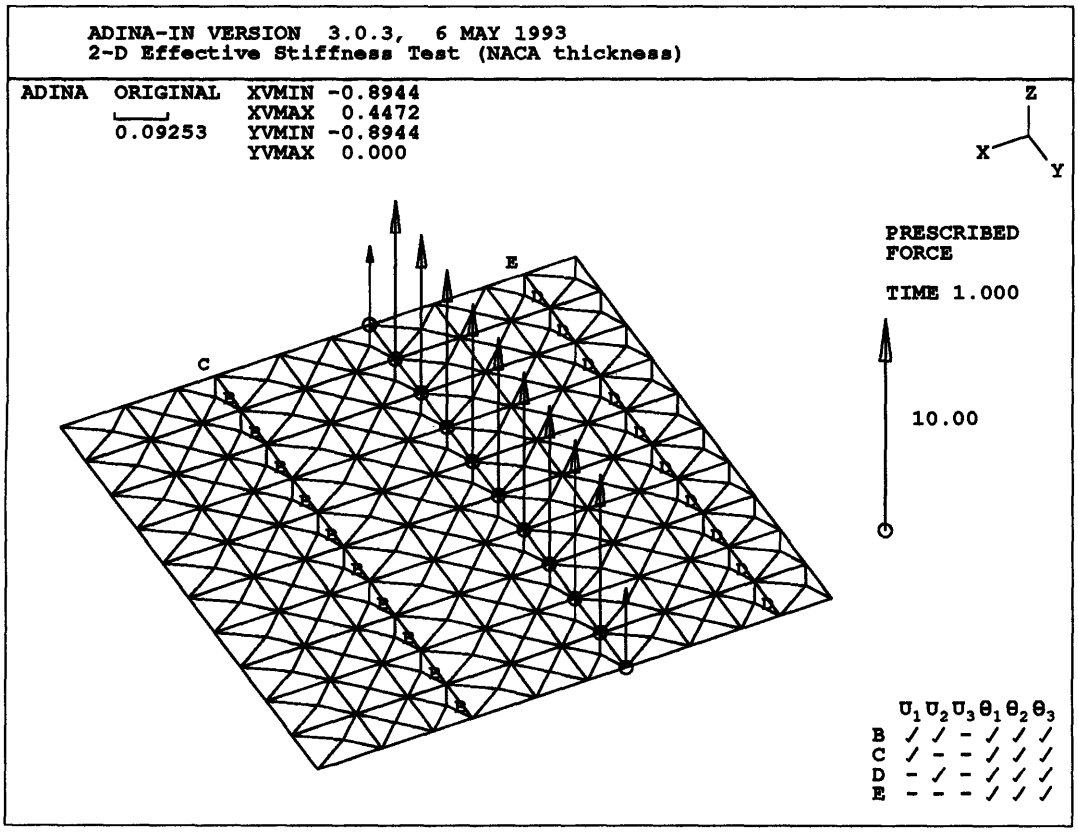

Figure A-5: Effective Stiffness Test: Spar B.C.s with NACA Thickness

The displacement of the test plate is shown in Figure A-4. The deflection at the midspan for this test is 0.01804 giving an effective stiffness of $S_{eff} = 5543$.

For a flexible airfoil with a uniform plate thickness and the spars placed at the 10% and 70% chord positions, the critical airfoil stiffness is given as K_{crit} is 0.30. The critical dynamic pressure is then $q_{crit} = 567.6$. Thus, the value for A for this airfoil is 0.1024.

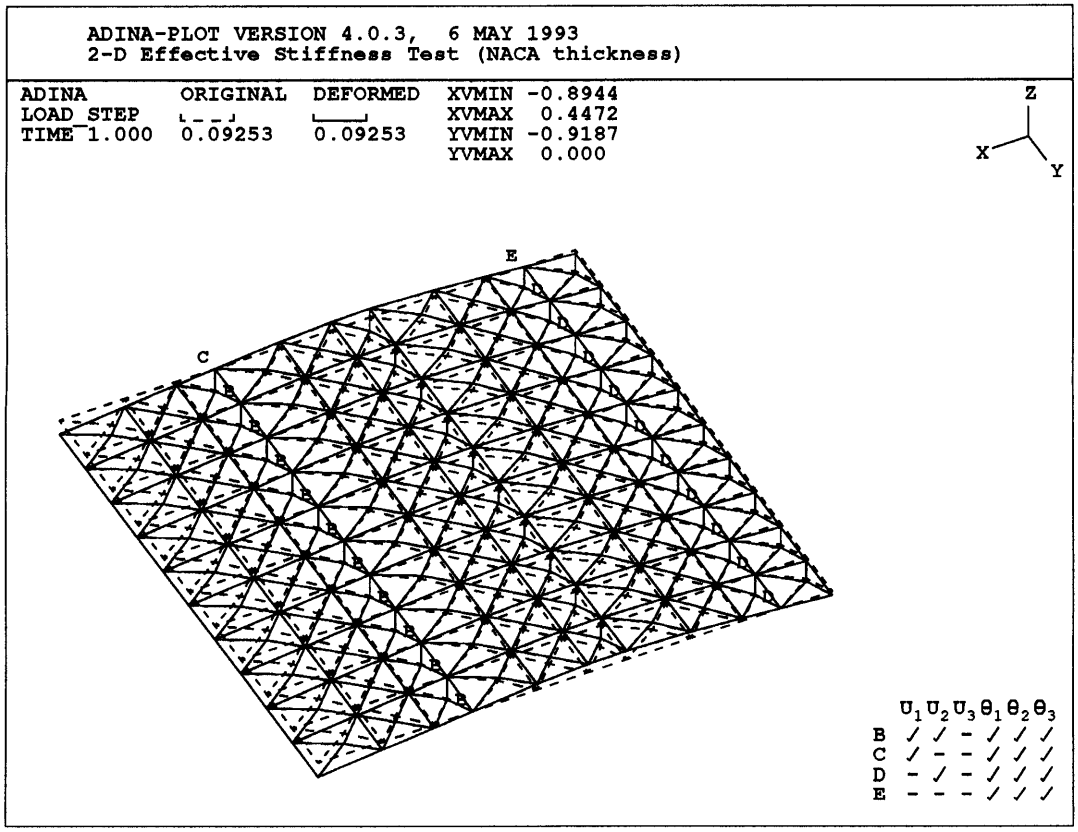

Figure A-6: Effective Stiffness Test: Spar B.C.s and NACA Thickness

A.1.4 Determination of Airfoil Critical Stiffness

A summary of the two dimensional effective stiffness tests is given in Table A.1.

Table A.1: 2-D Critical Stiffness Calculations

Effective Stiffness Tests			
Parameter	Ideal Plate	Spars/Uniform	Spars/NACA
E	300000	100000	100000
nu	0.3	0.3	0.3
thickness (max)	0.12	0.12	0.132467
D	47.472527	15.824176	21.286314
P	100	100	100
w	0.038	0.02878	0.01804
S eff	2631.5789	3474.6352	5543.2373
K crit	1.4	0.35	0.30
q crit	271.27159	361.69545	567.63504
A	0.1031	0.1041	0.1024

A.2 Tapered Wing

Tapered wings are used to generate a set of performance curves for general flexible wings. There types of tapered wings are studied. The idealized theory for flexible wings is determined from a set of tapered flexible wings with the boundary conditions enforced at the leading and trailing edges of the wing. This theory is then modified to account for the boundary conditions enforced by the spars. Two types of tapered wings with spars are studied. The first is a wing with a constant plate thickness in the chordwise direction. The second is a similar set of wings with a chordwise plate thickness distribution given by the thickness distribution of a NACA 0015 airfoil. Since all three cases use the same planforms, the results can be compared to isolate the effects of the non-idealities of the spars and the non-uniform thickness distribution. The examples shown here involve a tapered wing of aspect ratio 5.

The effective stiffness of the wing is defined in the same way as for the airfoil as are the stiffness parameter and the critical dynamic pressure. However, the dynamic pressure in this case is for a full three dimensional wing and must take into account the aspect ratio effects when compared to the effective stiffness. Thus, A is defined

as

$$A = \frac{q_{crit}(1 - \frac{1.3}{AR})}{S_{eff}} . \tag{A.8}$$

A.2.1 Ideal Boundary Conditions

The first tapered wing case is the wing with the boundary conditions enforced at the leading and trailing edge. This case can be compared to the two-dimensional ideal airfoil so that the effects of aspect ratio alone can be studied. The results of the effective stiffness test can be compared to the critical stiffness that is obtained numerically.

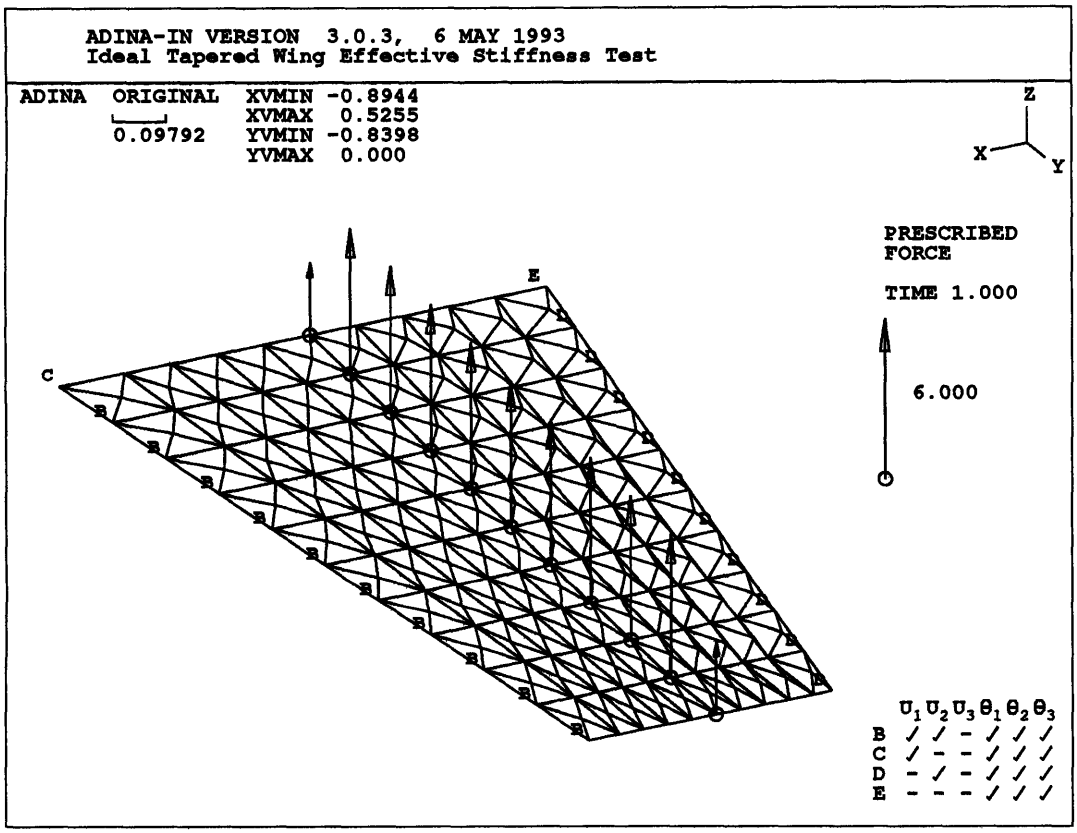

Figure A-7: Ideal Tapered Wing: Effective Stiffness Test Loading

The wing is loaded as shown in Figure A-7. This loading case is the consistent nodal loading for $P = 32$ $(load/unit\ span)$. The material properties of this wing are given as $E = 1.0 \times 10^5$, $\nu = 0.3$. The thickness of the plate is constant in the

chordwise direction, but varies in the spanwise direction such that the local thickness is 12% of the local chord. In this way, the stiffness parameter, K, is constant along the span.

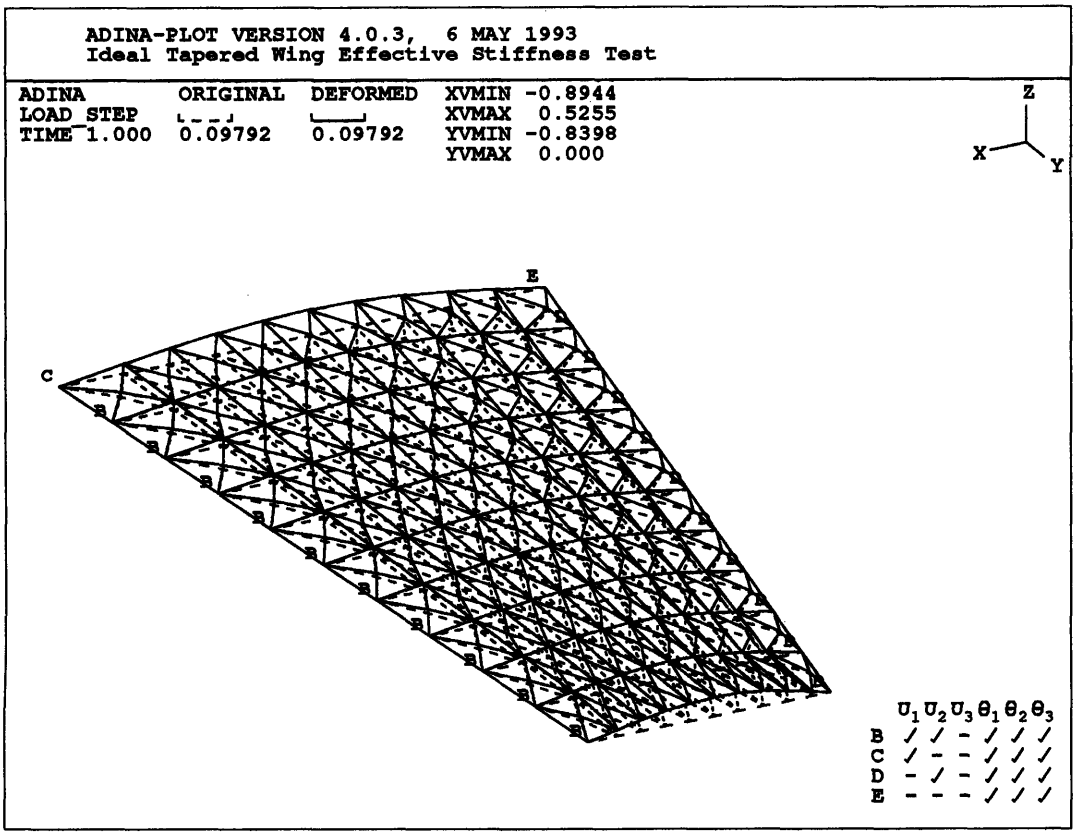

Figure A-8: Ideal Tapered Wing: Effective Stiffness Test Deflection

As explained in Section 2.4.2, the deflection, w, is measured at the midspan. The deflection for the effective stiffness case is shown in Figure A-8. The deflection at the half span is 0.038 giving the wing effective stiffness $S_{eff} = 834$.

The critical stiffness measured numerically is $K_{crit} = 0.9751$. Accounting for the aspect ratio correction, the airfoil stiffness parameter for this wing is $K_{crit\ airfoil} = 1.32$. Thus, the critical dynamic pressure $q_{crit} = 95.9$ Thus the calculated A is 0.115.

A.2.2 Spar B.C.s and Uniform Thickness

The second tapered wing case is a wing with the boundary conditions enforced at the 10% and 70% spar locations at the root of the wing. The plate thickness for this case is uniform in the chordwise direction. The critical stiffness for the airfoil sections for this wing are given by Equation 2.12 as 0.35.

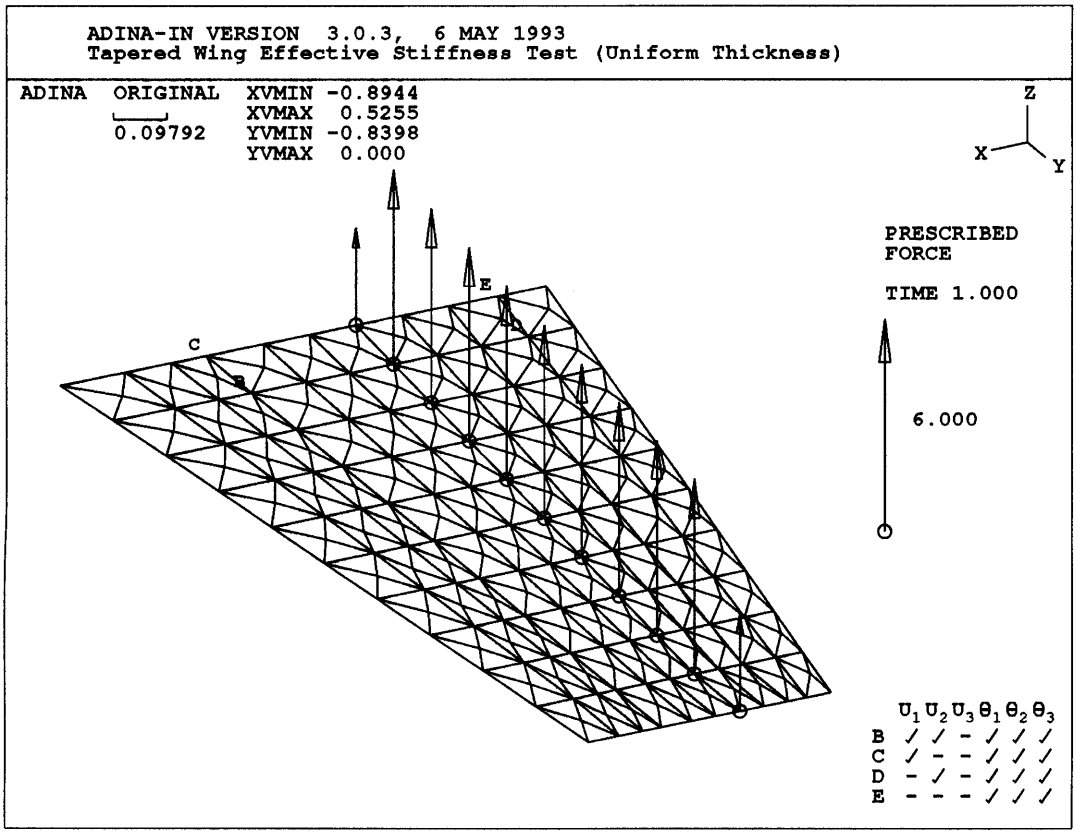

Figure A-9: Ideal Tapered Wing: Effective Stiffness Test Loading

The wing is loaded as shown in Figure A-9. This loading case is the same consistent nodal loading for $P = 32$ (*load/unit span*) as given in the ideal effective stiffness test described in the previous section. The material properties of this wing are given as $E = 5.0 \times 10^4$, $\nu = 0.3$. The thickness of the plate varies in the spanwise direction such that the local thickness is 12% of the local chord.

The deflection for the effective stiffness case is shown in Figure A-10. The deflection, w, measured at the midspan is 0.018 giving the wing effective stiffness $S_{eff} = 1769$.

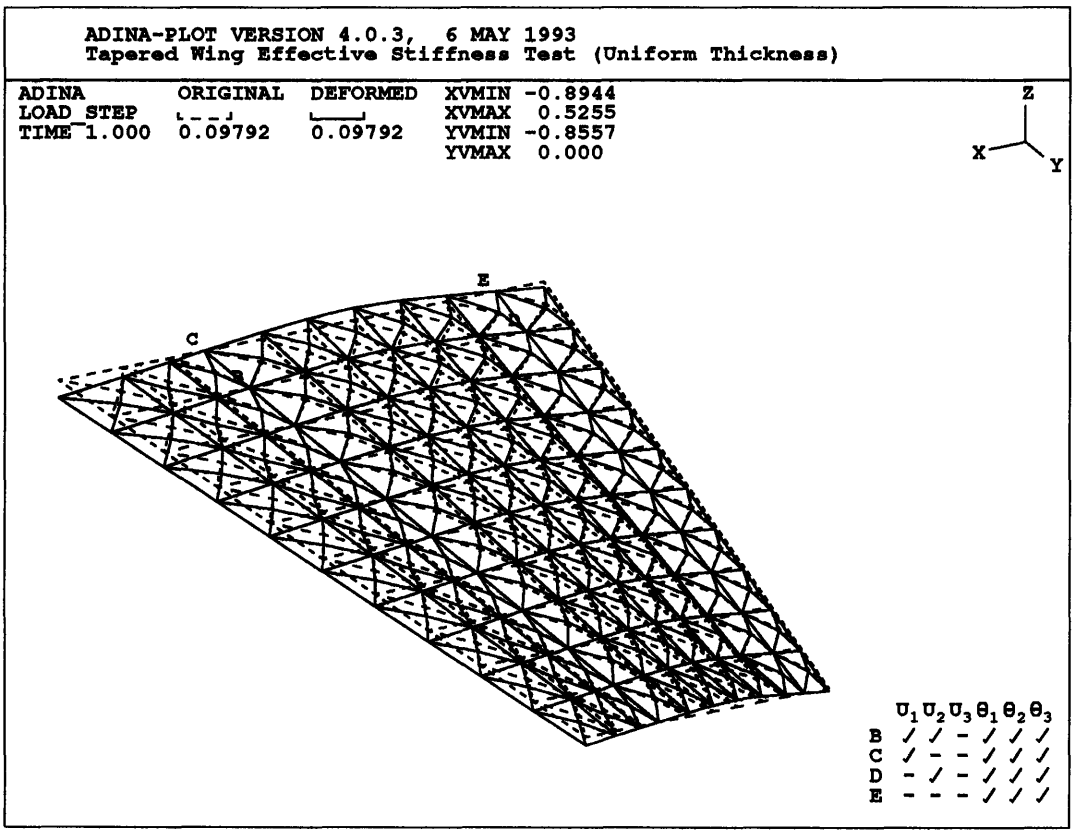

Figure A-10: Ideal Tapered Wing: Effective Stiffness Test Deflection

The critical stiffness measured numerically is $K_{crit} = 0.2174$. Accounting for the aspect ratio correction, the critical stiffness for this wing is $K_{crit\ airfoil} = 0.294$. Thus, the critical dynamic pressure for this wing $q_{crit} = 215.29$, giving $A = 0.1217$

A.2.3 Spar B.C.s and NACA Thickness

The final tapered wing case is also a wing with the boundary conditions enforced at the 10% and 70% spar locations at the root of the wing. The plate thickness for this case, however is given by a NACA airfoil thickness distribution in the chordwise direction. There is no expression in the prior work to estimate the critical stiffness for the airfoil sections for this wing. However, from the effective stiffness test in Section A.1.3, the airfoil K_{crit} is estimated to be approximately 0.30.

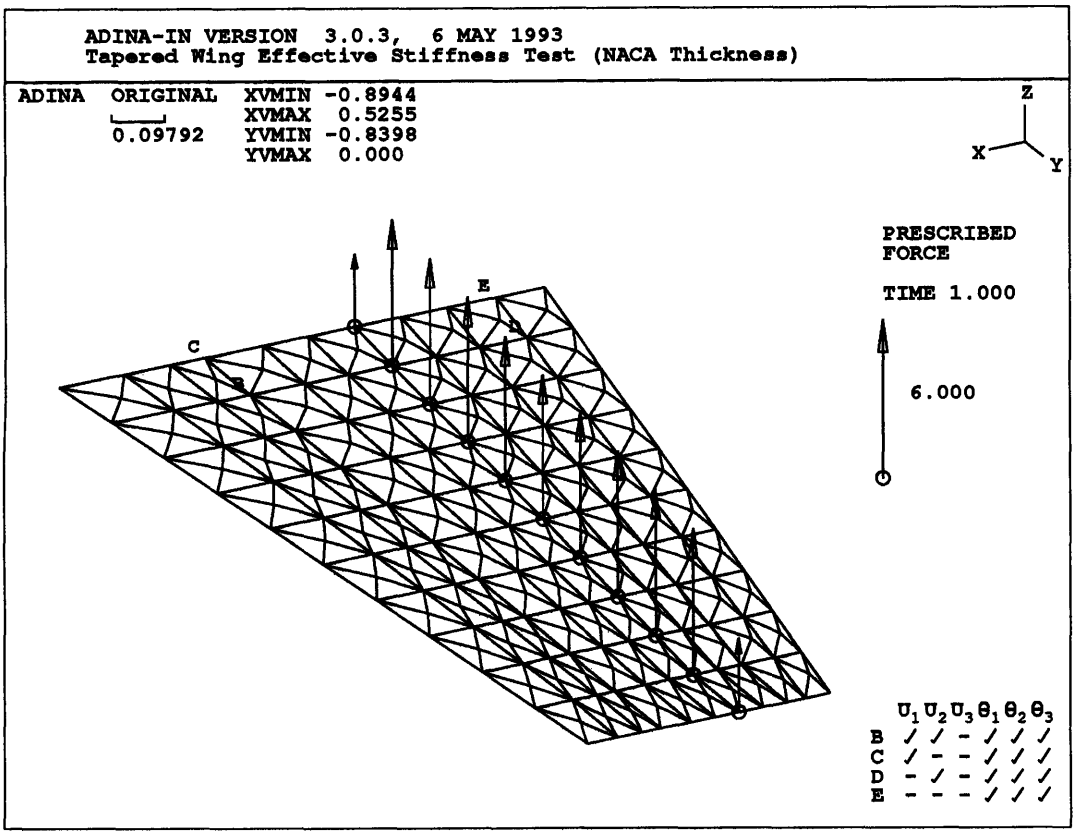

Figure A-11: NACA Tapered Wing: Effective Stiffness Test Load

The wing is loaded as shown in Figure A-9. This loading case is the same consistent nodal loading for $P = 32$ (*load/unit span*) as given in the ideal effective stiffness test described in the previous section. The material properties of this wing are given as $E = 5.0 \times 10^4$, $\nu = 0.3$. The thickness of the plate varies in the spanwise direction such that the local maximum thickness is 15% of the local chord. The thickness in the chordwise direction between the 10% and 70% chord locations follows Equation 4.18.

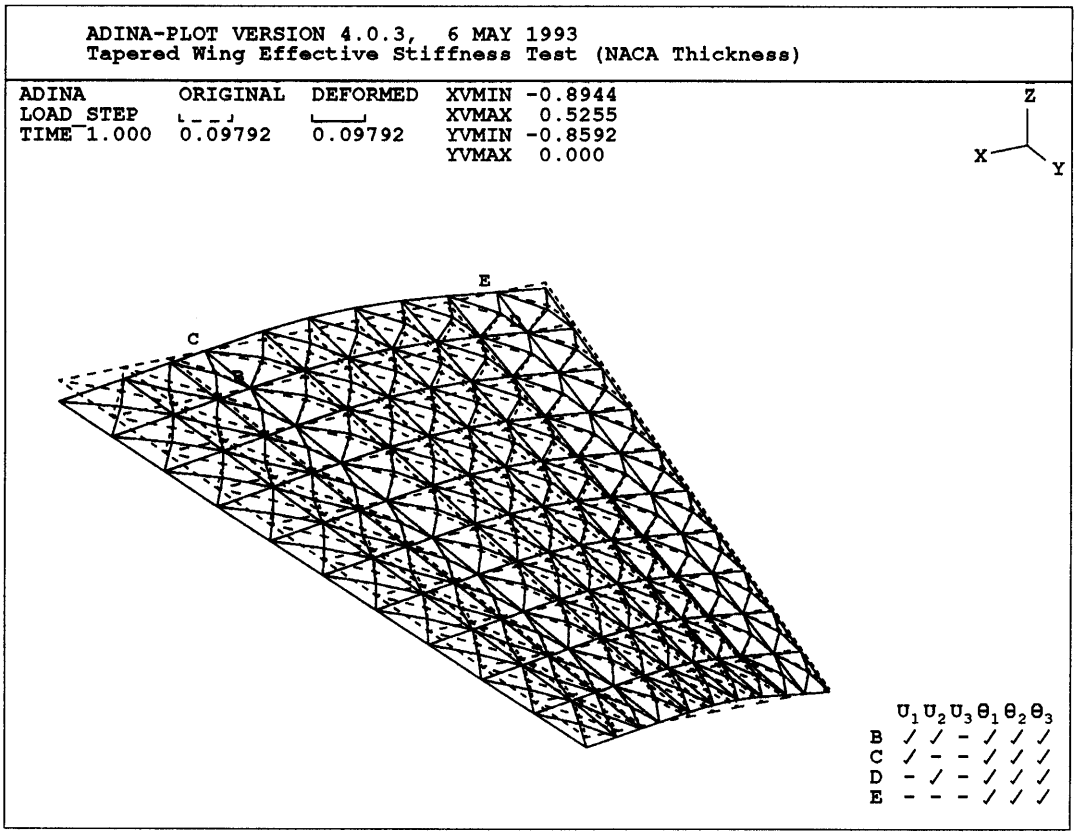

Figure A-12: NACA Tapered Wing: Effective Stiffness Test Deflection

The deflection for the effective stiffness case is shown in Figure A-10. The deflection, w, measured at the midspan is 0.019 giving the wing effective stiffness $S_{eff} = 1686$.

The critical stiffness measured numerically is $K_{crit} = 0.187$. Accounting for the aspect ratio correction, the airfoil stiffness parameter for this wing is $K_{crit\ airfoil} = 0.253$. The critical dynamic pressure, $q_{crit} = 336.54$ giving $A = 0.1996$

A.3 Flexible Sailboard Fins

Effective stiffness tests were also performed on the sailboard fins. Rather than the simple geometry of the tapered wings, these planforms have a chord distribution that more closely matches an elliptic shape. The chord distribution has been designed to cause the loading to more closely match an elliptic distribution. The spars are again placed at the 10% and 70% chord locations at the root and the spars are straight. However, since the trailing edge is not straight, the local spar axes of rotation do not lie at the 10% and 70% chord locations. Thus, even though the plate stiffness is proportional to the cube of the local chord the, change in boundary condition placement over the span causes the stiffness parameter to vary over the span. The effective stiffness test allows the complex stiffness distribution of the wing to be expressed in terms of a single number.

A.3.1 8 inch Flex Foil Fin Planform

The first flexible fin case is the 8 inch flex Foil planform. The Aspect ratio for this fin is 6.0. The span is 8 inches and the root chord is 3.5 inches.

The fin is loaded as shown in Figure A-13. This is a consistent nodal loading for $P = 10$ $(pounds/inch)$. The material properties of this wing are given as $E = 5.0 \times 10^3$ psi, $\nu = 0.3$. The thickness of the plate varies in the spanwise direction such that the local maximum thickness is 15% of the local chord. The thickness in the chordwise direction between the spar locations follows Equation 4.18.

The deflection for the effective stiffness case is shown in Figure A-14. The deflection, w, measured at the midspan is 0.041 inches giving the wing effective stiffness $S_{eff} = 243psi$.

The critical stiffness measured numerically is $K_{crit} = 0.180$. Accounting for the aspect ratio correction, the airfoil stiffness parameter for this wing is $K_{crit\,airfoil} = 0.230$. Then, $q_{crit} = 47.14psi$ gives $A = 0.194$

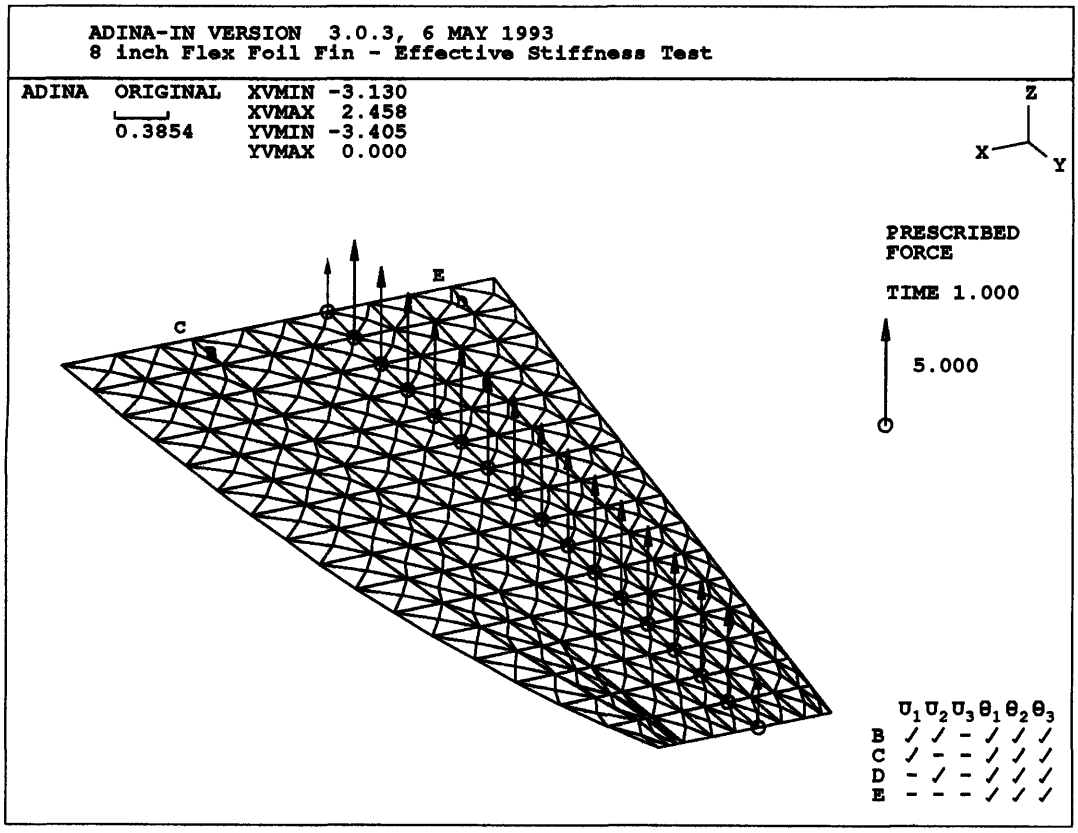

Figure A-13: 8 inch Flex Foil Fin: Effective Stiffness Test Load

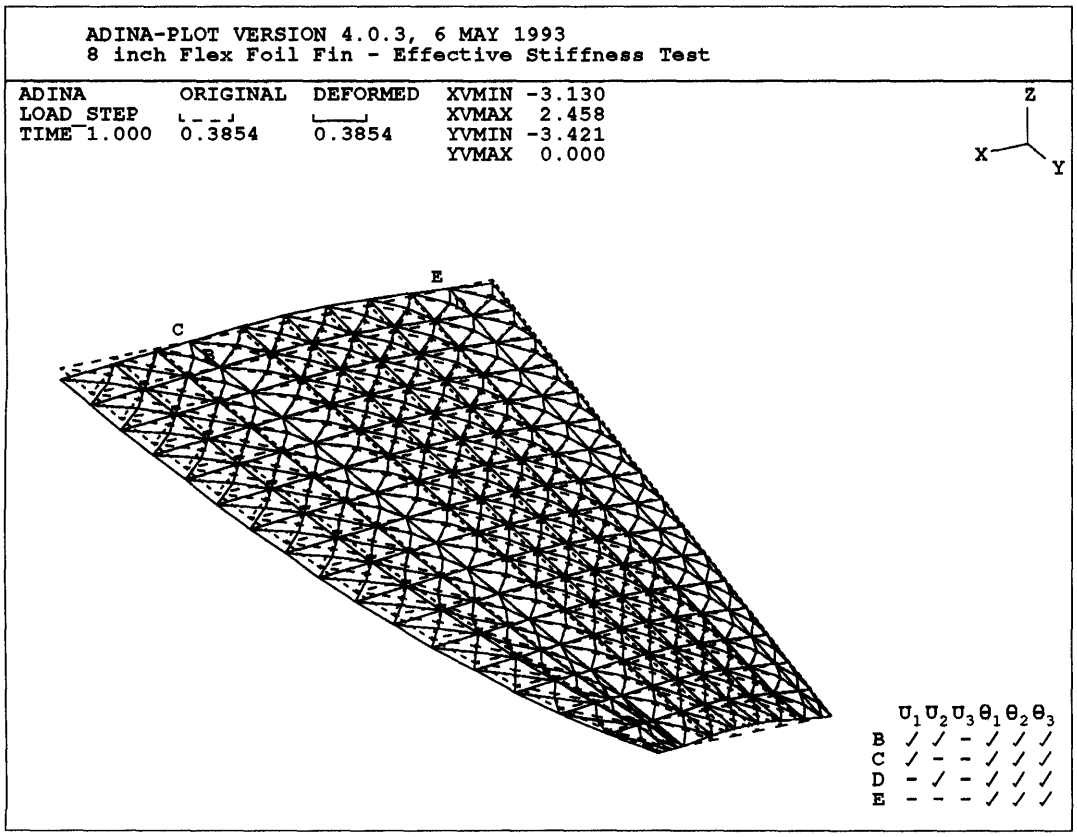

Figure A-14: 8 inch Flex Foil Fin: Effective Stiffness Test Deflection

A.3.2 10 inch Flex Foil Fin Planform

The 10 inch planform has an aspect ratio of 7.36. The span is 10 inches and the root chord is 3.7 inches.

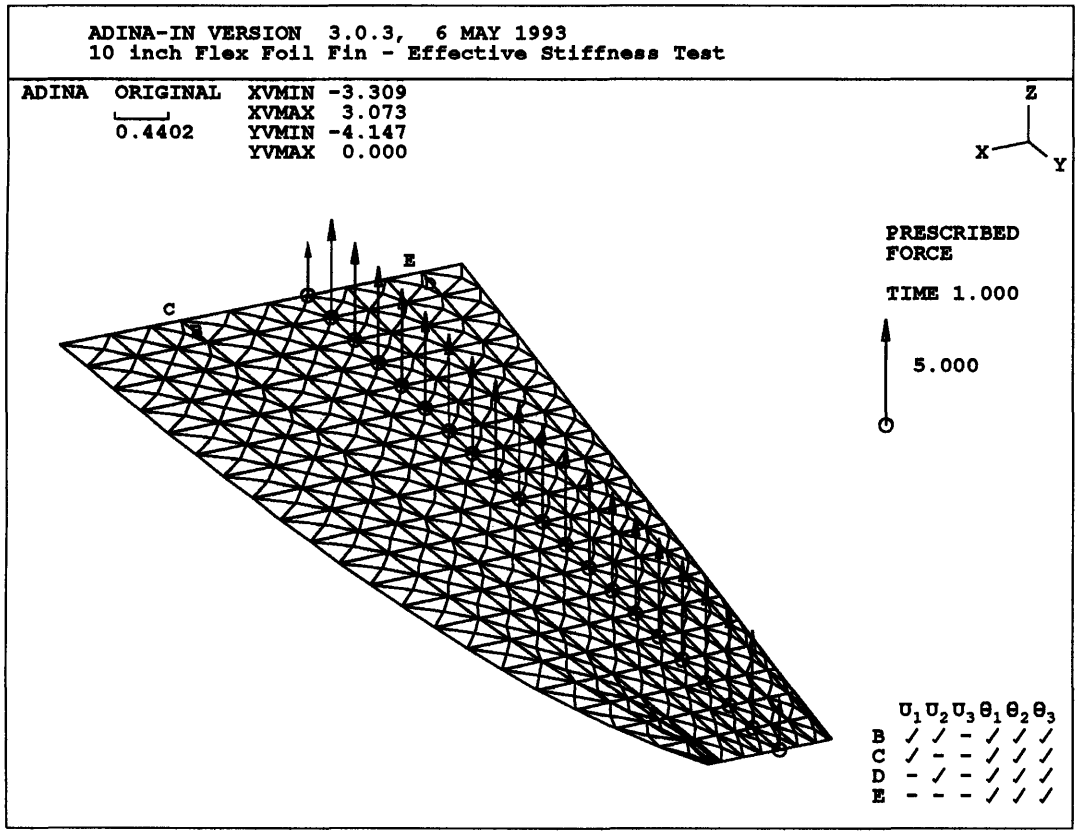

Figure A-15: 10 inch Flex Foil Fin: Effective Stiffness Test Load

The fin is loaded as shown in Figure A-15. This is a consistent nodal loading for $P = 10$ $(pounds/inch)$. The material properties of this wing are given as $E = 5.0 \times 10^3$ psi, $\nu = 0.3$. The thickness of the plate varies in the spanwise direction such that the local maximum thickness is 15% of the local chord. The thickness in the chordwise direction between the spar locations follows Equation 4.18.

The deflection for the effective stiffness case is shown in Figure A-16. The deflection, w, measured at the midspan is 0.05 inches giving the wing effective stiffness $S_{eff} = 200psi$.

The critical stiffness measured numerically is $K_{crit} = 0.171$. Accounting for the aspect ratio correction, the airfoil stiffness parameter for this wing is $K_{crit\ airfoil} =$

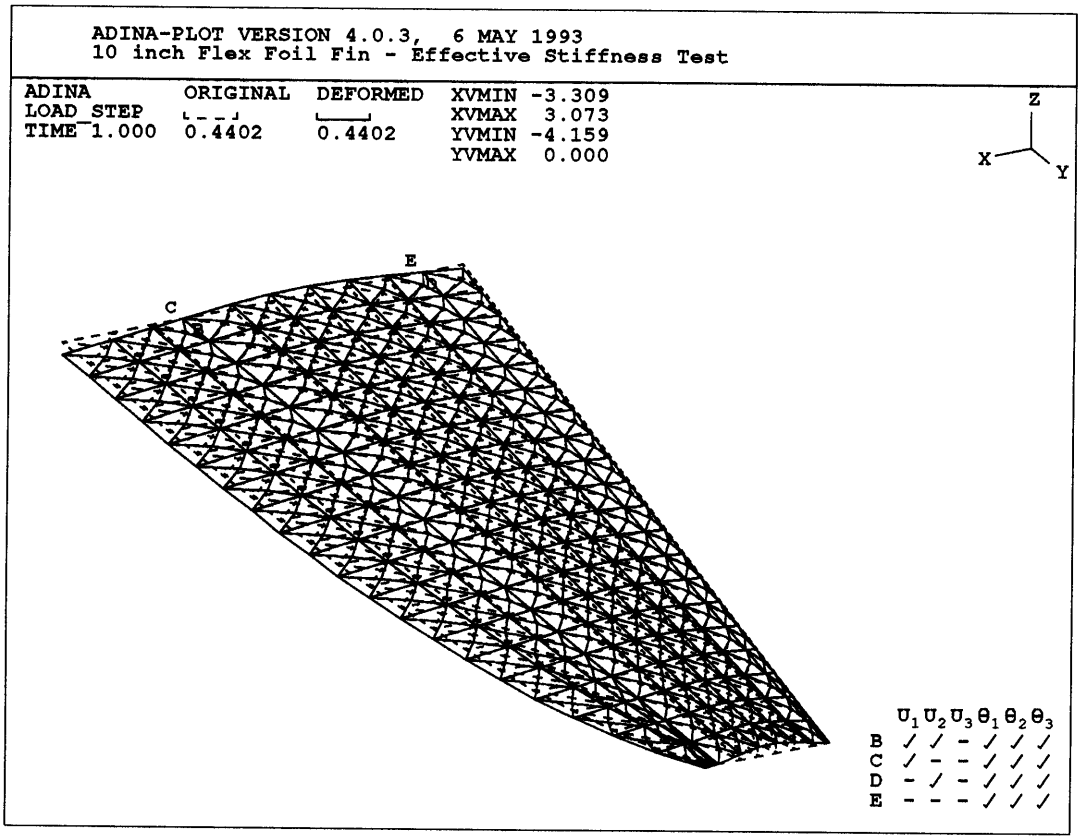

Figure A-16: 10 inch Flex Foil Fin: Effective Stiffness Test Deflection

0.388 giving $q_{crit} = 40.6psi$ and $A = 0.203$

Appendix B

Numerical Analysis

This appendix shows some of the output plots from the numerical analysis. They are presented to show some examples of the numerical solutions and the steady state behavior of the flexible wings. Examples are shown for a typical planform for each of the wing types analyzed in Chapter 4.

Numerical results are shown for several of the interesting operating points of the flexible wings. The load distribution output plots from the vortex lattice code are included for the rigid wing loading and critical stiffness loading for each of the example wings. Output plots from the finite element program showing the wing deflection at the critical stiffness are also included. These plots are typical of the output from the computer programs.

B.1 Tapered Wing: Ideal Boundary Conditions

The loading of a rigid tapered wing with aspect ratio of 5 is shown in Figure B-1.

Figure B-2 shows the loading at the critical stiffness for the wing. Since the angle of attack is nearly zero, all the load is produced by the camber of the wing as is plainly shown in this figure.

Figure B-2 shows the deflection of the wing at the critical stiffness.

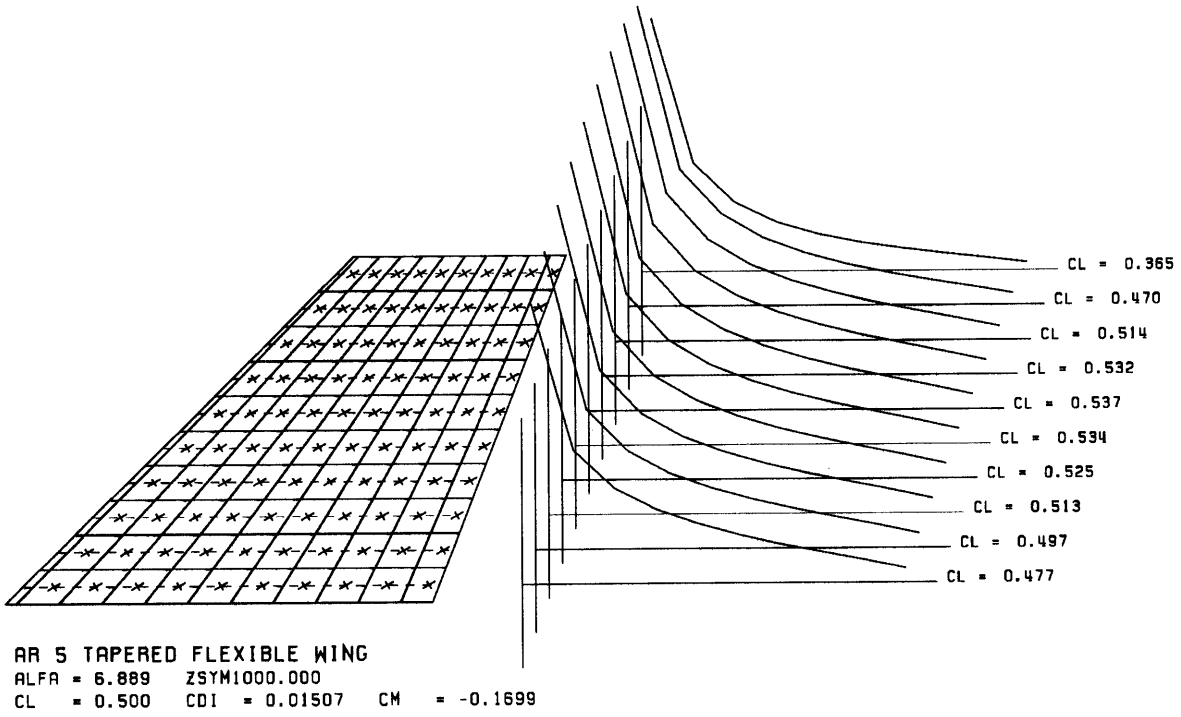

Figure B-1: AR 5 Tapered Flexible Wing: Rigid Loading

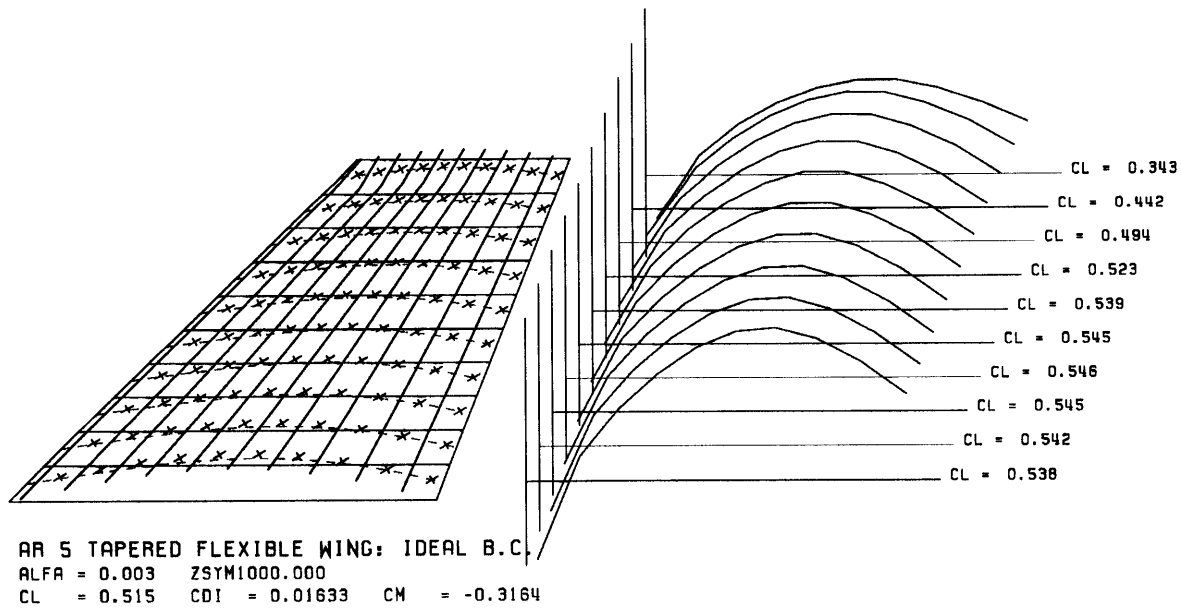

Figure B-2: Ideal AR 5 Flexible Wing: Load at Kcrit

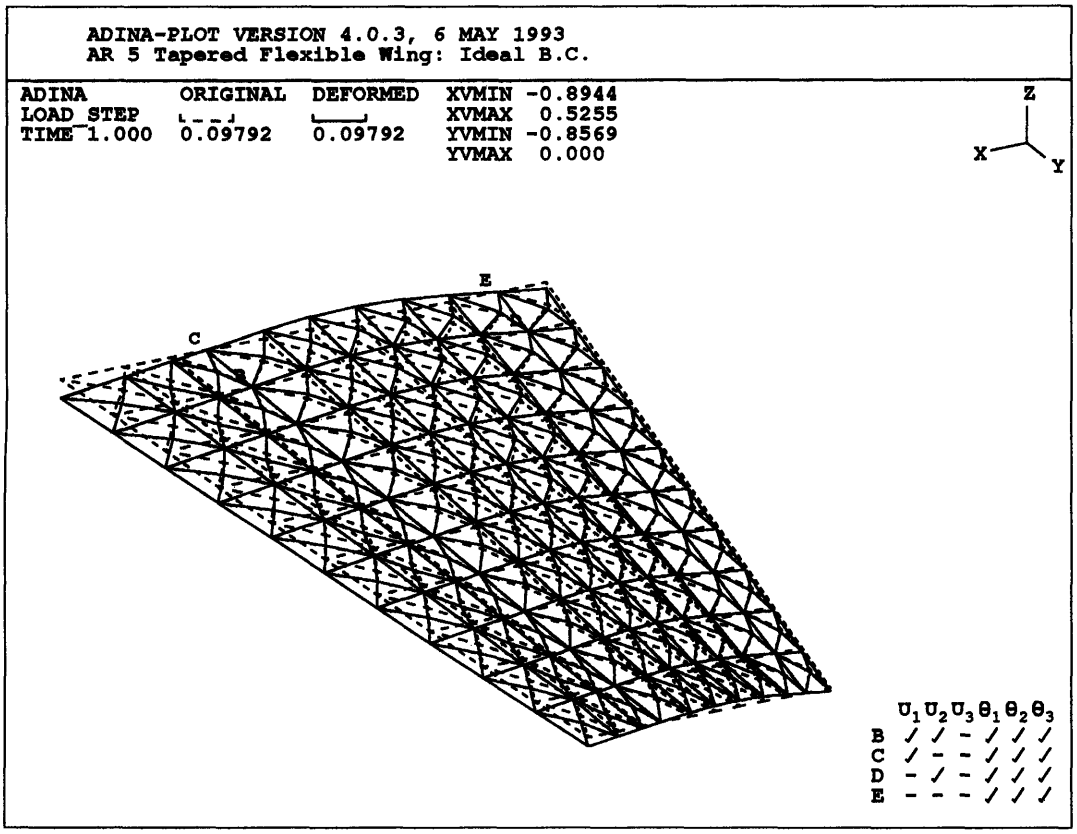

Figure B-3: Ideal AR 5 Flexible Wing: Camber at Kcrit
labelapp:ideal5-w

B.2 Aspect Ratio 5 Tapered Wing: Spar Boundary Conditions

The rigid loading for this wing planform is shown in Figure B-1. The boundary conditions and thickness distributions have no affect on the loading of the rigid wing. Thus, this rigid planform is identical to the tapered wing with ideal boundary conditions for the rigid case.

B.2.1 Aspect Ratio 5 Tapered Wing: Uniform Thickness

Figure B-4 shows the loading at the critical stiffness for the wing. Since the angle of attack is nearly zero, all the load is produced by the camber of the wing as is plainly shown in this figure.

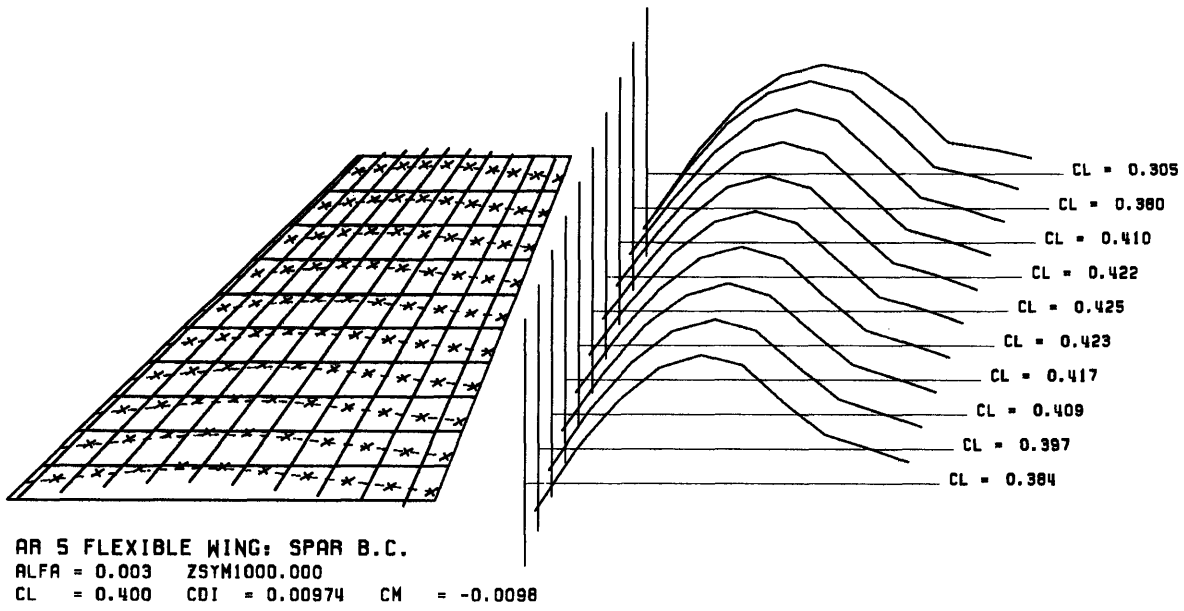

Figure B-4: Uniform thickness AR 5 Flexible Wing: Load at Kcrit

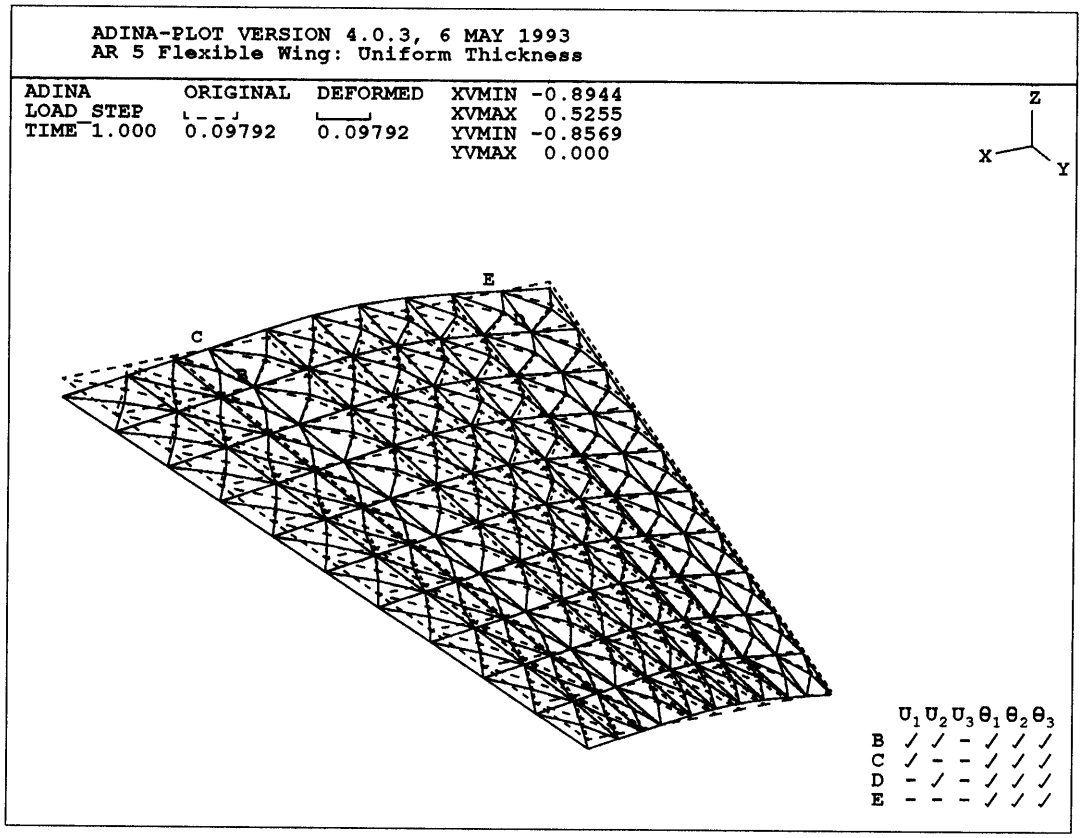

Figure B-5: Uniform Thickness AR 5 Flexible Wing: Camber at Kcrit

B.2.2 Aspect Ratio 5 Wing: NACA Thickness

For the NACA stiffness distribution, the loading is slightly different near K_{crit}. than the uniform stiffness.

Figure B-7 shows the deflection for this wing.

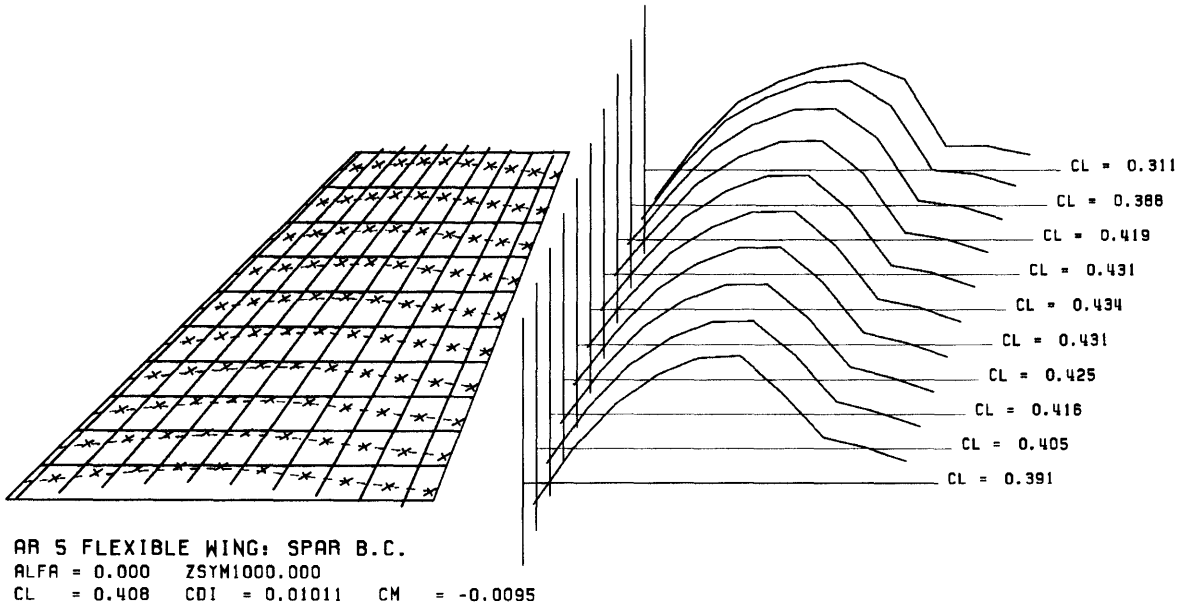

Figure B-6: NACA AR 5 Flexible Wing: Load at Kcrit

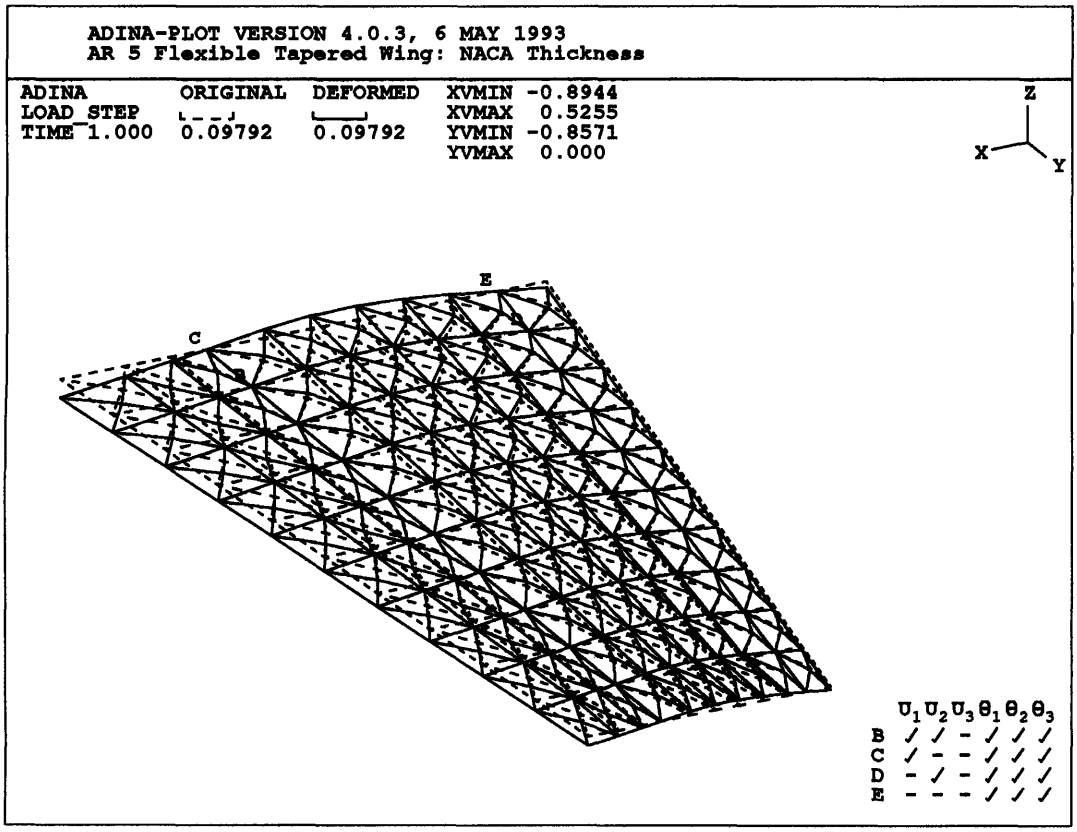

Figure B-7: NACA AR 5 Flexible Wing: Camber at Kcrit

B.3 Flexible Sailboard Fins

Results are shown for both Flex Foil planforms as the deflection behavior of these planforms is quite unique. Giver the non-uniformity in the stiffness parameter in the spanwise direction, the camber response takes on a unique shape that should be shown.

B.3.1 8 inch Fin Planform

Plots for the 8 inch planform are included to show the rigid wing loading as well as the loading at the critical stiffness. The camber response near the tip of the wing is higher than in the tapered wing examples due to the large percentage of the chord of the flexible region near the tip. This causes the tip to camber more than it normally would, and distorts the elliptic loading.

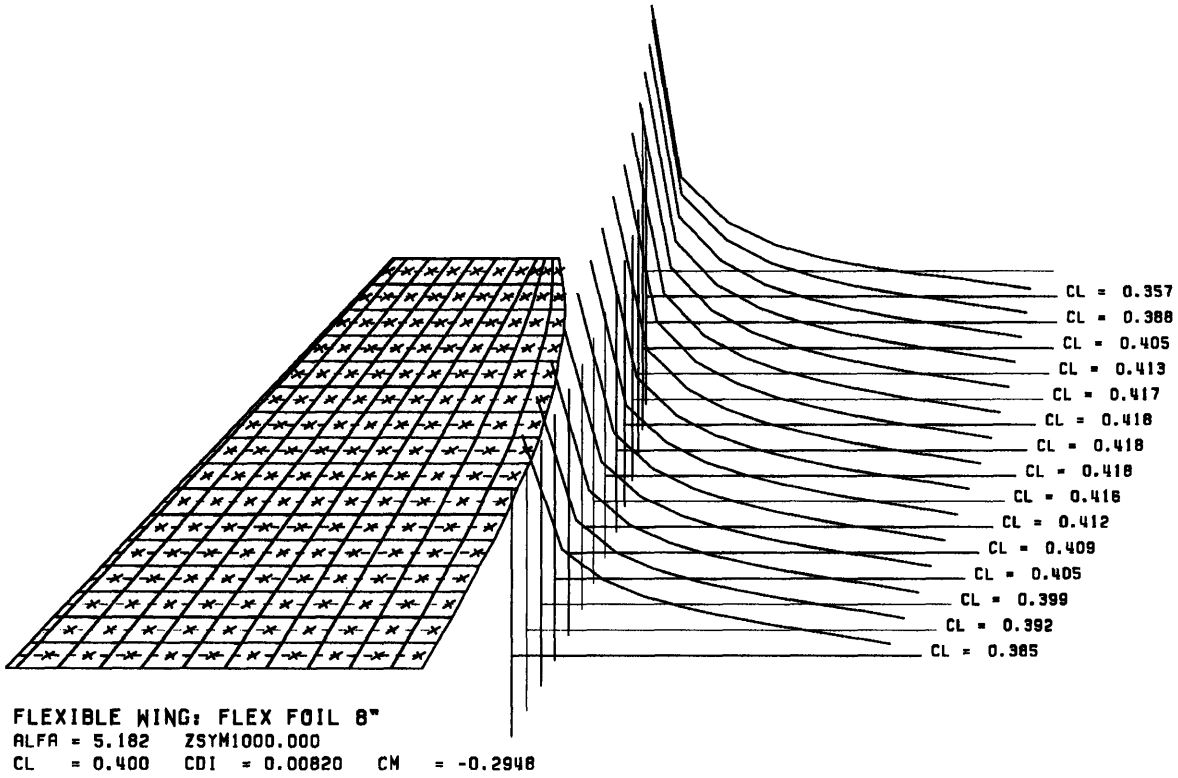

Figure B-8: 8 inch Flex Foil Planform: Initial Load

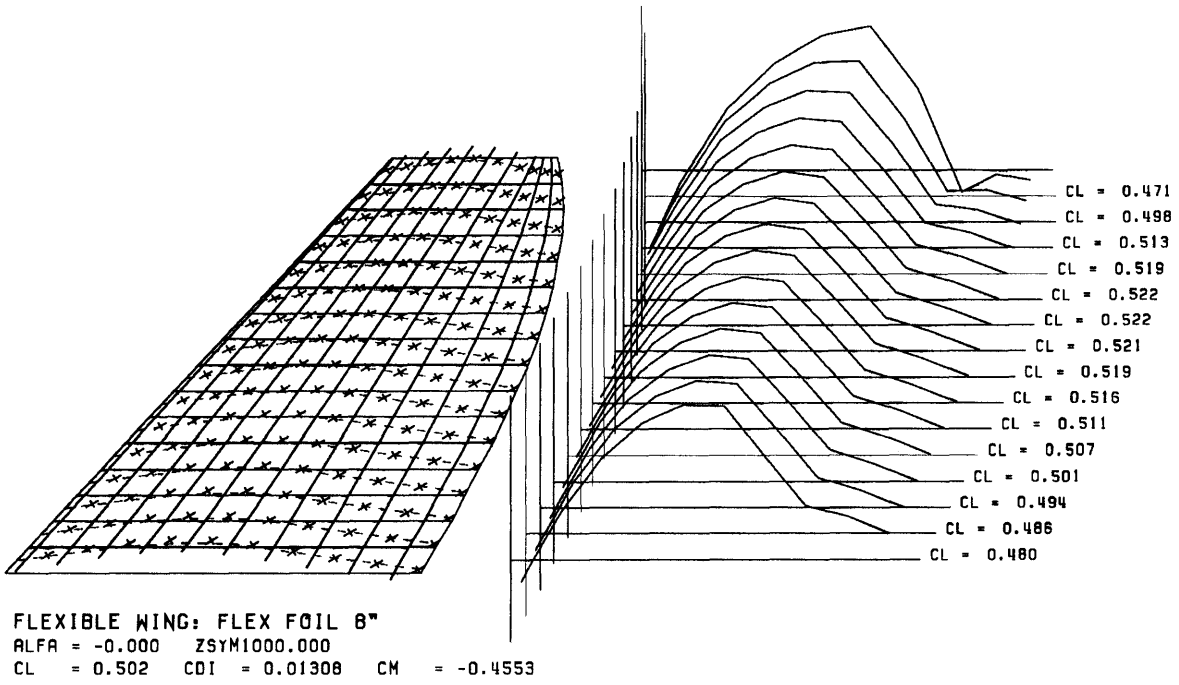

Figure B-9: 8 inch Flex Foil Planform: Load at Kcrit

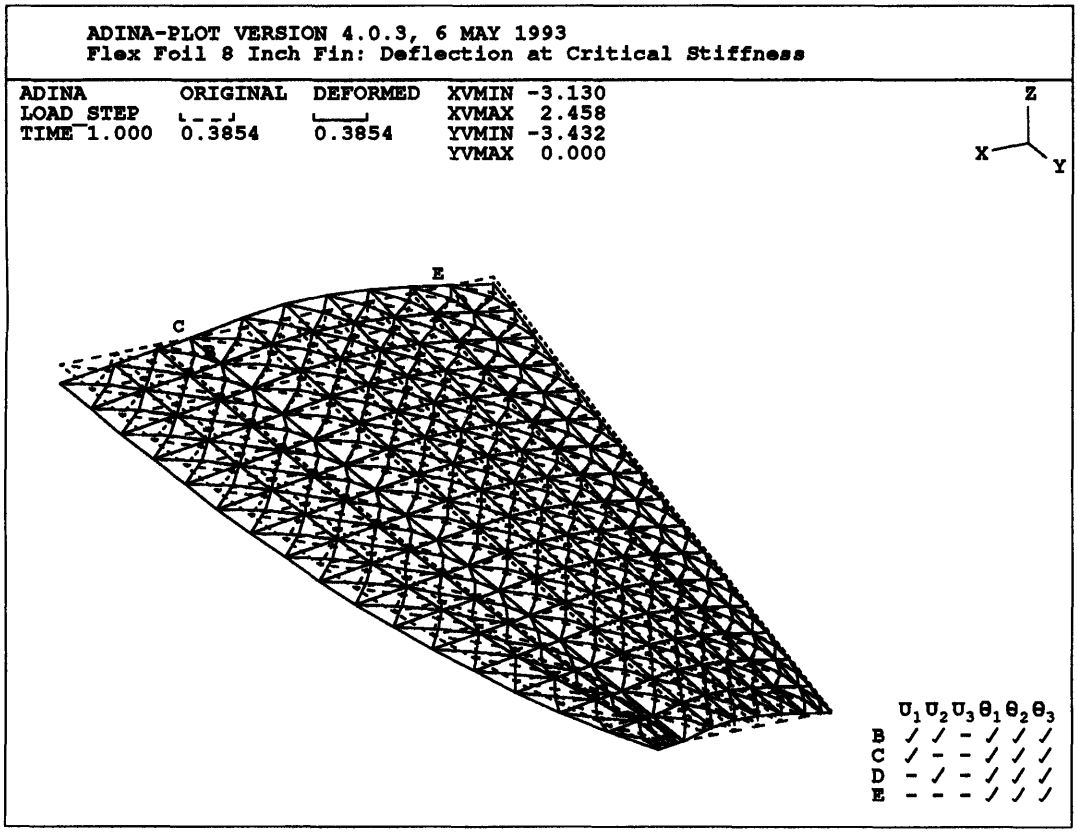

Figure B-10: 8 inch Flex Foil Planform: Camber at Kcrit

B.3.2 10 Inch Fin Planforms

The 10 inch fin shows many of the same tip effects as the 8 inch fin due to the large size of the flexible region as compared to the tip chord.

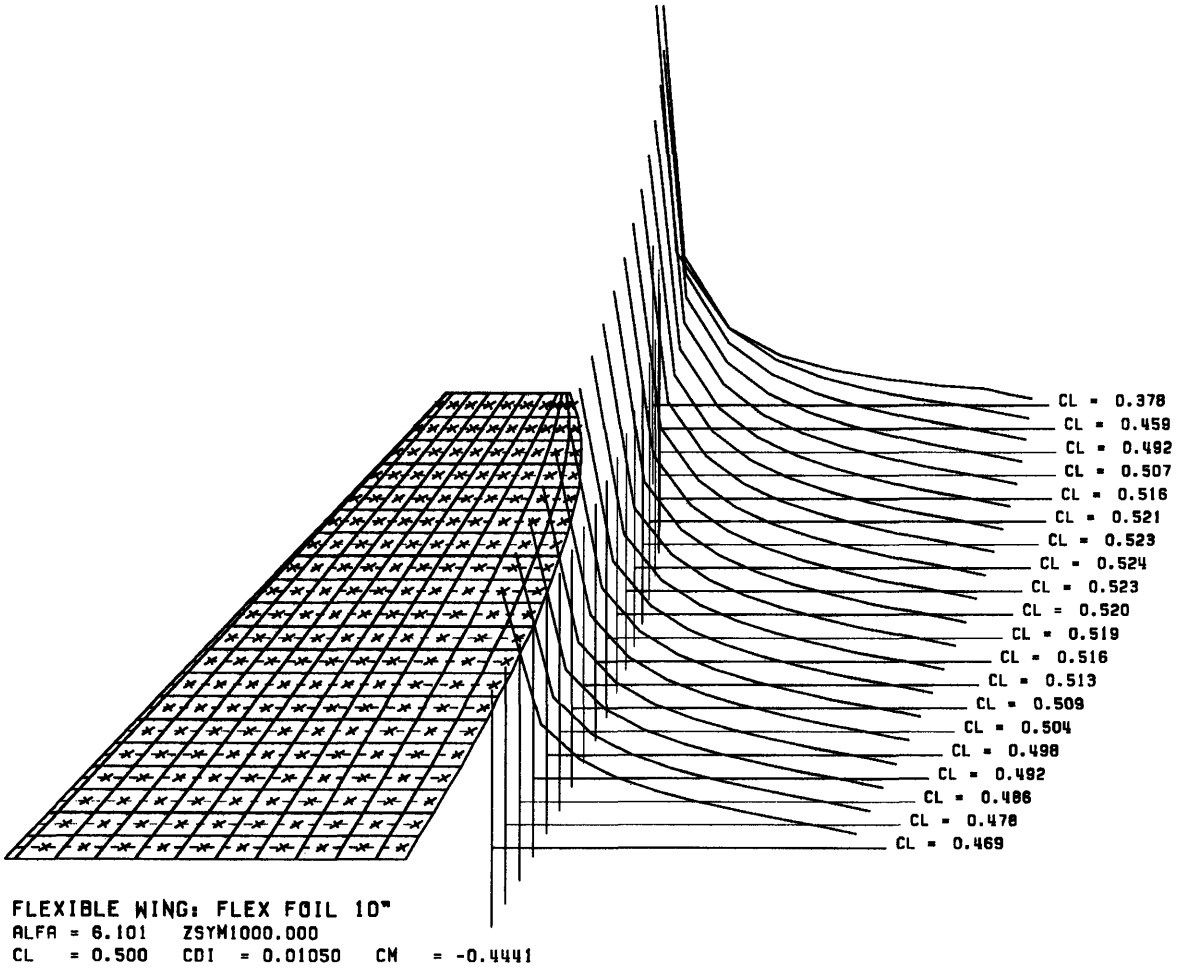

Figure B-11: 10 inch Flex Foil Planform: Initial Load

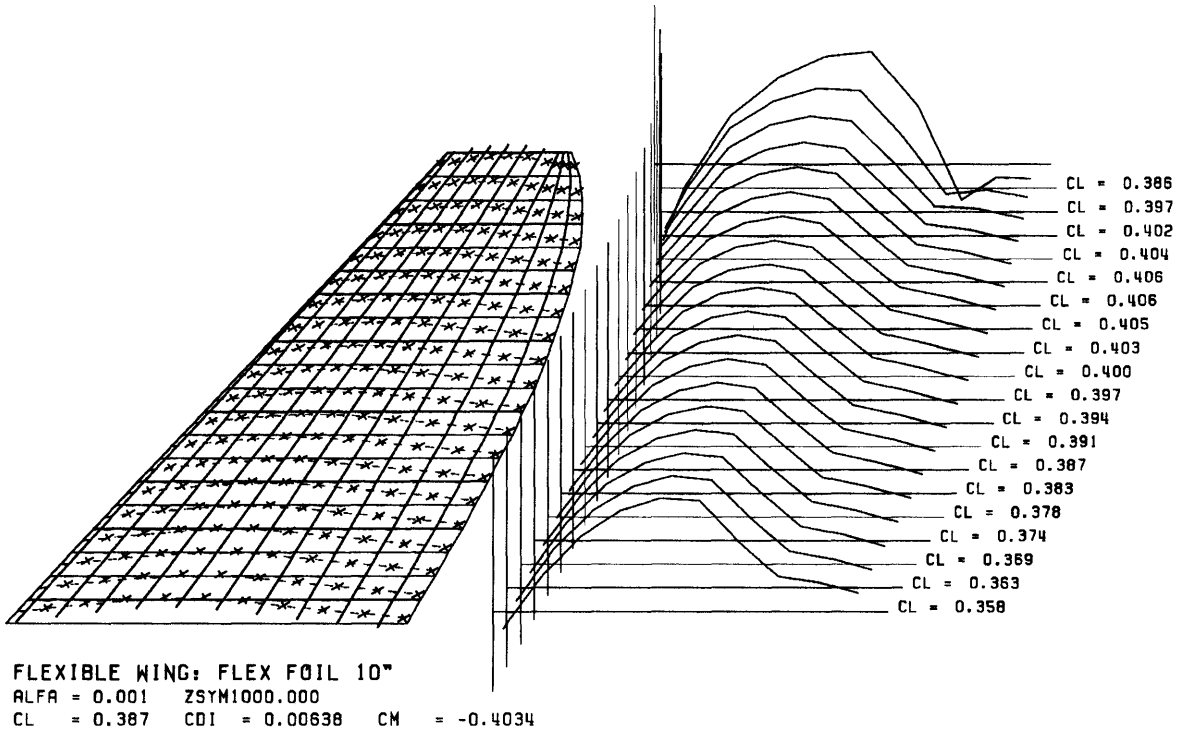

Figure B-12: 10 inch Flex Foil Planform: Load at Kcrit

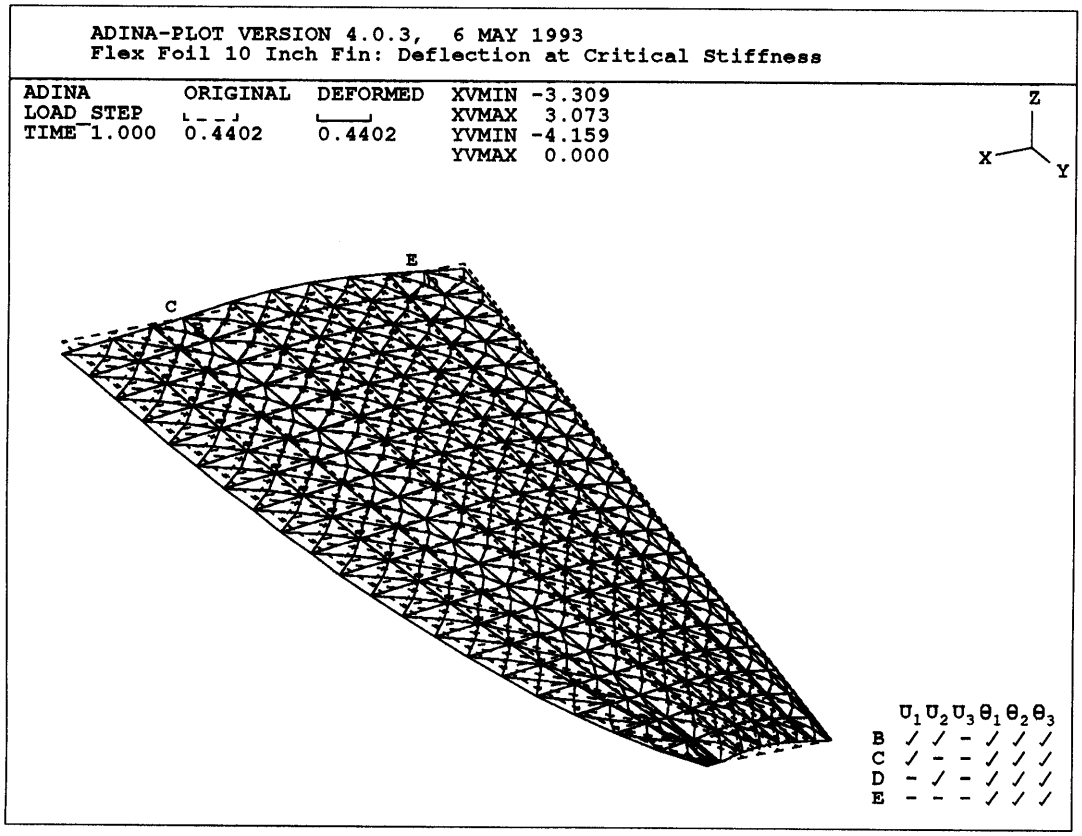

Figure B-13: 10 inch Flex Foil Planform: Camber at Kcrit

Bibliography

[1] Ira H. Abbott and Albert E. Von Doenhoff. *Theory of Wing Section.* Dover Press, 1959.

[2] Robert D. Cook, David S. Malkus, and Michael E. Plesha. *Concepts and Applications of Finite Element Analysis.* Wiley, third edition, 1989.

[3] M. Drela. Xfoil: An analysis and design system for low reynolds number airfoils. In T.J. Mueller, editor, *Low Reynolds Number Aerodynamics.* Springer-Verlag, Jun 1989. Lecture Notes in Engineering, No. 54.

[4] H. Glauert. *Elements of Airfoil and Airscrew Theory.* Cambridge University Press, second edition, 1947.

[5] Robert V. Hogg and Johannes Ledolter. *Applied Statistics for Engineers and Physical Scientists.* Macmillan, second edition, 1992.

[6] E. H. Mansfield. *The Bending and Stretching of Plates.* Macmillian, 1964.

[7] Richard Von Mises. *Theory of Flight.* Dover, 1959.

[8] Jack Moran. *Theoretical and Computational Aerodynamics.* Wiley, 1984.

[9] Stephen P. Timoshenko. *Theory of Elastic Stability.* McGraw Hill, second edition, 1961.

[10] Sheila E. Widnall, William S. Widnall, William E. Gorgen, and Jeffery T. Evernham. Flexible tailored elastic airfoil section. United States Patent Number 5,181,678, January 26 1993.